SOLID STATE THERMAL GRADIENT PROCESSING

OF $Y_1Ba_2Cu_3O_{7-x}$/Ag SUPERCONDUCTING COMPOSITE RIBBONS

by

Monica L. Kaforey

B.S., Metallurgical Engineering & Materials Science
Carnegie-Mellon University, 1989

Submitted to the Department of Materials Science & Engineering
in partial fulfillment of the requirements for the Degree of

DOCTOR OF PHILOSOPHY
in Ceramics

at the

Massachusetts Institute of Technology
Cambridge, Massachusetts

February, 1994

Signature of Author_____
Department of Materials Science & Engineering
January 7, 1994

Certified by_____
John B. Vander Sande
Associate Dean, School of Engineering
Thesis Advisor, Department of Materials Science & Engineering

Accepted by_____
Carl V. Thompson II
Professor of Electronic Materials
Chair, Departmental Committee on Graduate Students

SOLID STATE THERMAL GRADIENT PROCESSING

OF $Y_1Ba_2Cu_3O_{7-X}$/Ag SUPERCONDUCTING COMPOSITE RIBBONS

by

MONICA L. KAFOREY

Submitted to the Department of Materials Science & Engineering
on January 7, 1994 in partial fulfillment of the requirements for the
Degree of Doctor of Philosophy in Ceramics

ABSTRACT

The process of texturing materials by the use of a thermally activated phase transition in the presence of a temperature gradient was systematically examined for the first time. It was expected that an improved understanding of thermal gradient processing would lead to the eventual production of superconducting composite ribbons with improved properties due to alignment and elongation of the superconductor grains. The effect of solid state thermal gradient processing on microstructure was examined experimentally and theoretically. The starting material $Y_1Ba_2Cu_3Ag_{15}$ was used to produce $Y_1Ba_2Cu_3O_{7-x}$/Ag superconducting composite ribbons. The novel process of oxidizing metallic precursors to form superconducting composite ribbons was also investigated systematically. The importance of a low temperature oxidation stage and a high temperature transformation stage on the final microstructure was determined. The effect of various treatments within each processing stage was investigated; this included the use of solid state thermal gradient processing during the high temperature transformation stage.

During the low temperature oxidation stage, internal oxidation resulted in the formation of elemental oxides Y_2O_3, BaO, and CuO in Ag. The low temperature oxidation treatment had a very strong influence on the microstructure of the final ribbon, with the tendency for forming Ag bands being stronger in samples subjected to longer oxidation stage treatments. Ag nodules formed at the surfaces due to stress relief and an Ag band formed at the center of samples due to outward solute diffusion in samples that were completely oxidized. Complete oxidation was achieved by heating the samples in flowing oxygen 5°C/min to 140°C, 0.5°C/min to 420°C, and holding for 13 hours.

The high temperature transformation stage enabled the elemental oxides to transform to the superconducting oxide $Y_1Ba_2Cu_3O_{7-x}$. During the high temperature transformation treatment, the Ag nodules on the surface spread out

to become a surface band of Ag. Coarsening resulted in an increase in the average oxide particle size and a thickening of the Ag bands as the hold time increased, with temperatures in the range of 890°C to 900°C.

The superconducting properties of the composite $Y_1Ba_2Cu_3O_{7-X}$/Ag ribbons were tested after oxygenation. The samples were found to contain superconducting $Y_1Ba_2Cu_3O_{7-X}$ with a critical transition temperature in the range of 86 K to 90 K. The samples were found to be unable to support a supercurrent at either 77 K or 4.2 K. This was attributed to the lack of a continuous supercurrent path due to the presence of cracks, voids, Ag grains, and other non-superconducting phases such as barium cuprates.

The use of solid state thermal gradient processing to produce textured $Y_1Ba_2Cu_3O_{7-X}$/Ag composite superconducting ribbons during the high temperature transformation stage was investigated experimentally and theoretically. Experimentally, no significant amount of either preferential alignment or elongation of superconductor grains along the length of the ribbon was seen. Using a theoretical approach, nucleation should occur at orientations that are randomly distributed. Since there is no driving force for rotation, a superconductor grain will maintain the orientation of its nucleus and no preferential alignment will result. Anisotropic growth in an isothermal situation will favor the formation of plate-like grains that extend in the basal plane. In the presence of a temperature gradient, surface energy considerations show that growth will usually occur in the c-axis direction; the c-axis may or may not be perpendicular to the traveling direction. Plate-like grains are expected to form and have a wide variety of orientations and an average size that increases according to coarsening predictions. This agrees very well with the results seen experimentally. Thus, solid state thermal gradient processing alone is not likely to result in improved electrical properties due to either elongation or alignment of the superconductor grains in the superconducting composites. It is thought that the combination of mechanical deformation and solid state thermal gradient processing will result in superconducting composite ribbons with improved superconducting properties. The understanding of solid state thermal gradient processing that was gained can be applied to the production of texturing in many other materials systems including non-superconducting materials as well as other superconducting composites.

Thesis Supervisor: John B. Vander Sande
Title: Associate Dean, School of Engineering
Thesis Advisor, Department of Materials Science & Engineering

Table of Contents

List of Figures

List of Tables

Acknowledgements

I would like to thank my thesis advisor, Prof. John Vander Sande, for his guidance and assistance throughout this work. I thank the members of my thesis committee, Prof. Donald Sadoway and Prof. Yet-Ming Chiang, for their advice, particularly with respect to the writing of this document. I would also like to thank many of the MIT staff members for the help which made this endeavor possible. This list includes, but is not limited to, Mike Jercinovic, Fred Wilson, Pat Kearney, Jean DiMauro, Marj Joss, and Pat Gavagan.

Most of all, I would like to thank my husband, Paul Kaforey, for his unending support, encouragement, and computer expertise, as well as many hours of listening to me ramble, delivering late-night meals, proof-reading, and so much more. I would like to thank the many fellow graduate students who made my stay at MIT a pleasant experience, including Cindy Bedell, Jimmy Chen, Beth Stadler, Ann Redsten, Sharon Furcone, Catherine Heremans, and Hongbao Liu.

This work was made possible through the support of an NSF graduate fellowship and D.O.E. contract DE-FG02-85ER45179.

Chapter 1. Introduction

Since 1986 when Bednorz and Muller [1] discovered the first high temperature oxide superconductors, there has been a steady effort to develop processing methods for making materials with better electrical and mechanical properties. The eventual goal of such work is to produce bulk superconducting materials that can transfer large amounts of electrical power efficiently and economically.

The method of oxidizing a melt-spun metallic precursor ribbon to form a superconducting oxide/noble metal ribbon has been examined by Yurek et al. [2-5]. This method results in improved formability in the precursor stage, and improved ductility and ease of making electrical contact in the superconducting ribbon. Generally, there are three steps to this process: a metallic precursor ribbon is melt-spun, a low temperature oxidation stage treatment enables formation of elemental oxides, and a high temperature transformation stage enables transformation to a superconducting oxide.

If the superconducting oxide grains could be aligned within the ribbon in a favorable orientation, the ribbon would be expected to have a higher critical current density. Solid state thermal gradient processing was proposed as one possible method of producing oriented superconducting oxide grains. The current work was intended to examine the processing science and underlying

engineering theory. It was hoped that an improved understanding of solid state thermal gradient processing and the method of oxidizing metallic precursors to produce superconducting composite ribbons would eventually contribute to the production of superconducting composite ribbons with improved critical current densities.

Solid state thermal gradient processing as a method of producing a textured material will have potential applications in many materials systems. Thus, an improved understanding of the process and the factors which control it may have an impact well beyond the field of superconductors. More established methods of processing in a thermal gradient include directional solidification, float-zone melt growth, and melt texturing. These methods will be examined further in Section 1.3. Relevant information concerning directional solidification will be presented in Section 1.3.3.

For the current work, a metallic precursor composition of $Y_1Ba_2Cu_3Ag_{15}$ was chosen. The precursor oxidation method was examined to determine the effect of changes in the low temperature oxidation stage treatment on the final superconducting oxide/noble metal ribbon. Changes were made in the processing atmosphere and the degree of oxidation. The high temperature transition stage was examined to determine the effects of temperature, hold time, and prior treatment on the final composite microstructure. The effect of solid state thermal gradient processing during the high temperature transformation

treatment was examined. These examinations lead to an improved understanding of the process in which oxidation of metallic precursors is followed by transformation to a superconducting oxide. An improved understanding of solid state thermal gradient processing and its limitations and potential benefits for processing bulk superconductors also resulted. An improved understanding of the applicability of solid state thermal gradient processing for producing textured materials in other materials systems also resulted.

In order to examine the effect of the oxidation treatment and the effect of a temperature gradient during the transformation treatment on the resulting superconducting oxide/noble metal ribbons, it is necessary to have an understanding of two distinct areas of knowledge. First, it is necessary to have a basic understanding of the materials under consideration. An overview of the history of superconductivity followed by more specific information on the YBCO (Y-Ba-Cu-O and Yb-Ba-Cu-O) superconductors will be presented in Section 1.1. Second, It is necessary to understand the available information concerning the processing conditions. The relevant information in the areas of oxidation, thermal gradient processing, and orientation dependent growth will be presented in Sections 1.2 and 1.3. Section 1.3.5 briefly presents some concerns that apply to the processing Y-Ba-Cu-Ag precursors in a temperature gradient to form superconducting oxides in Ag.

Section 1.1 Superconductivity

1.1.1 History of High Critical Temperature Superconductors

Superconductivity was first discovered in 1911 by Onnes when mercury was cooled in liquid helium [6]. From then until 1986, the superconductive properties of a large number of metals and alloys were tested. However, no material was found to have a critical transition temperature above about 23 K (Nb alloys). Bednorz and Muller at IBM's Zurich lab chose to concentrate on oxides rather than the usual metals and alloys [7]. In 1986, they tried a material composed of barium, lanthanum, copper, and oxygen and found a critical transition temperature (T_c) greater than 30 K [1].

From the time that the results of Bednorz and Muller were published, there was a scramble to find new higher critical temperatures by testing various oxide compounds. Changes in composition resulted in finding a critical temperature above 40 K for $La_{1.85}Sr_{0.5}CuO_4$. The next breakthrough was the discovery by Wu et al. [8] of a critical temperature above 90 K in the Y-Ba-Cu-O system. This was important because it raised the critical temperature above the temperature of liquid nitrogen (77 K). The material was later identified as $Y_1Ba_2Cu_3O_{7-x}$. The critical temperature continued to increase with the discoveries of critical temperatures of 110 K for $Bi_2Sr_2Ca_2Cu_3O_{10}$ (the use of Bismuth was first reported by Chu [9]) and 125 K for $Tl_2Ba_2Ca_2Cu_3O_{10}$ (the use of thallium was first reported by Prof. Hermann of the U. of Arkansas [10]).

The consistent theme pervading the high temperature superconductors is the presence of Cu-O layers. These Cu-O layers are believed to be responsible for the superconducting properties of the materials [11].

1.1.2 $Y_1Ba_2Cu_3O_{7-x}$ Structure and Properties

The structure of $Y_1Ba_2Cu_3O_{7-x}$ is similar to that of the perovskite structure. Figure 1-1 contains a schematic of (a) the AMO_3 perovskite structure and (b) the $Y_1Ba_2Cu_3O_{7-x}$ structure [11]. In the perovskite structure, the A cation occupies the body center site, the M cations occupy the corner sites, and the oxygen is located at the center of the cube edges. In the $Y_1Ba_2Cu_3O_{7-x}$ (1-2-3) structure, there are three slightly distorted perovskite-like cubes stacked. The Cu occupies the corner sites (M), the Ba occupies the body center position (A) of the top and bottom cubes, while Y (or another rare earth element) occupies the body center position (A) of the center cube, and the oxygen is located at the center of the edges as before. The 1-2-3 compounds are oxygen deficient. There is no oxygen in the rare earth layer, and less than one-half of the oxygen sites in the basal plane are occupied. The structure described is the tetragonal structure which has a critical temperature of 66 K. The structure progresses from tetragonal to orthorhombic as the oxygen content increases (x decreases). When x = 0.095, the critical temperature reaches a theoretical maximum of 94.5 K. Note that the Cu-O layers, which are believed to be responsible for the superconducting properties of the materials, extend in the basal plane.

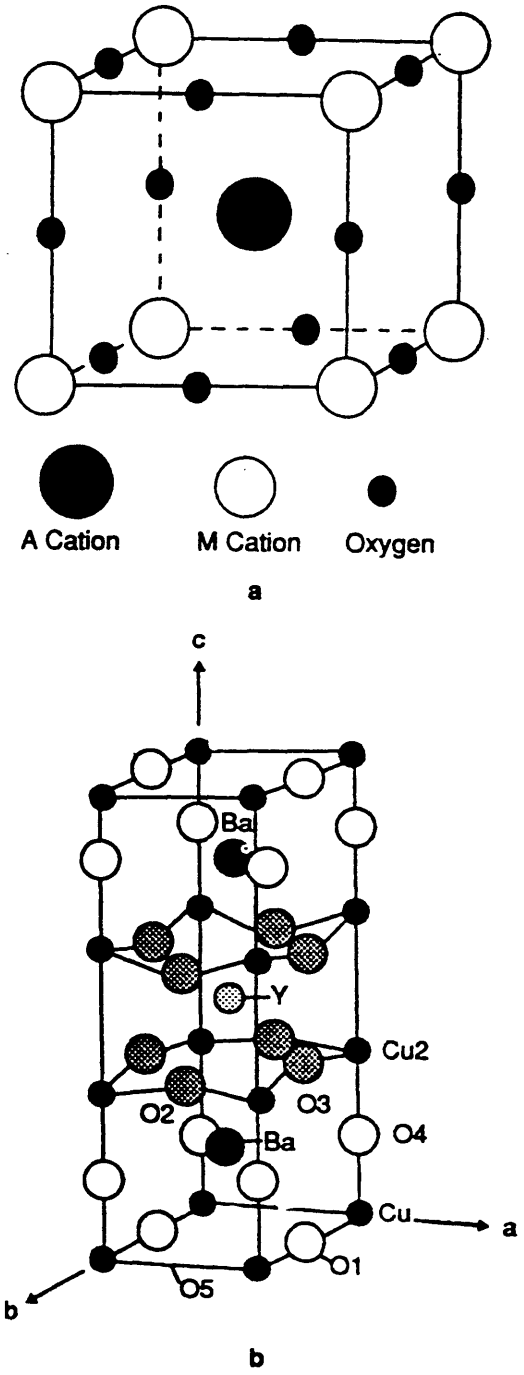

Figure 1-1. (a) The ideal perovskite structure. (b) The $Y_1Ba_2Cu_3O_{7-x}$ structure [11].

The desirable parameters for bulk superconductors to become feasible in many applications, as stated by Narayan [11], include: a critical current density (J_c) on the order of 10^6 A/cm^2, a consistent and reliable T_c of 90 K to 290 K, grain sizes of approximately 1 micron (for thin films), and a normal-state resistivity below 100 $\mu\Omega$ cm. The bulk values of J_c for polycrystalline oxide superconductors have typically been several orders of magnitude below the desired value. However, studies of thin films of $Y_1Ba_2Cu_3O_{7-x}$ on $SrTiO_3$ single crystal substrates [12] indicated that the critical currents are not intrinsically low. The grain boundaries and the anisotropy of the materials were identified as probable causes of the poor current densities in the bulk materials [13].

1.1.3 Benefits of Preferential Alignment

Many studies [14-16] have indicated that grain boundaries are the weak link which limits J_c and the critical magnetic field, H_{c2}. Clem [17] developed a model in which grains are connected by Josephson junctions. This became known as the "weak link" model. Further interest in investigating grain boundaries has lead to studies such as Dimos et al. [18] in which the orientation dependence of grain boundary critical current in $Y_1Ba_2Cu_3O_{7-x}$ bicrystals was examined. The ratio of critical current density in the grain boundary relative to the critical current density in the grains was found to decrease significantly with increasing misorientation angles. Their results showed that achieving a high degree of

texture both normal to and within the basal plane is important for obtaining very high critical current densities in pure polycrystalline samples.

Studies of single crystal YBCO superconductors showed considerable anisotropy in resistivity, critical current density, and upper and lower critical fields [19-22]. In orthorhombic $Y_1Ba_2Cu_3O_{7-x}$, the critical current density in the basal plane is about one order of magnitude greater than in the c-axis direction [23]. Thus, it would be advantageous to have a crystallographic texture in which the basal planes of the grains are parallel to the conduction direction. If conduction is to occur along the length of a ribbon, this means that the c-axis of the grains should be perpendicular to the length of the ribbon.

Aligning the c-axis of the grains perpendicular to the length of the ribbon is also beneficial for reducing microcracking. Sintered superconducting oxide materials have a tendency for microcracking due to the stresses resulting from anisotropic contraction during transformation and anisotropic contraction during cooling from processing temperatures [24]. In both of these cases, the contraction is most severe in the c-axis direction. In a material in which the c-axis directions are aligned orthogonal to the conduction direction, the tendency for grain boundary cracking is significantly reduced. The denser, uncracked material will have better mechanical and electrical properties.

Thus, improvements in the understanding of solid state thermal gradient processing are likely to contribute to the production of favorably textured

superconducting grains in the superconducting oxide/noble metal composites. These textured composites are expected to have improved electrical properties due to the intrinsic anisotropy of the grains and the reduced misorientation angles between grains. Aligning the c-axis of the oxide grains perpendicular to the length of the ribbon is also expected to improve the mechanical properties of the ribbons.

1.1.4 Metallic Precursor Route

The method of oxidation of metallic precursors, developed by Yurek et al. [2], was found to be a useful method for producing dense superconducting oxides. This method is advantageous because the resulting superconducting oxides tend to be more dense than those produced by more traditional ceramic processing methods such as sintering or hot isostatic pressing (hipping). Oxidation of metallic precursors is also promising because of the formability of the precursors. Unlike oxides which are brittle, a metallic precursor may be readily formed into useful shapes such as cables and wires. Melt spinning is one way, but not the only way, of producing the metallic precursor ribbons.

1.1.5 Benefits of Having a Noble Metal Present

Yurek et al. [3-5] found that a noble metal could be added to the liquid prior to melt spinning. Oxidation of the quaternary (e.g. Eu-Ba-Cu-Au) precursor results in a microcomposite of the superconducting oxide and the noble metal. The ease of joining a superconducting oxide to electrical terminators with a

low-resistance contact is greatly improved in the oxide/metal composites. The ductility of the resulting ribbon was found to have a greater ductility than either the ceramic oxide alone or an extruded wire in a metal sheath. The microcomposite material was also expected to have improved fracture toughness, maximum strain-to-failure and cryostability [25].

In the Y-Ba-Cu system, it is difficult to produce a homogeneous metallic precursor because a 16 wt% Y, 49.6 wt% Ba, and 34.4 wt% Cu liquid separates into two immiscible liquid layers [4]. The addition of 33 wt% Ag or more results in a miscible liquid [26] which can be melt-spun with greater success. Thus, the precursor will have greater homogeneity in addition to the previously mentioned benefits of having a noble metal present.

1.1.6 Benefits of Alternating Layers of Ag and Superconducting Oxide

Arrangements of alternate layers of Ag and superconducting oxide within the microcomposite material have some advantages [27]. Since an interconnected oxide path does not exist perpendicular to the layers, crack propagation in this direction is inhibited. The crack must move through the pure noble metal and this is more difficult than traveling through the oxide. The interconnectivity of the oxide phase is greater in this layered arrangement than for a random composite. This is because the same volume fraction oxide phase is located in the smaller volume which excludes the noble metal layers. Sandhage [27] published a paper which examined the formation of microlaminates of $Y_1Ba_2Cu_3O_{7-x}$/Ag by an

oscillating oxidation scheme. Sandhage reported bulk J_c measurements on the order of 10^3 A/cm^2 for the cross-sectional area occupied by the $Y_1Ba_2Cu_3O_{7-x}$.

Texturing of the oxide phase at Ag/oxide interfaces was observed in Ag-clad Bi2Sr2CaCu2O8+x superconducting tapes [28]. In this material there was a strong tendency for (001) texturing of the oxide at the interface. This indicates that the formation of Ag layers might also have benefits in developing a textured superconducting oxide within a composite material.

Section 1.2 Oxidation Theory and Predictions

There are several publications that are relevant to the consideration of the oxidation of the $Y_1Ba_2Cu_3Ag_{15}$ metallic precursor ribbons. The theories of Wagner [29] on internal oxidation will be examined in Section 1.2.1. The relevant diffusivity data will be summarized and the oxidation behavior of the $Y_1Ba_2Cu_3Ag_{15}$ ribbons will be predicted in Section 1.2.2. A brief summary of some published results on the formation of noble metal nodules at the surface due to strain relief will be presented in Section 1.2.3.

1.2.1 Internal Oxidation

Before attempting to predict the oxidation behavior of the $Y_1Ba_2Cu_3Ag_{15}$ ribbons, the relative reactivity of the elements present should be known. The enthalpy of formation of one mole of oxide for each of the metals present may be seen in Table 1.1. The metals in order of most to least reactive are Y, Yb, Ba,

Cu, and Ag. Thus, it is expected that the Ag will remain unreacted and the other metals will be oxidized.

Table 1.1. Enthalpy of formation of one mole of oxide for each of the metals present.

Metal Oxide	Enthalpy of Formation (kcal/mole)	Source
Y_2O_3	-455.4	Kubachewski & Hopkins [30]
Yb_2O_3	-432	Gschneider [31]
BaO	-139.0 +/- 2	Rosenqvist [32]
CuO	-37.1 +/- 0.8	Rosenqvist [32]
Cu_2O	-40.0 +/- 0.7	Rosenqvist [32]
Ag_2O	-7.3 +/- 0.1	Rosenqvist [32]

The possibilities for oxidation mechanisms include both internal and external oxidation. External oxidation would result in the formation of an oxide scale on the surface of the ribbon. Internal oxidation would result in small oxide particles being formed throughout an unoxidized Ag phase.

Internal oxidation is the expected form of oxidation for this starting material because it satisfies the various criteria suggested in the literature. Wagner [29] states that "a low concentration of the less noble alloying constituent and a high oxygen solubility in the nobler main constituent promote the occurrence of internal oxidation without the development of an outer skin." In the case of $Y_1Ba_2Cu_3Ag_{15}$, the more noble constituent is Ag, and the less noble alloying constituents include the other 3 metals. The solubility of oxygen in Ag is

relatively high (1.3 X 10^{-5} atomic fraction at 420°C [27]), and the concentration of Y, Ba, and Cu combined is 0.268 atomic fraction.

Combe and Cabane [33] note that the oxygen flux must be greater than the solute flux in order to obtain internal oxidation. That is, considering alloy AB, with oxide formation of BO_v,

$$C_o^0 D_o \rangle\rangle C_B^0 D_B \tag{1-1}$$

where C_o^0 is the solubility of oxygen in the alloy, C_B^0 is the concentration of the solute, and D_o and D_B are the diffusivities of oxygen in A and B in A, respectively. In this case the main constituent, A, is the metal Ag, and Y, Ba, and Cu are solute elements. The diffusivity of O in Ag is 1.16 X 10^{-6} cm^2/s at 420°C [34]. Diffusivities of the solute elements in Ag are on the order of 10^{-13} cm^2/s or less at 420°C [35]. Thus the flux of oxygen is several orders of magnitude greater than the combined flux of the solute elements. If any one of the solute elements is considered individually, the difference is even greater.

Combe and Cabane [33] summarize the equations for predicting the thickness of the internally oxidized zone, ξ (cm) as

$$\xi = 2\gamma(D_o t)^{\frac{1}{2}} \tag{1-2}$$

with

$$\gamma = \left[\frac{C_o^0}{2\nu C_B^O}\right]^{\frac{1}{2}} \tag{1-3}$$

where t is time (s).

1.2.2 Diffusion and Solubility Data

Various approximations for the solubility of oxygen in Ag are available. An approximation is given in Podgurski & Davis [36] of

$$\log S = -0.840 - \frac{2250}{T} + \frac{1}{2}\log P \qquad (1\text{-}4)$$

where S is the solubility of oxygen in Ag (cm^3/g of O_2 at STP), T is temperature (K), and P is partial pressure of oxygen (Torr). Another approximation is given in Eichenauer & Muller [37] of

$$\log S = -0.597 - \frac{2593}{T} + \frac{1}{2}\log P. \qquad (1\text{-}5)$$

Sandhage [27] gives an approximation of 1.3×10^{-5} atomic fraction at 420°C.

An approximation for diffusivity of O in Ag is given in Kontoulis & Steele [34] of

$$D_o = 0.00498 \exp\left(\frac{-0.50}{kT}\right) \qquad (1\text{-}6)$$

where k is Boltzmann's constant (eV/K). Gryaznov et al. [38] state the diffusivity of O in Ag as 4.67×10^{-4} cm^2/s in the range of 250°C to 400°C. Sandhage [27] uses a value of 9×10^{-7} cm^2/s at 400°C.

Using equations (1-2) and (1-3), and considering all of the solute elements ($C_B^0 = 0.286$ and $\nu \cong 1.13$), the predicted thickness of the oxidation zone was

calculated for a ramp rate of 0.5°C/min with hold times of 0 (ramp only), 4 hours, 8 hours, and 13 hours in flowing oxygen, a ramp rate of 5°C/min with hold times of 0 (ramp only) and 4 hours in flowing oxygen, and a ramp rate of 10°C/min with hold times of 0 (ramp only), 14 hours, and 17 hours in air. The results of these calculations are shown in Table 1.2. The time during the ramp was approximated as a step function with 1 hour intervals at each step.

Table 1.2. Predicted thickness of the oxidation zone using various combinations of the available solubility and diffusivity data.

Ramp Rate:		0.5°C/min (in flowing oxygen)				5°C/min (in air)		10°C/min (in air)		
Hold time:		ramp only	4 hr	8 hr	13 hr	ramp only	4 hr	ramp only	14 hr	17 hr
Solubility Source	Diffusivity Source	Thickness (microns)								
Podgurski & Davis [36]	Kontoulis & Steele [34]	1.76	3.12	4.04	4.96	0.38	1.78	0.27	3.26	3.6
Eichenauer & Muller[37]	Kontoulis & Steele [34]	1.29	2.31	3.01	3.7	0.28	1.33	0.19	2.44	2.69
Sandhage [27]	Kontoulis & Steele [34]	7.62	13.9	18.1	22.2	1.63	8.01	1.15	14.7	16.2
Podgurski & Davis [36]	Gryaznov et al.[38]	45.7	68.8	85.9	103	9.79	36.1	6.92	65.5	72.1
Eichenauer & Muller[37]	Gryaznov et al.[38]	32.6	50.4	63.4	76.6	6.98	27	4.94	49	53.9
Sandhage [27]	Gryaznov et al.[38]	189	300	379	459	40.6	16.2	28.7	29.5	32.5
Podgurski & Davis [36]	Sandhage [27]	1.75	3.1	4.02	4.93	0.38	1.77	0.27	3.25	3.58
Eichenauer & Muller[37]	Sandhage [27]	1.28	2.3	2.99	3.68	0.27	1.32	0.19	2.43	2.68
Sandhage [27]	Sandhage [27]	7.58	13.8	18	22.1	1.62	7.97	1.15	14.6	16.1

1.2.3 Strain Relief

During internal oxidation, nodules of the noble metal element have been seen to form on the surface. Mackert et al.[39] reported this behavior for a dental material based on Pd-Ag. The nodules were explained as resulting from "a type of Nabarro-Herring creep driven by the hydrostatic compressive stress introduced by the internal oxidation of tin and indium." Guruswamy et al.[40] examined the internal oxidation of Ag-In alloys. In this case, silver nodules free of oxide particles were observed to form at the surface. The volume of the silver nodules was comparable to the total volume increase caused by internal oxidation. The volume change resulted in a stress gradient between the stress-free surface and the internal oxidation front which is under a high compressive stress. Nabarro-Herring creep based on lattice diffusion of Ag was not adequate to account for the high rate of Ag transport to the surface; pipe-diffusion controlled creep was proposed as the mechanism of stress accommodation by silver diffusion.

In a recent publication, Sandhage [27] observed the formation of Ag nodules at the surface during internal oxidation of a $Y_1Ba_2Cu_3Ag_{29}$ metallic precursor. Thus, it is to be expected that surface silver nodules will form during oxidation of $Y_1Ba_2Cu_3Ag_{15}$ metallic precursor ribbons.

Section 1.3 Use of a Temperature Gradient to Affect a Material's Microstructure and Properties

Thermal gradient processing involves the movement of a thermal gradient relative to a specimen. There are many commonly known forms of thermal gradient processing such as zone refining, float-zone crystal growth, and melt texturing. In all of the processes just mentioned, the specimen is melted and then crystallized as the temperature gradient passes. It is also possible to use a temperature gradient to produce changes in a material without melting if the original material is metastable under the processing conditions. This is known as solid state thermal gradient processing (SSTGP).

Consider a long rod that is traveling at a constant velocity up a temperature gradient. The rod is initially made of metastable phase α and transforms to stable β. The transformation of α to β is thermally activated. A schematic of this model is shown in Figure 1-2.

If the rod is considered as a series of short segments, β may nucleate and grow in each segment. If the growth rate is faster than the traveling velocity, the nuclei will expand to cover the cross section of the rod and also extend down the temperature gradient until the decreasing temperature causes the growth rate to slow to match the traveling velocity. This temperature where the growth rate is equal to the traveling velocity is labeled T_g. The temperature at which nucleation of β first begins to occur is T_n.

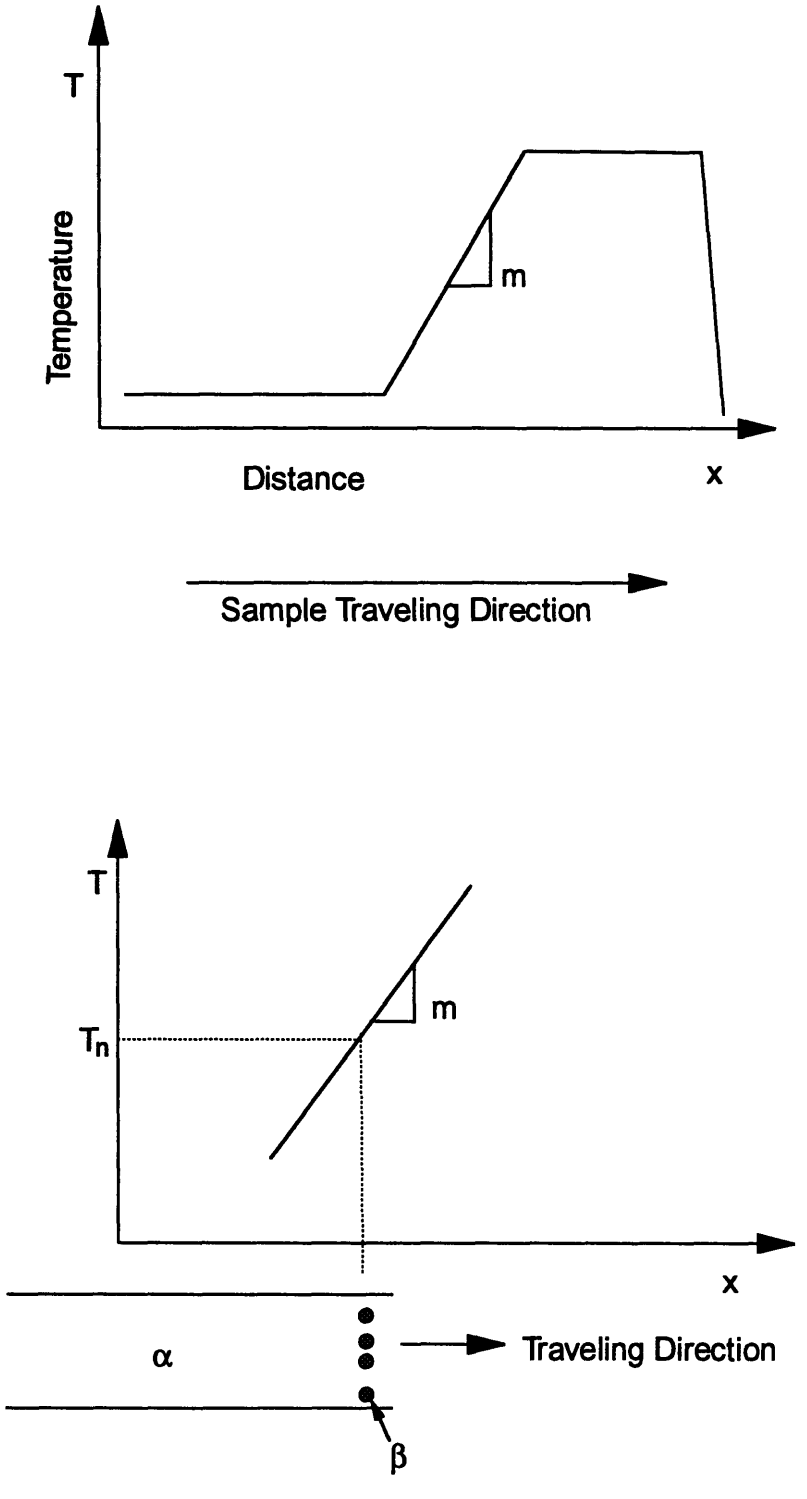

Figure 1-2. Schematic of solid state thermal gradient processing (SSTGP).

1.3.1 Steady State Thermal Gradient Processing with No New Nucleation

If $T_g < T_n$, then nucleation of new grains does not occur at steady state conditions; the result is grains of β that extend along the length of the rod from a short non-steady state region to the end of the rod. This is shown schematically in Figure 1-3. A similar case occurs during directional solidification [41], and floating melt-zone processing [42-45], where solidification is activated by a decreasing temperature.

1.3.2 Anisotropic Growth

Anisotropic growth has been shown to result in texturing without the presence of a temperature gradient [46-49]. In a one component system, this is due to the orientation dependence of the rate of grain boundary migration [50]. Anisotropic growth in the presence of a temperature gradient has been used to result in texturing during directional recrystallization, particularly in oxide dispersion strengthened materials [51-53].

In the case where $T_n > T_g$, the grains which are oriented with their fast growth directions parallel to the temperature gradient will grow faster than grains with other orientations. In the steady state condition, only grains with favorable orientations will remain. These grains will then extend to the end of the rod. Directional solidification has been used to produce aligned grains of intermetallic materials for turbine blade applications [41]. The transformation is from the liquid state to the solid state and new nucleation is prevented by using a slow

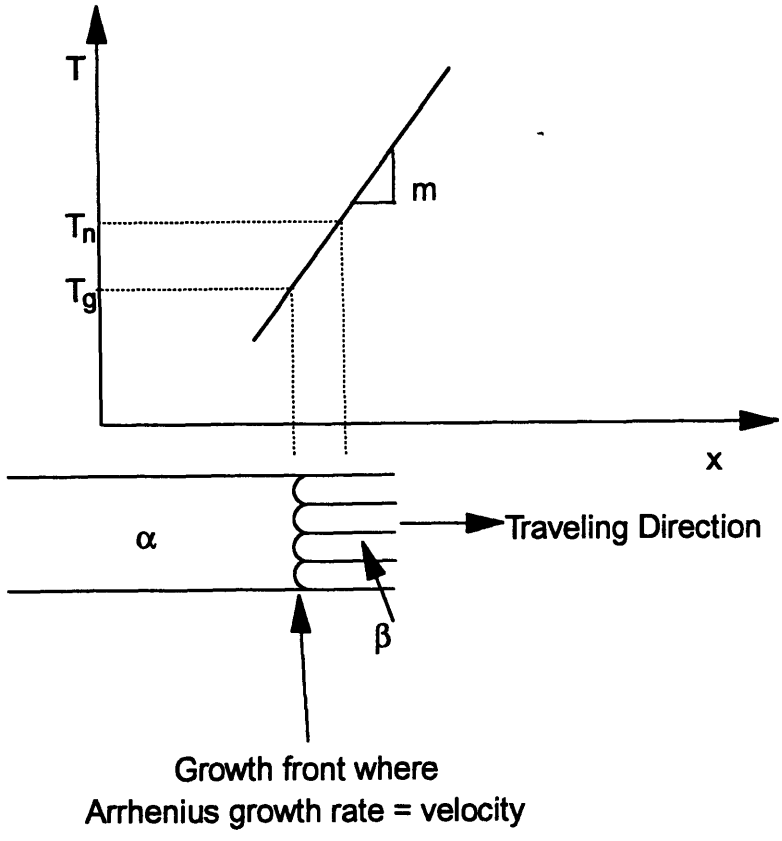

Figure 1-3. Steady state SSTGP with no new nucleation ($T_g < T_n$).

velocity. The grains that are oriented with their fast growth direction parallel to the temperature gradient grow faster than those grains with less favorable orientations and, eventually, only the grains with favorable orientations remain.

1.3.3 Directional Recrystallization

One common SSTGP method is directional recrystallization, also known as zone annealing. Directional recrystallization has been used on a wide variety of materials including pure molybdenum wires [54], gold and silver films [55], various semicrystalline polymers [56], aluminum [57], intermetallic superalloys [58], single crystals of niobium nitride [59] and vanadium nitride [60] under nitrogen atmospheres, and others. Christensen [60] produced single crystals of $VN_{0.84\text{-}1.0}$ and $TiN_{0.9}$ using multiple passes through an annealing zone at a temperature below the melting temperature. Christensen et al. [59] used zone melting followed by zone annealing to produce single crystals of niobium nitride. It was noted that the nitrogen content of the resulting material depended on the annealing temperature, ambient gas pressure, and duration of the annealing experiment.

Directional recrystallization has been widely used to produce texturing in oxide dispersion strengthened (ODS) materials. The process has been labeled by a variety of names including Zone Aligned Polycrystals (ZAP) [61-62], Moving Zone Heat Treatments [52], Zone Annealing (ZA) [53], and gradient annealing [63]. In most of these cases, a hot zone was traversed across a stationary

sample. Allen [61] noted that the process was found to depend on the recrystallization temperature. Cairns et al. [52] observed that the grain aspect ratio tends to increase with decreasing zone travel rate. Baloch & Bhadeshia [64] also observed that with rapid travel rates equiaxed grain structures resulted, while at slower travel rates, a highly elongated, directionally recrystallized microstructure was produced. Their explanation of this effect was that the recrystallization front can not keep up with the travel speed; thus, the sample is only partially recrystallized upon leaving the heat source. Although many of these articles include a qualitative discussion of the effect of various process parameters on the resulting material, a quantitative model for the process has not been published.

One other use of a temperature gradient is discussed in Shewmon [65]. It was noted that a precipitate phase could form at one end of a solid solution alloy when the alloy was placed in a stationary temperature gradient. All other methods of thermal gradient processing discussed in this work involve the movement of a thermal gradient relative to the sample.

1.3.4 Steady State Thermal Gradient Processing With Nucleation

If $T_n < T_g$, then nucleation of new β grains does occur in each segment before the segment reaches the location of the growth front at T_g. The nucleation first occurs at T_n as the rod travels up the gradient. The growth front at T_g consumes any α that did not convert to β due to the nucleation in the

gradient. The β grains that nucleate in the gradient are embedded in the α/β interface at T_g. Thus, the growth of the elongated β grains at T_g is stopped in the area where the new β grain exists. At steady state, the grains will have an average length that depends on temperature gradient, traveling velocity, and nucleation and growth rates. If the temperature gradient is steep enough and the traveling velocity is slow enough, elongated grains will result.

The modeling attempt that is closest to the current experimental conditions is that of Otto [66]. Otto considers the case of a rod of unit area traveling up a temperature gradient at a velocity, v, and transforming from α to β (see Figure 1-4). Consider consecutive segments of length D. As a segment reaches a temperature sufficient for nucleation to occur (T_n), nuclei are formed which expand to fill the cross-section of the rod. The grains grow along the length of the rod to the point at which the decreasing temperature slows the growth rate to equal the traveling velocity. The temperature at this growth front is T_g.

If $T_n > T_g$, then at steady state no new nucleation may occur and the grains extend to the end of the rod. The case treated by Otto is that of $T_n < T_g$. (The detailed calculations for Otto's approximations are presented in Appendix 1.) In the case of $T_n < T_g$, new nuclei may form, which become grains that embed in the α/β interface at T_g (see Figure 1-5). The total area fraction of new β grains formed in a segment of length D projected onto the α/β interface is F. The

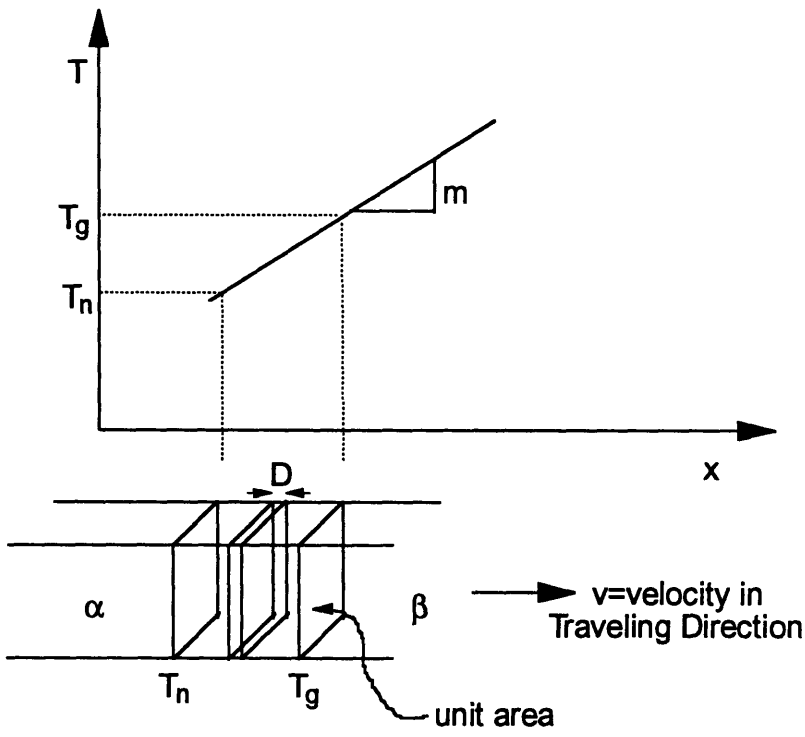

Figure 1-4. Schematic of SSTGP as treated by Otto model ($T_n < T_g$).

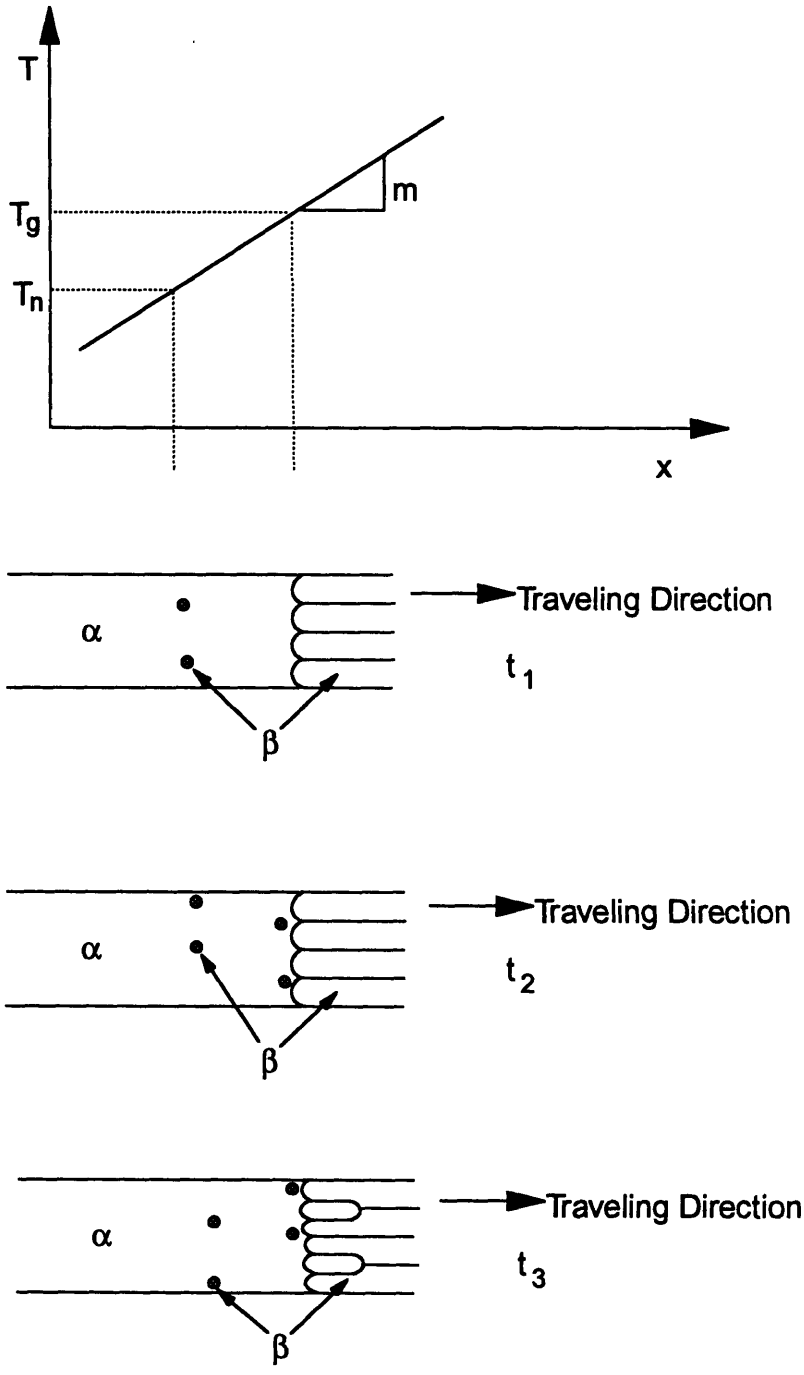

Figure 1-5. Schematic showing how new grains embed in the interface at T_g.

average number of segments per grain is N. The average radius of a grain is r_a. Thus, the aspect ratio is

$$\Phi = \frac{ND}{2r_a}. \tag{1-7}$$

In order to maintain the validity of the two-dimensional approximation of nucleation and growth, the average repeating length is $2r_a$. Thus, $D = 2r_a$ and $\Phi = N$.

N is calculated in terms of F as

$$N = \frac{0.693}{F} - 0.693 \tag{1-8}$$

for the general case and

$$N = \frac{0.693}{F} \tag{1-9}$$

for the case of very small F. F is then calculated in terms of the nucleation and growth parameters.

Otto approximates nucleation and growth rates as exponentially increasing with respect to temperature such that

$$I = 2r_a B_n \exp(\frac{-E_n}{kT}) \tag{1-10}$$

and

$$R = B_r \exp(\frac{-E_r}{kT}) \tag{1-11}$$

where k is Boltzmann's constant, B_n and B_r are constants, and E_n and E_r are

activation energies for nucleation and growth, respectively. This leads to

$$F = \frac{2\pi B_n B_r^3 E_n^{\frac{1}{2}} T_g^8 k^4 \exp\left(\frac{-(E_n+3E_r)}{kT_g}\right)}{E_r^3 m^4 v^4 (E_n+2E_r)^{\frac{3}{2}}} \qquad (1\text{-}12)$$

where m is the temperature gradient and v is the traveling velocity.

The aspect ratio appears to be proportional to $(mv)^4$. This indicates that the process should be highly influenced by the temperature gradient and the traveling velocity. However, the velocity must equal the growth rate at T_g. If the velocity increases, T_g will also increase and the T_g^8 term will overpower the v^4 term. Thus, an increase in velocity actually results in reduced elongation.

1.3.5 Additional Concerns for Processing of Metallic Precursors in a Temperature Gradient to Form Superconductors

In the case of processing metallic Y-Ba-Cu-Ag precursors in a temperature gradient to form superconducting oxides in Ag, there are a few additional complications that were not dealt with in Otto's analysis. One consideration is the presence of the noble metal. Another consideration with respect to the formation of 1-2-3 superconductors is the anisotropic growth rate. These materials grow approximately 10 times faster in the a-b plane than in the c-axis direction. The effects of the presence of the noble metal and the anisotropic growth will be discussed in Section 4.4. Also, the applicability of Otto's approximations to this more complicated system will be examined.

Chapter 2. Experimental Procedure

Section 2.1 Starting Material

The melt spun precursor ribbons of nominal composition $Y_1Ba_2Cu_3Ag_{15}$ and $Yb_1Ba_2Cu_3Ag_{16}$ were prepared using the following method, which was reported in Kogure et al [26]. Pieces of alloys were melted quickly in an argon atmosphere in a fused silica crucible to achieve the desired composition. The liquid alloy was ejected through a nozzle in the bottom of the crucible onto a spinning chromium-plated wheel. The wheel had a surface speed on the order of 27 m/s. The typical ribbons produced were less than 10 cm long, approximately 2 mm wide, and less than 50 microns thick. The ribbons that were produced in this way were cut to lengths of 2 cm to 3 cm and considered to be the starting material for the current experiments.

Section 2.2 Furnaces

Three furnaces were used in the experiments. An isothermal furnace, I, was used for annealing samples at a constant temperature in air. A controlled ramp furnace, R, was capable of ramping the temperature at a controlled rate and having an atmosphere of either air or flowing oxygen. Furnace R was used whenever a controlled atmosphere or changing temperature were desired. A temperature gradient furnace, TG, was used to enable a sample to travel through a temperature gradient. For more detail about any of these furnaces, see Sections 2.2.1 to 2.2.3.

2.2.1 Isothermal Furnace I

Isothermal furnace I was capable of maintaining a steady temperature within ±2°C of a desired hold temperature between 700°C and 1000°C. The furnace temperature was controlled by a Eurotherm controller and thyristor model 931/125A/240V/M/X//. The temperature was monitored independently using an Omega Type S thermocouple and an Omega thermometer model 199-SC-X-X. The sample chamber was a silica tube that was open to the atmosphere. Thus, the only available atmosphere was room air. The samples were loaded in a crucible lined with Ag foil. The crucible was suspended in the hottest part of the furnace. The variation in temperature over the length of the samples was less than 2°C.

This furnace was used for annealing samples in air. This was generally done after a sample received an oxidation treatment and a high temperature transformation treatment. The standard anneal was 3 hours at 890°C. The samples were loaded directly into a hot furnace, held for the desired time, and removed from the furnace to be cooled in air. Information on specific samples which received an isothermal anneal is located in Section 3.5.

2.2.2 Controlled Ramp Furnace R

Furnace R was capable of maintaining a temperature ramp at a desired rate from room temperature to 1000°C. The temperature was controlled using a Eurotherm programmable controller model 808/L1/M0/M0/N0/(ASNC200)// and Eurotherm thyristor model 831/30A240V/LVS-FC/M//. The sample chamber was a silica tube as in furnace

I. However, this tube could be sealed to provide a controlled atmosphere. The atmospheres used were room air and flowing oxygen from an AIRCO gas cylinder of standard purity oxygen. The samples were loaded as in Furnace I in an Ag foil lined crucible suspended in the hottest part of the furnace. The variation between the desired temperature and the actual temperature during a typical ramp can be seen in Figure 3-2 for an oxidation stage treatment and Figure 3-14 for a high temperature transformation treatment. The samples were loaded into a cold furnace, heated at the desired ramp rate, held for the desired tme, if any, and removed from the furnace to be cooled in air. For details about these treatments for specific samples see Sections 3.2 and 3.3, respectively.

Oxygenation treatments were also done in this furnace. The standard oxygenation treatment was an isothermal hold at 500°C for 20 hours in flowing oxygen. The samples were loaded directly into a hot furnace, held for the desired time, and removed from the furnace to be cooled in air. Two samples (Y15-38 and Y15-30) were loaded into a furance at 600°C and held for 12 hours, cooled 0.5°C/min to 450°C, and held for 24 hours. Two samples (Y15-21 and Y15-53) were given the standard oxygenation treatment and an additional oxygenation hold for 120 hours at 500°C in flowing oxygen. See Section 3.6 for more information on oxygenation.

2.2.3 Temperature Gradient Furnace TG

Furnace TG was used to enable a sample to travel through a temperature gradient. A schematic of the furnace is shown in Figure 2-1. The furnace consists of two

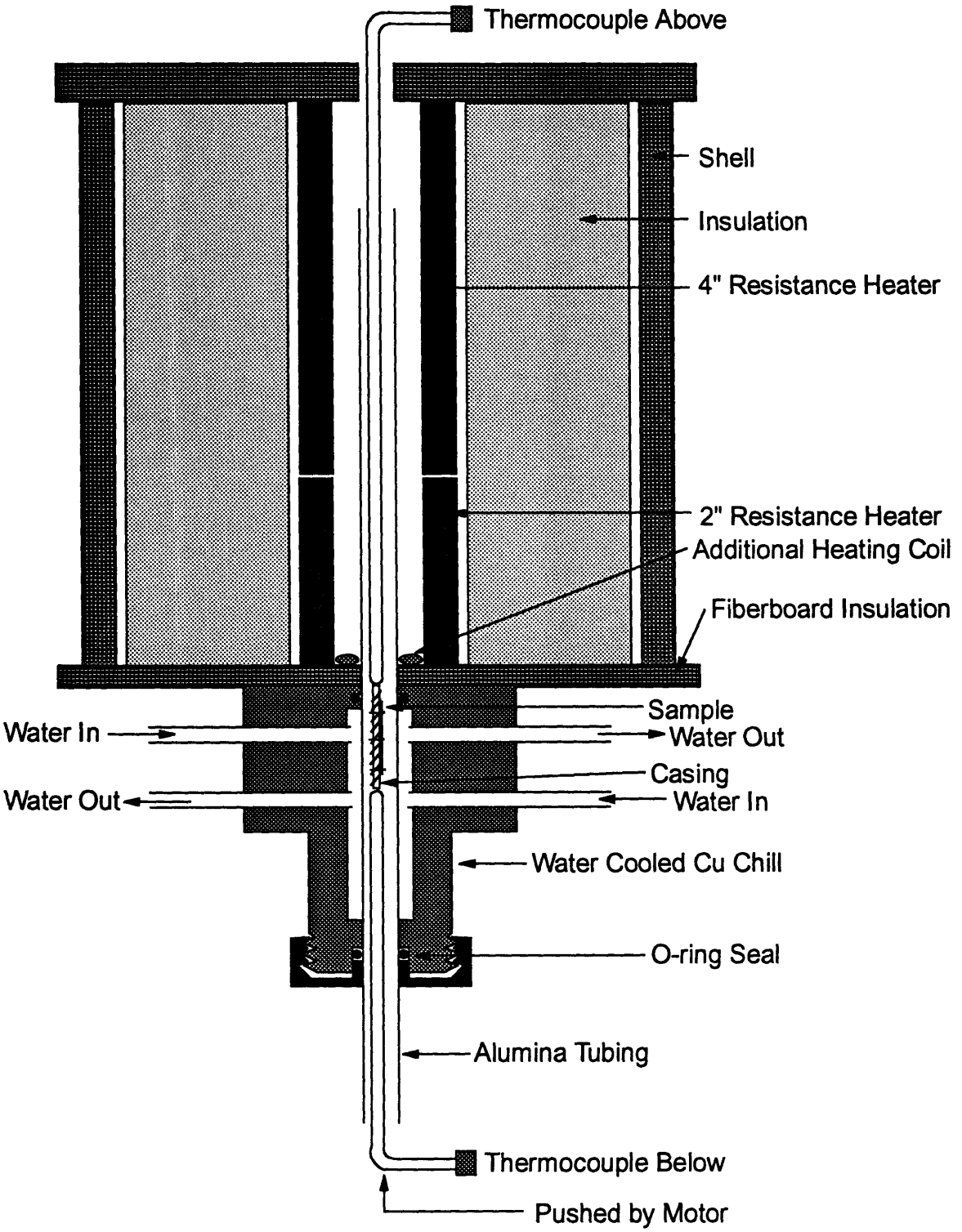

Figure 2-1. Temperature gradient furnace.

independently controlled zones. The lower portion of the furnace is heated by a cylindrical resistance heating element with a 1 inch inner diameter and a height of 2 inches. This element is controlled by an Omega controller model CN5001K2 and an Omega solid state relay model SSR240D45. The upper portion of the furnace is heated by a cylindrical resistance heating element with a 1 inch inner diameter and height of 4 inches. This element is controlled by an Omega controller type CN310-K-C. These elements are surrounded by fiberfrax insulation and a 6 inch diameter shell. The top and bottom of the furnace are covered with 1/4 inch insulating fiberboard with a 1/4 inch in diameter opening at the center. Just below the bottom of the furnace is a water cooled copper chill. An alumina tube travels through the chill and the center of the furnace. This tube is pushed further into the furnace by an Electro Motor Control Corp. motor type NSH-33RJ controlled by a Minirik Electric Co. speed controller model SH83HF.

The samples are loaded attached to small pieces of alumina thermocouple casing in order for the sample to be pushed through the temperature gradient. A cylindrical piece of alumina thermocouple casing 3 cm to 4 cm long is cut in half lengthwise and then wrapped with 0.25 micron Ag wire (approximately 5 wraps per cm). The sample is then attached to the flat edge of the thermocouple casing with Ag wire. The sample and thermocouple casing are then placed inside the alumina tube and stabilized by the placement of type K thermocouples above and below the ends of the thermocouple casing (see Figure 2-1).

The temperatures measured in each of the heating zones as well as above and below the sample are captured by a Kaye Instruments Digistrip II and sent to an IBM PC for storage.

For more information about specific treatments of samples using the temperature gradient furnace see Section 3.4.

Section 2.3 Analysis

2.3.1 Scanning Electron Microscope and Microprobe Analysis

All samples were prepared for scanning electron microscope (SEM) and microprobe analysis by mounting in epoxy and polishing with a 0.05 micron alumina solution.

All SEM analysis was done on two Jeol Superprobe 733 machines. Both systems were equipped with a NORAN 5500/5600 system for automation. This is a series II x-ray microanalysis system. The system is equipped to do both energy dispersive analysis (EDS) and wavelength dispersive analysis (WDS). One SEM had five WDS spectrometers and the other SEM had four WDS spectrometers. The system is fully automated; automation includes the stage, the spectrometers, the counting, the data reduction, and the on-line implementation of the ZAF matrix correction.

The conditions that were used for this work include a beam current of 10 nA, an accelerating voltage of 15 kV, and a focused probe diameter of 1 micron.

The standards that were used for calibration are listed in the following table along with the spectrometer crystal and the x-ray line that was used for the measurements.

Table 2.1 Standards for calibration of microprobe analysis.

Element	Standard	X-ray Line	Spectrometer Crystal
Y	YAG (Y-Al-Garnet)	L_α	TAP
Yb	YbF_3	M_α	TAP
Ba	$BaSO_4$	L_α	PET
Cu	CuO	K_α	LIF
Ag	Ag	L_α	PET

2.3.2 SQUID Measurements of Critical Transition Temperature

All critical transition temperature (T_c) measurements were made on a Quantum Design Magnetic Property Measurement System (MPMS) by measuring magnetic moment as a function of temperature. The MPMS system integrates a SQUID (Superconducting QUantum Interference Device) magnetic field detection system and a superconducting magnet with stable temperature control and a distributed process control system. The system is fully automated with a menu-driven touch screen. The SQUID control system is a Quantum Design model 2000 VHF SQUID Control Unit which has a 200 MHz rf System with external feedback and an intrinsic flux noise less than $1 \times 10^{-4}\ \phi_o/\sqrt{\text{Hz}}$. The computer controller is a Hewlett-Packard Touch Screen II Computer. The temperature is controlled by He gas flow (approximately 1 Pascal) through the sample chamber and heaters located in an annular region outside the sample chamber.

The temperature stability is within 0.05 K. The field stability is 1 ppm/hour. The range of measurement is ±2 emu and the differential sensitivity is 1 x 10^{-6} emu in a 2 T magnetic field. The field resolution is 1 G and the intrinsic field uniformity is 0.01% over the length of the measuring coils.

All measurements were made with an applied magnetic field of 30 G. The T_c measurements were made from 10 K to 100 K. For more information on the results of the measurements see Section 3.7.1.

2.3.3 Four Point Probe Measurement of Critical Current Density

All measurements of critical current density (J_c) were made using the four point probe method. Four leads are attached to a sample using Ag paint to make electrical contact. Two of the leads supply a current while the other two leads are used to measure the resulting voltage as shown in Figure 2-2. After the leads are attached, the sample is cooled by submerging in liquid nitrogen (77 K) or liquid helium (4.2 K). For more information on the results of the measurements see Section 3.7.2.

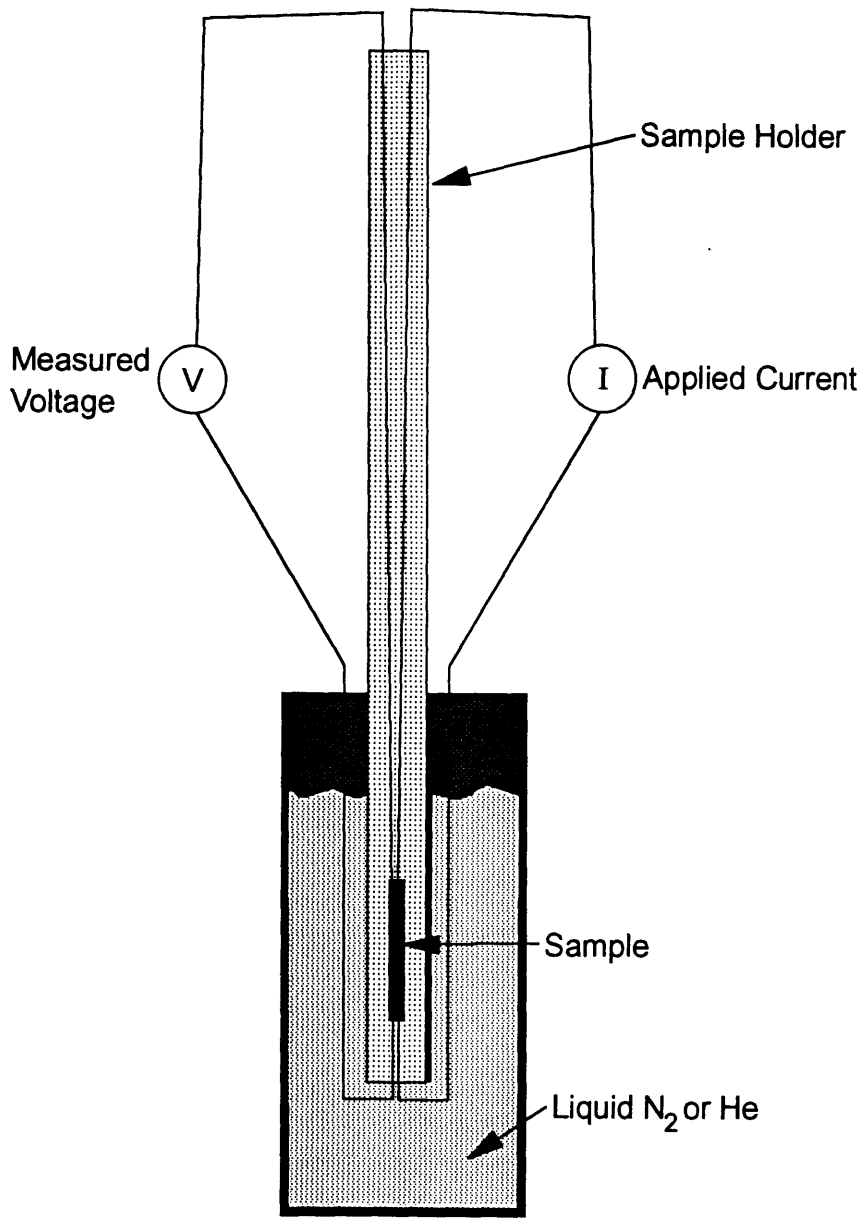

Figure 2-2. Four point probe method for measuring critical current density (J_c).

Chapter 3. Results

The experimental results presented in this chapter are divided into sections according to processing stage. Section 3.1 concerns the starting ribbon. Results of the low temperature oxidation stage are in Section 3.2. Results of the high temperature transformation stage are in Section 3.3. Section 3.4 covers the results of thermal gradient processing during the high temperature transformation stage. Section 3.5 contains the results of isothermal annealing. A subsection at the end of each of Sections 3.2 to 3.5 contains a summary of the trends seen in the results in that section. Oxygenation results are in Section 3.6. Superconducting property results are in Section 3.7. Section 3.8 contains the results for samples with the starting ribbon composition $Yb_1Ba_2Cu_3Ag_{16}$.

Section 3.1 $Y_1Ba_2Cu_3Ag_{15}$ Starting Ribbon

The as-received ribbon referred to as Y15, nominally $Y_1Ba_2Cu_3Ag_{15}$, was examined using both SEM/microprobe analysis and x-ray diffraction. Figure 3-1 shows an SEM photo of the ribbon Y15 as received. (Unless specified otherwise, all photographs are oriented with the length of the ribbon running left to right and the narrow thickness of the ribbon shown top to bottom. The direction into the page is the width of the ribbon which is typically 2 mm. The photographs are taken between 30% and 70% of the way through the width of the sample.) The microstructure is fairly uniform with a slightly coarser microstructure in a region 17 microns wide near the upper surface with respect

Figure 3-1. Backscatter electron image of as received ribbon Y15 (1200x).

to the photo. Microprobe analysis of this sample gives an average composition of 2.90 at% Y, 8.75 at% Ba, 13.60 at% Cu, 70.43 at% Ag, and 4.33 at% O where the amount of O present is calculated by the difference method. This gives an average composition of $Y_1Ba_{3.01}Cu_{4.69}Ag_{24.28}$. Stating compositions in terms of Cu_3 instead of Y_1 is done frequently in superconductor literature because Cu is less volatile than Y or Yb. All compositions in this document will be normalized to Cu_3. In this case the composition is $Y_{0.64}Ba_{1.93}Cu_3Ag_{15.54}$; thus, the actual composition shows that the sample contains slightly less Y than desired. The microprobe analysis measurements show that the central region is slightly closer to the desired composition ratio than the outer regions. The upper region is deficient in Y and has excess Cu, while the lower region is slightly rich in Y and Cu and poor in Ba.

Section 3.2 Low Temperature Oxidation

Samples were first subjected to variations in processing during the low temperature oxidation stage. This stage was intended to allow the oxidation of the metallic precursor to form elemental metal oxides. Three benchmark oxidation treatments were used for the majority of samples, while a few individual treatments were each used on one or two samples. All of the low temperature oxidation processing was done in furnace R (see Section 2.2.2 for a description of the furnace).

One of the benchmark oxidation treatments consisted of a temperature ramp of 5°C/min from room temperature to 140°C and 0.5°C/min from 140°C to 420°C. This was done in an atmosphere of flowing oxygen. The sample was removed from the furnace and cooled in air as soon as it reached 420°C. This treatment will be referred to as Ox-NH (Oxidation-No Hold). Figure 3-2 shows a typical temperature profile for this ramping procedure. Sample Y15-17, which is shown in Figure 3-3, received only this treatment (note presence of coarser region 14 microns wide near upper surface). Figure 3-4 shows sample Y15-2 which also received only the treatment Ox-NH. The contrast was exaggerated in this image to show the position of the oxidation front. The oxidation front is located 10 microns from the upper edge and 3 microns from the lower edge of the sample. A typical composition in the center of the sample is $Y_{0.73}Ba_{1.55}Cu_3Ag_{12.77}$ while in the oxidized zone the average composition is $Y_{0.68}Ba_{1.65}Cu_3O_{6.84}$-$Ag_{16.90}$ (note that this notation is used for convenience to state an overall ratio of Y:Ba:Cu:O:Ag and not to represent the composition of a particular phase). There are small bright nodules visible on the upper surface of sample Y15-2 in Figure 3-4. These nodules are composed of Ag.

Table 3.1 contains a complete listing of all samples and their processing treatments in chart form. The samples which received the treatment Ox-NH may be identified by the "Ox-NH" in the oxidation column. This treatment may also be seen schematically in Figure 3-5. Figure 3-5 contains a representation of the

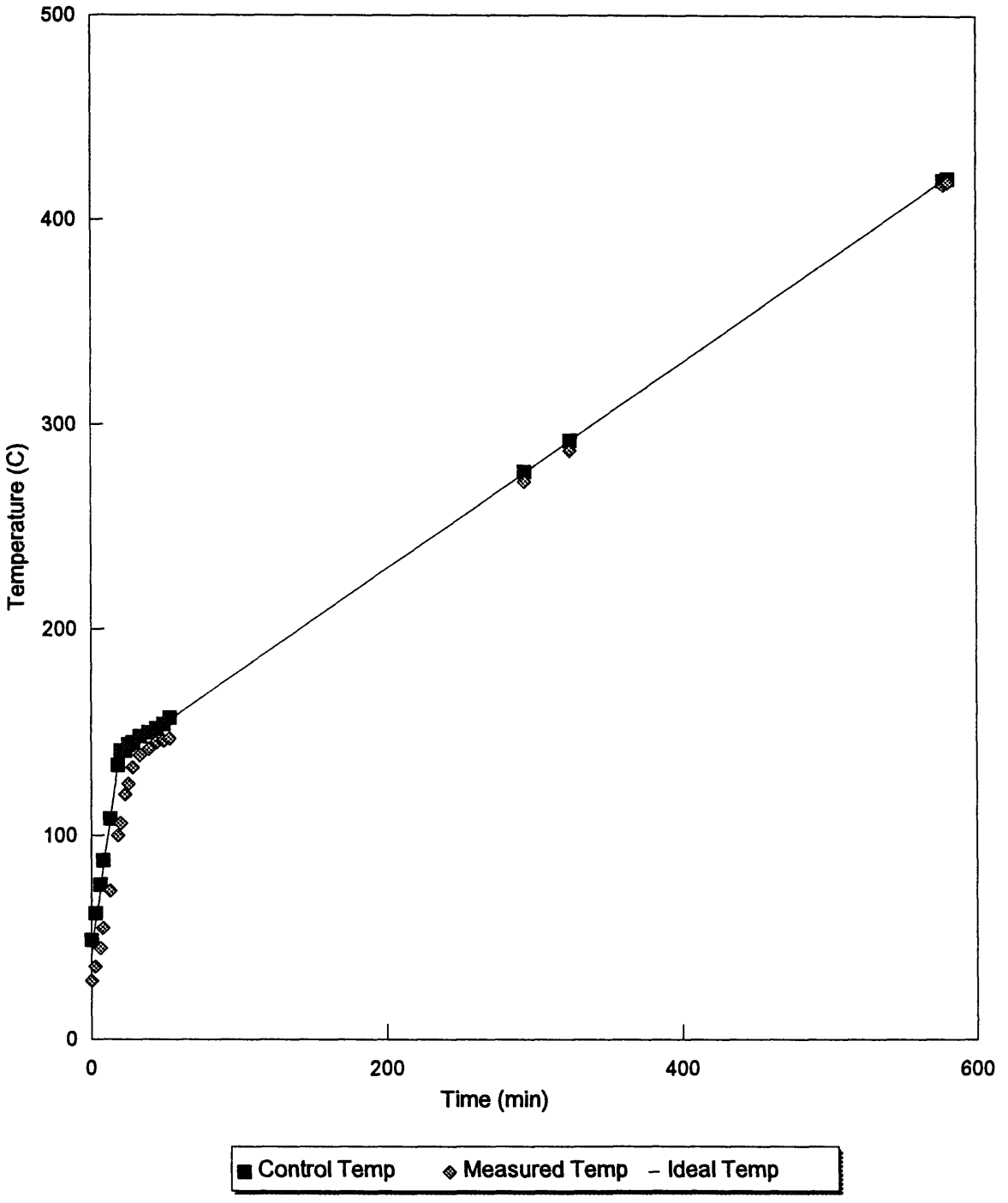

Figure 3-2. Typical temperature profile for Ox-NH and Ox-13 ramp of 5°C/min from room temperature to 140°C and 0.5°C/min to 420°C.

Figure 3-3. Secondary electron image of ribbon Y15-17 which received treatment Ox-NH (1600x).

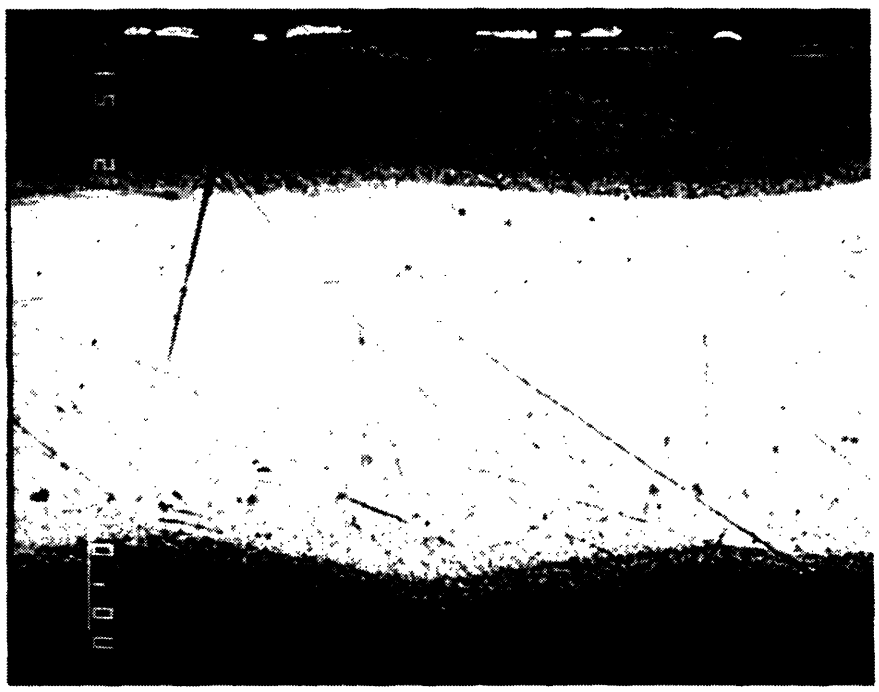

Figure 3-4. Backscatter electron image of ribbon Y15-2 which received treatment Ox-NH with contrast exaggerated to show the oxidation front (2000x).

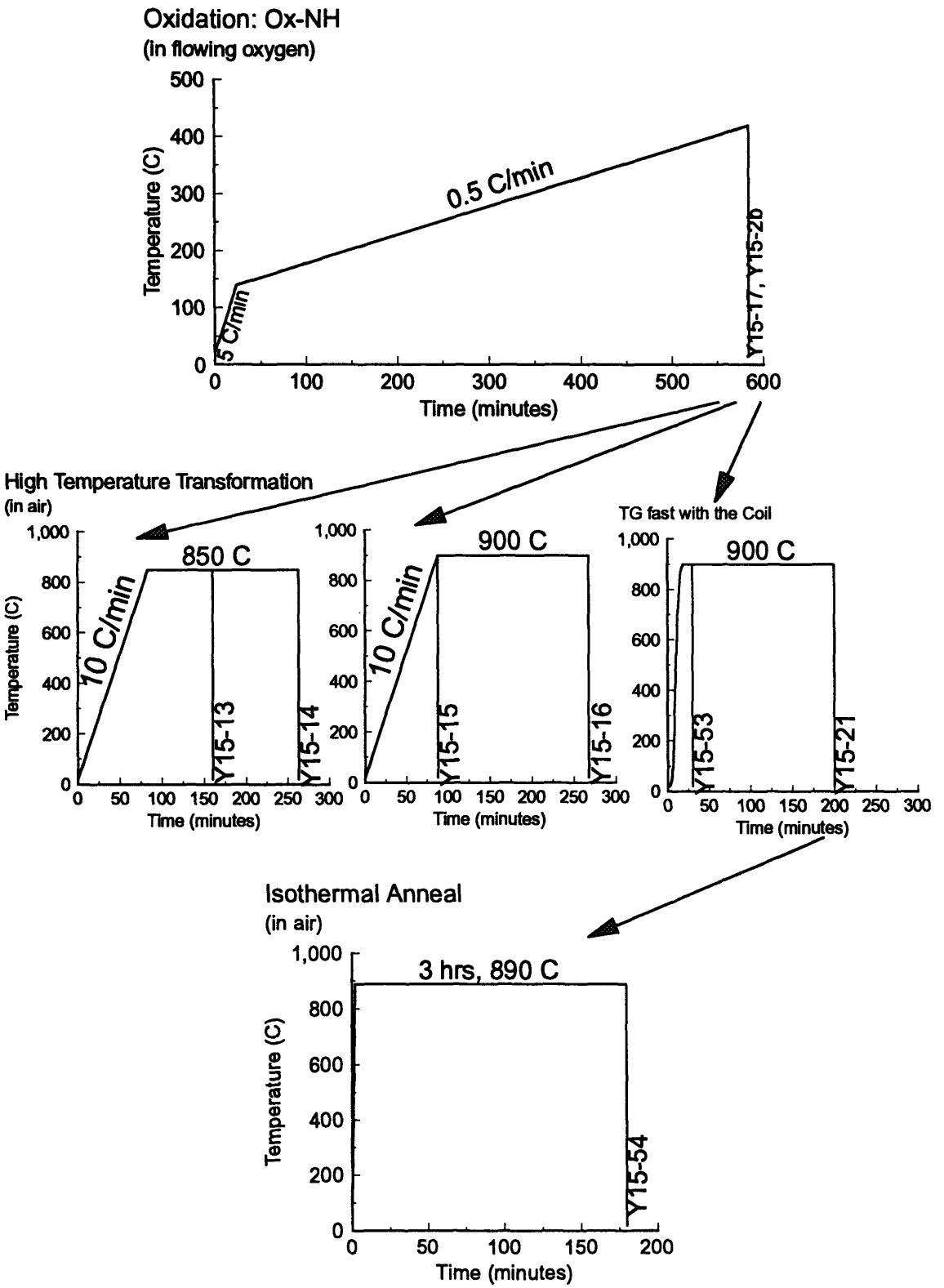

Figure 3-5. Schematic representation of temperature versus time treatments for samples which received Ox-NH.

Table 3.1. List of all samples and their processing treatments.

Sample	Oxidation Treatment	High Temperature Transformation Treatment	Isothermal Anneal
Y15-4	No-Ox	10°C/min to 900°C, hold 3 hrs	
Y15-6	No-Ox	5°C/min to 900°C, hold 3 hrs	
Y15-8	No-Ox	TG slow to 900°C, hold 3 hrs	
Y15-9	No-Ox	10°C/min to 900°C, no hold	
Y15-11	No-Ox	TG slow to 900°C, no hold	
Y15-2, Y15-17	Ox-NH		
Y15-13	Ox-NH	10°C/min to 850°C, hold 1 1/4 hrs	
Y15-14	Ox-NH	10°C/min to 850°C, hold 3 hrs	
Y15-15	Ox-NH	10°C/min to 900°C, no hold	
Y15-16	Ox-NH	10°C/min to 900°C, hold 3 hrs	
Y15-21	Ox-NH	TG fast with coil to 900°C, hold 3 hrs	
Y15-53	Ox-NH	TG fast with coil to 900°C, hold 10 min	
Y15-54	Ox-NH	TG fast with coil to 900°C, hold 10 min	3 hrs at 890°C
Y15-33, Y15-35	Ox-13	TG fast to 900°C, hold 3 hrs	
Y15-34, Y15-38	Ox-13	TG fast to 900°C, hold 10 min	
Y15-36a	Ox-13		
Y15-36	Ox-13	TG fast with coil to 900°C, hold 3 hrs	
Y15-39	Ox-13	TG fast to 900°C, hold 10 min	3 hrs at 890°C
Y15-42	Ox-13	TG fast with coil to 895°C, hold 3 hrs	

Sample	Oxidation Treatment	High Temperature Transformation Treatment	Isothermal Anneal
Y15-47	Ox-13	TG fast with coil to 900°C, hold 10 min	
Y15-48	Ox-13	TG fast with coil to 900°C, hold 10 min	3 hrs at 890°C
Y15-49	Ox-13	TG fast with coil to 925°C, hold 10 min	30 hrs at 890°C
Y15-51	Ox-13	TG fast to 925°C, hold 3 hrs	
Y15-68	Ox-13	TG very slow (0.38 cm/hr) to 900°C, no hold	
Y15-70	Ox-13	TG very slow (0.13 cm/hr) to 900°C, no hold	
Y15-72	Ox-13	TG very slow (0.26 cm/hr) to 900°C, no hold	
Y15-43	10°C/min to 420°C in air, hold 14 1/4 hrs		
Y15-44	10°C/min to 420°C in air, hold 14 1/4 hrs		3 hrs at 890°C
Y15-45	10°C/min to 420°C in air, hold 17 1/3 hrs		
Y15-46	10°C/min to 420°C in air, hold 17 1/3 hrs		3 hrs at 890°C
Y15-59a	5°C/min to 420°C in air, hold 4 hrs		
Y15-59	5°C/min to 420°C in air, hold 4 hrs		3 hrs at 890°C
Y15-64	0.5°C/min to 420°C in O_2, hold 8 hrs		
Y15-66	0.5°C/min to 420°C in O_2, hold 4 hrs		
Y15-22	0.5°C/min to 420°C in O_2, hold 2 hrs		
Y15-23	0.5°C/min to 420°C in O_2, hold 3 1/2 hrs		
Y15-24	0.5°C/min to 420°C in O_2, hold 6 hrs		

Sample	Oxidation Treatment	High Temperature Transformation Treatment	Isothermal Anneal
Y15-25	0.5°C/min to 420°C in O_2, hold 8 hrs		
Y15-26	0.5°C/min to 420°C in O_2, hold 13 1/2 hrs		
Y15-27	0.5°C/min to 420°C in O_2, hold 13 1/2 hrs, cool in furnace		
Y15-28	0.5°C/min to 420°C in O_2, hold 2 hrs	10°C/min to 850°C, hold 1 2/3 hrs	
Y15-29	0.5°C/min to 420°C in O_2, hold 3 1/2 hrs	10°C/min to 850°C, hold 1 2/3 hrs	
Y15-30	0.5°C/min to 420°C in O_2, hold 6 hrs	10°C/min to 850°C, hold 1 2/3 hrs	
Y15-31	0.5°C/min to 420°C in O_2, hold 13 1/2 hrs	10°C/min to 850°C, hold 1 2/3 hrs	
Yb16-2	No-Ox	10°C/min to 900°C, no hold	
Yb16-3	Ox-13	TG fast with coil to 870°C, hold 10 min	
Yb16-4	Ox-13	TG fast with coil to 870°C, hold 10 min	3 hrs at 850°C

temperature versus time treatment seen by the samples which received the Ox-NH treatment. The samples Y15-2 and Y15-17 are labeled on the oxidation portion of the page (upper graph) because they received only this treatment. Samples Y15-13, Y15-14, Y15-15, Y15-16, Y15-21, Y15-53, and Y15-54 all received this treatment followed by high temperature transformation treatments which are shown in the lower portion of the figure and will be discussed in Sections 3.3 and 3.4.

Another standard oxidation treatment, which will be referred to as Ox-13, involved the same temperature ramp of 5°C/min from room temperature to 140°C

and 0.5°C/min from 140°C to 420°C (see Figure 3-2) followed by a 13 hour hold at 420°C. This treatment, like Ox-NH, was done in an atmosphere of flowing oxygen. At the end of the 13 hour hold, the sample was removed from the furnace and cooled in air. Sample Y15-36a received only this treatment. Figure 3-6 shows an SEM photo of this sample. The dark features 3 to 4 microns in diameter near the center of the sample are very rich in Ba and Cu. The surrounding area in the center of the sample is Cu depleted, and the thick regions of the sample have a composition of $Y_{0.98}Ba_{2.24}Cu_3O_{5.66}$-$Ag_{16.72}$. Thus, when the Ba and Cu segregation occurs, the remaining composition more closely resembles the ideal 1:2:3 ratio. The hold time was sufficient to allow the oxidation front to progress to the center of the samples given this treatment. Microprobe analysis showed that there is over 20 at% O everywhere in the sample, including at the center. The Ag nodules at the surface of this sample are approximately 2 microns thick and cover 80 % of the surface. The treatment Ox-13 is represented in the sample listing in Table 3.1 by an "Ox-13" in the "Oxidation" column. Figure 3-7 contains a schematic representation of the temperature versus time treatments of samples which received the Ox-13 treatment. Samples Y15-33, Y15-34, Y15-35, Y15-36, Y15-38, Y15-39, Y15-42, Y15-47, Y15-48, Y15-49, Y15-51, Y15-68, Y15-70, and Y15-72 received the Ox-13 treatment followed by further processing which will be explained in Sections 3.3 - 3.5.

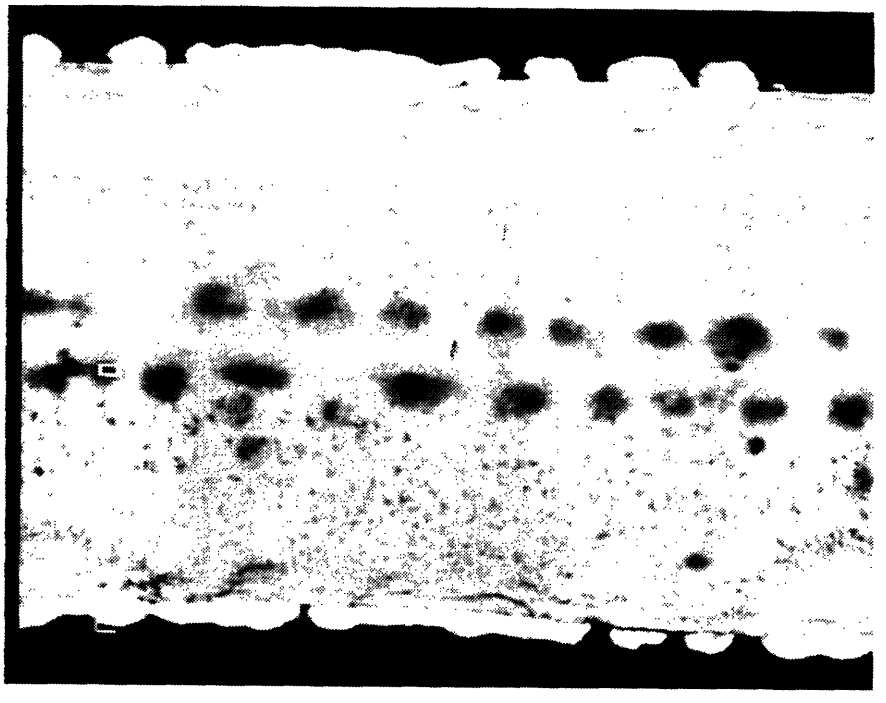

Figure 3-6. Backscatter electron image of ribbon Y15-36a which received treatment Ox-13 (1500x).

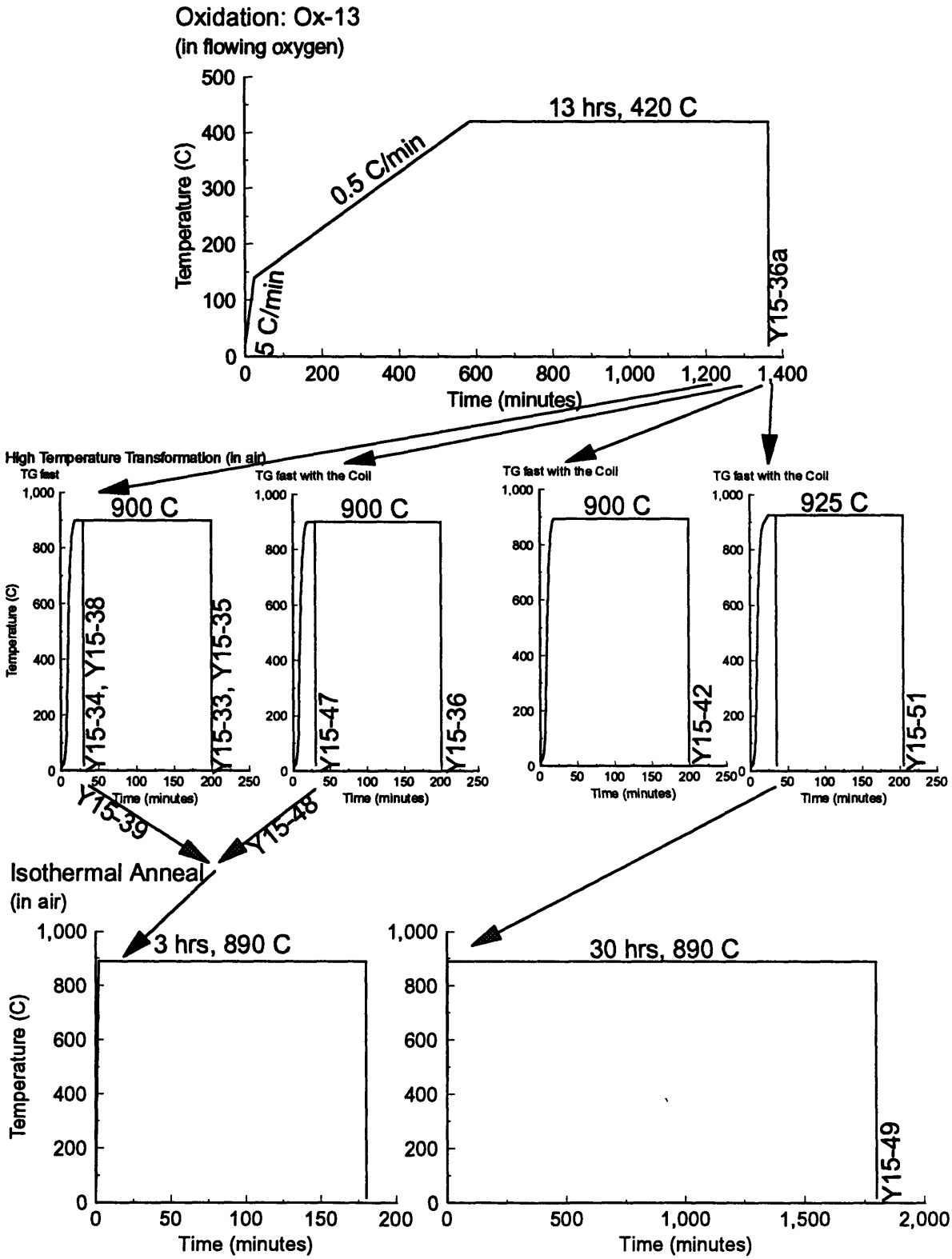

Figure 3-7. Schematic representation of temperature versus time treatments for samples which received Ox-13.

Some samples received no oxidation stage treatment. These samples were processed directly to the high temperature transformation stage. This treatment will be referred to as No-Ox and is represented by No-Ox in the oxidation column of the sample listing in Table 3.1. Samples Y15-4, Y15-6, Y15-8, Y15-9, and Y15-11 received this treatment followed by further processing (see Figure 3-8).

Samples Y15-66 and Y15-64 received an oxidation stage treatment in which the sample was heated 0.5°C/min to 420°C in flowing oxygen and held for 4 hours and 8 hours, respectively. An oxidation front is located 10 and 18 microns from the surface of sample Y15-66, and 18 and 24 microns from the surface of sample Y15-64. Elemental dotmaps of each of the elements present in these samples were taken. All of the dotmaps show the elements distributed evenly throughout the sample, with Ag-rich nodules at the surface.

Samples Y15-22 through Y15-27 received an oxidation stage treatment that involved heating the sample at 0.5°C/min from room temperature to 420°C in flowing oxygen with a variable hold time at 420°C. The hold times were 2 hours, 3 1/2 hours, 6 hours, 8 hours, and 13 1/2 hours for samples Y15-22, Y15-23, Y15-24, Y15-25, and Y15-26, respectively. Sample Y15-27 had a hold time of 13 1/2 hours and was cooled in the furnace in flowing oxygen. In order to remove one of the samples from the furnace, the crucible containing all of the samples was removed from the furnace briefly. After removing the desired sample, the remaining samples were returned to the furnace for the additional

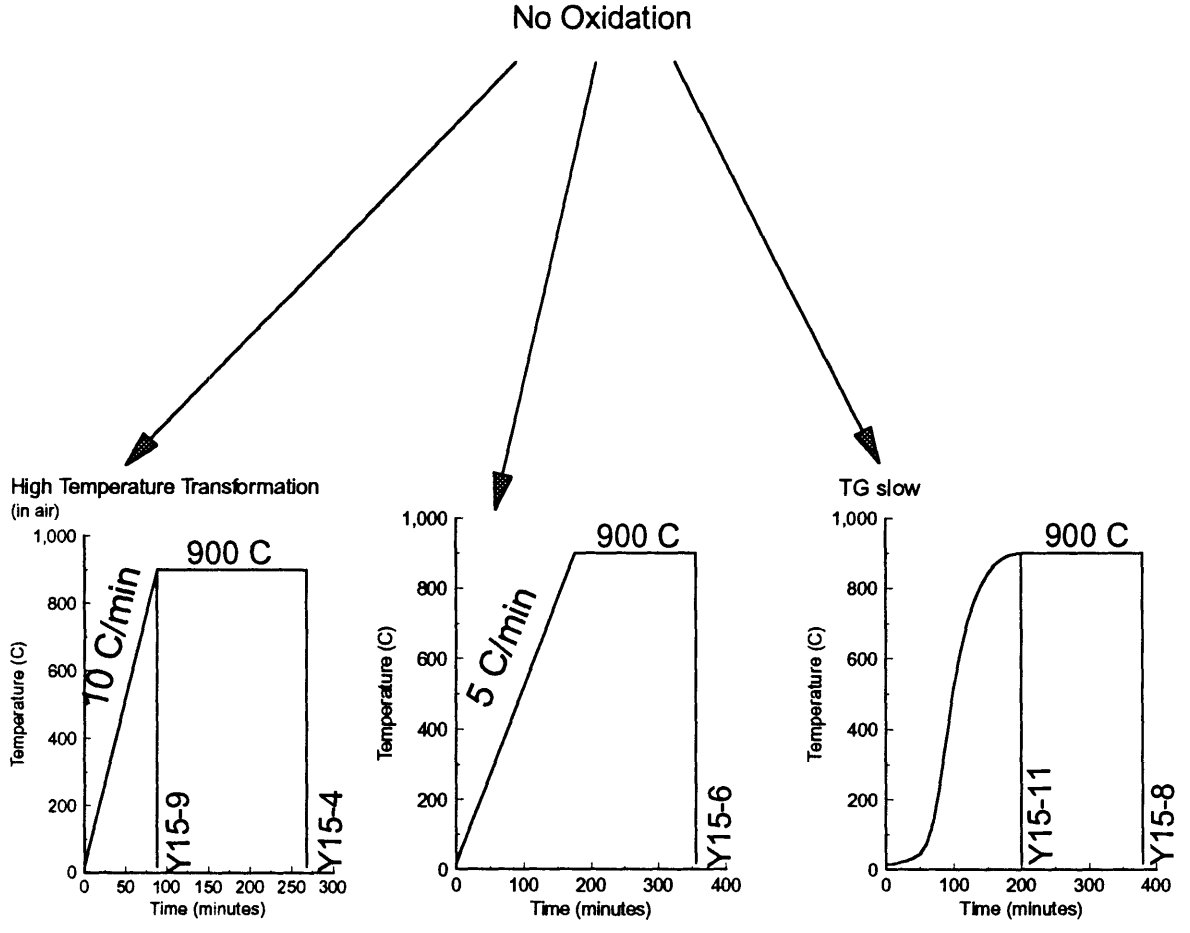

Figure 3-8. Schematic representation of temperature versus time treatments for samples which received No-Ox.

hold time. Thus, when sample Y15-22 was removed from the furnace at the end of the 2 hour hold, samples Y15-23 to Y15-27 were exposed to a decrease in temperature and in partial oxygen pressure (to air). When a sample was removed from the furnace at the end of the hold time, it was cooled in air. Figure 3-9 shows schematically the temperature versus time treatments of these samples. A vertical line indicates that a sample was removed from the furnace at that point and cooled in air. The line labeled Y15-27 is slanted to indicate slower cooling inside the furnace. This cooling is done in the treatment atmosphere of flowing oxygen.

SEM/microprobe analysis was used to produce elemental dotmaps to illustrate the movement of the various elements during this treatment (see Section 2.3.1 for an explanation of the procedure used to obtain these). In sample Y15-22, shown in Figure 3-10, there is Ba enrichment at the surface, then a wide region (17 to 19 microns) where Ba and Cu are slightly depleted, and a central region 11 microns wide where Y and Ag are slightly depleted. In sample Y15-24, shown in Figure 3-11, a very narrow region of Cu enrichment (1 micron wide) exists at approximately the location of the edges of the central region in Y15-22. The central area surrounded by these narrow Cu enriched regions is 5 to 11 microns wide and is Cu depleted. Less Ba surface enrichment is visible in this sample. In sample Y15-25, Ba, Cu, and Ag each appear to be distributed evenly throughout the sample. Y is evenly distributed in an outer region 12 to 14 microns thick and forms clusters of Y enriched areas surrounded

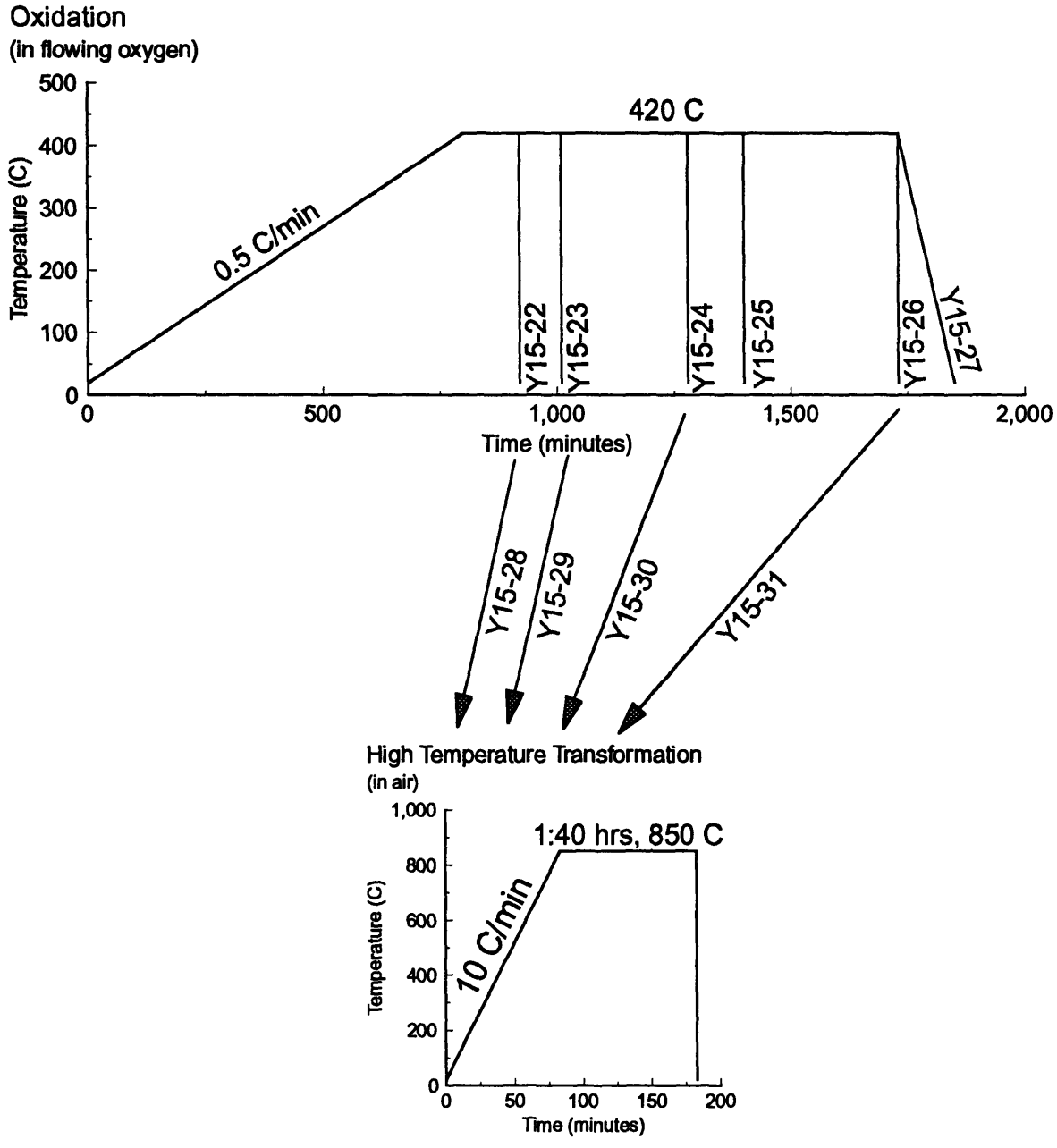

Figure 3-9. Schematic representation of temperature versus time treatments for samples Y15-22 to Y15-31 which received oxidation 0.5°C/min to 420°C in flowing oxygen with various hold times.

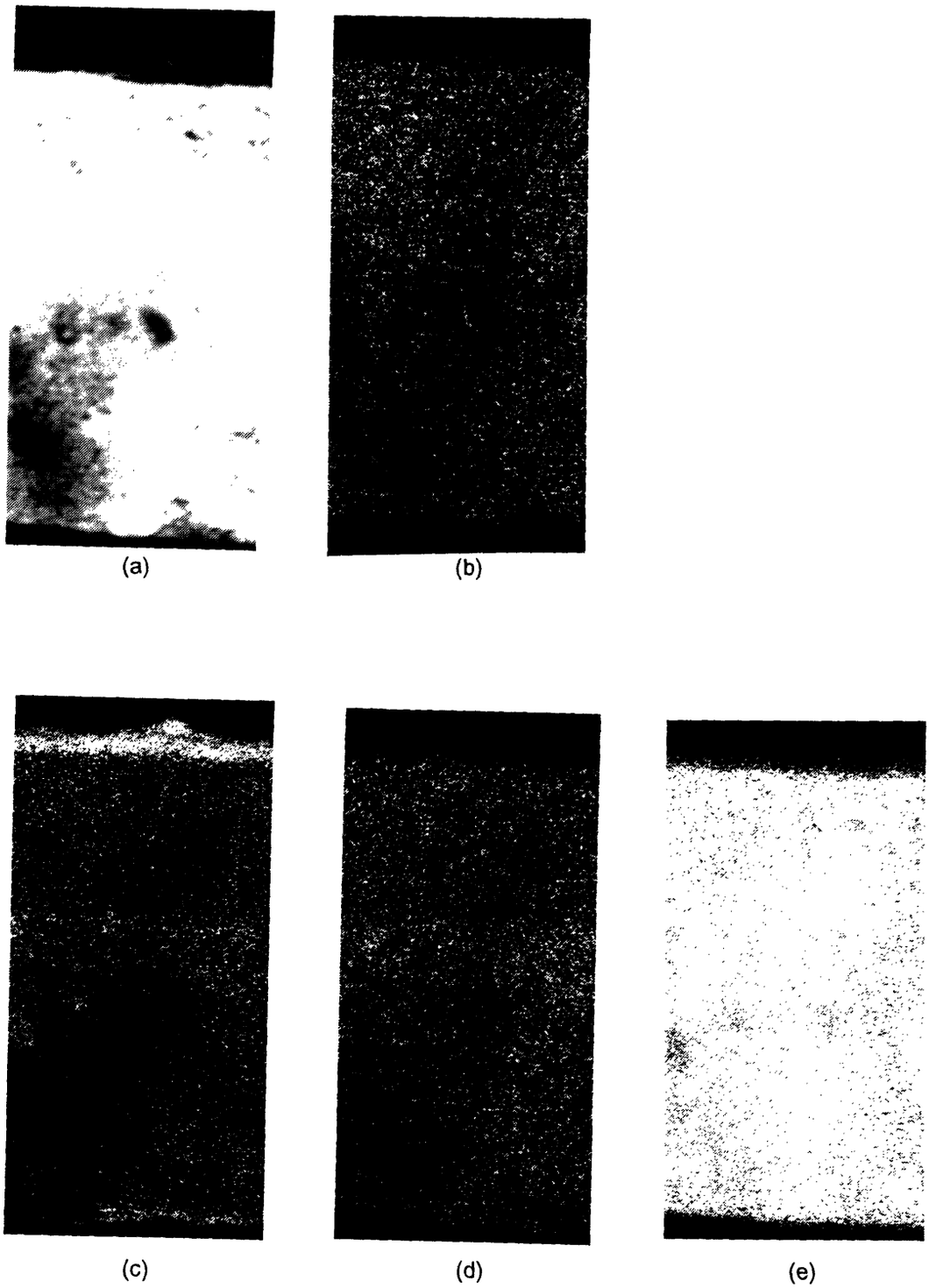

Figure 3-10. Sample Y15-22 (a) backscatter electron image; (b) Y dotmap; (c) Ba dotmap; (d) Cu dotmap; and (e) Ag dotmap (1000x).

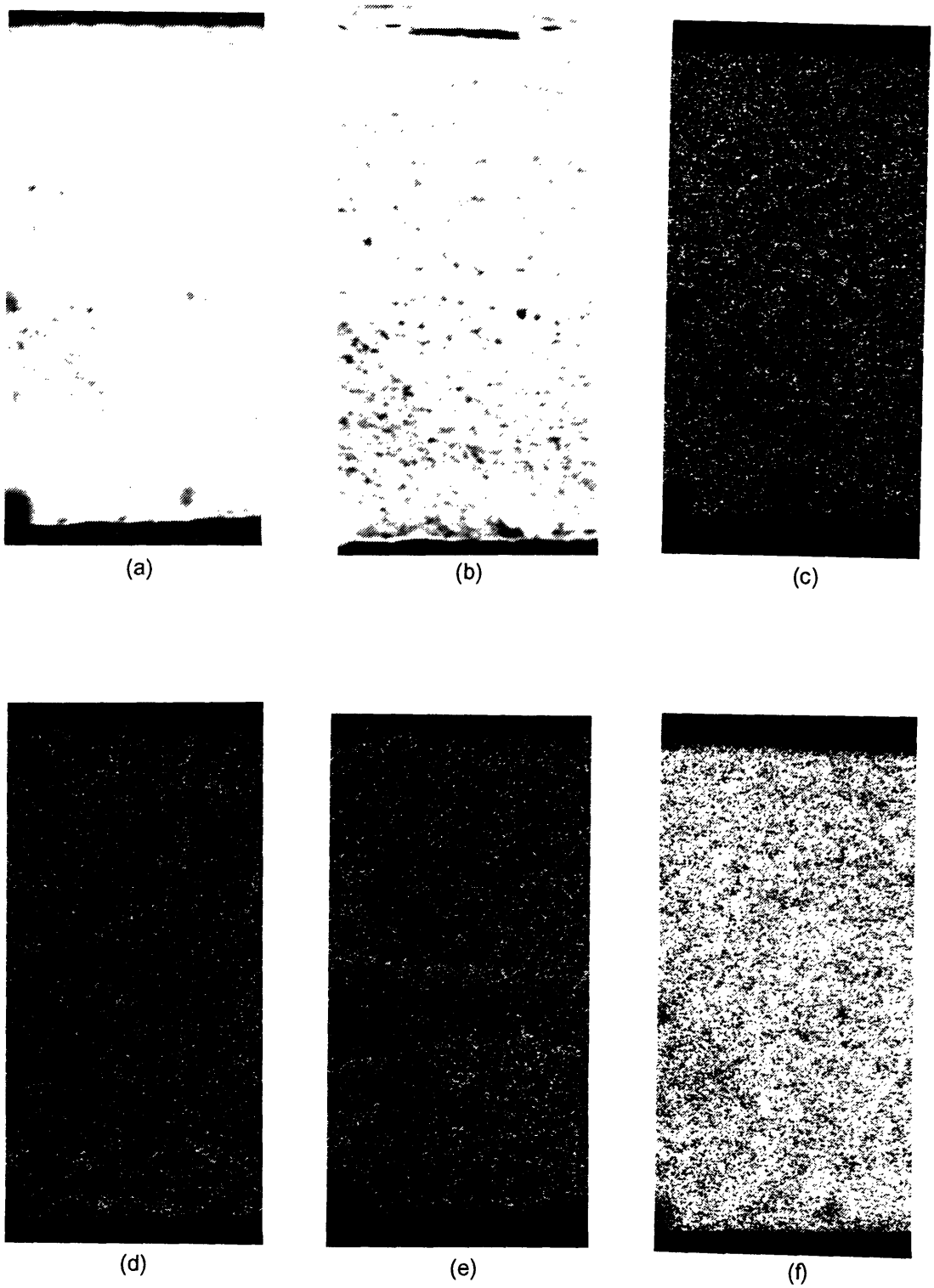

Figure 3-11. Sample Y15-24 (a) backscatter electron image; (b) secondary electron image; (c) Y dotmap; (d) Ba dotmap; (e) Cu dotmap; and (f) Ag dotmap (1000x).

by Y depleted areas in the central region. In sample Y15-27, shown in Figure 3-12, the Y clusters in the central region are more pronounced, Ba enrichment at the surface is again prevalent, and there is a narrow region of Y, Cu and Ag 1 to 2 microns thick at a distance of 10 microns from one surface. Samples Y15-28, Y15-29, Y15-30 and Y15-31 were given the same treatment as samples Y15-22, Y15-23, Y15-24, Y15-26, respectively, and followed by further processing.

A few samples received oxidation treatments in air instead of flowing oxygen; these samples will each be considered individually. Sample Y15-59a was heated 5°C/min to 420°C in air and held 4 hours. The oxidation front was located an average distance of 13 microns and 8 microns from the upper and lower edges of the sample, respectively. Microprobe analysis results show 0 at% O at the center of the sample, a few at% O at locations just behind the oxidation front, and as much as 20 at% O near the outer edges of the sample. Sample Y15-59 received this treatment followed by further processing. Sample Y15-43 was heated 10°C/min to 420°C in air and held 14 hours and 18 minutes. Sample Y15-44 received this treatment followed by further processing. Sample Y15-45 was heated 10°C/min to 420°C in air and held for 17 hours and 22 minutes before being cooled in the furnace. Sample Y15-46 received this treatment followed by further processing. Samples Y15-43 and Y15-45 both have a uniform microstructure similar to that of the bulk of Y15-17 (see Figure 3-3) with no oxidation front visible in the photographs. These treatments may be seen schematically in Figure 3-13.

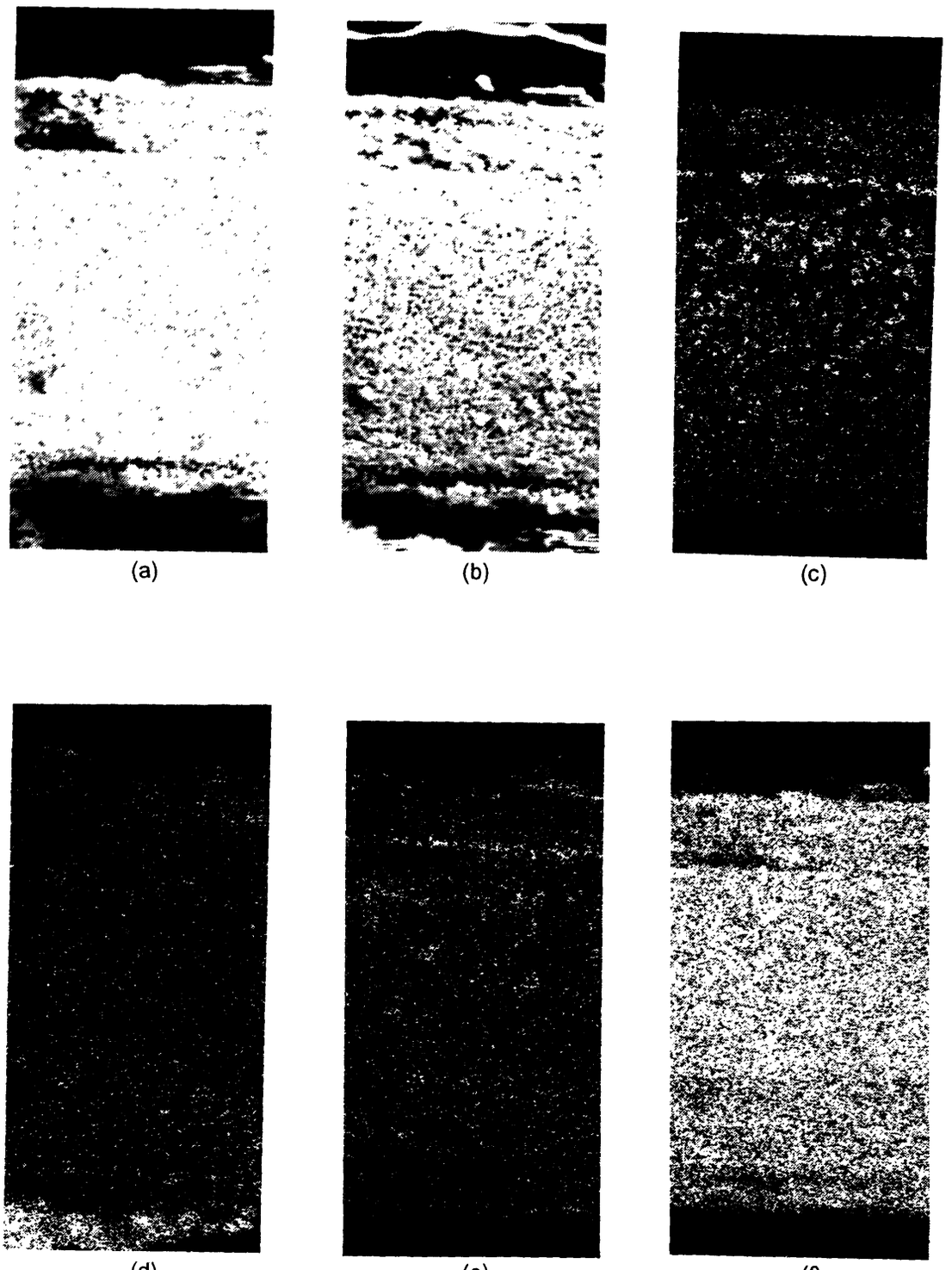

Figure 3-12. Sample Y15-27 (a) backscatter electron image; (b) secondary electron image; (c) Y dotmap; (d) Ba dotmap; (e) Cu dotmap; and (f) Ag dotmap (1000x).

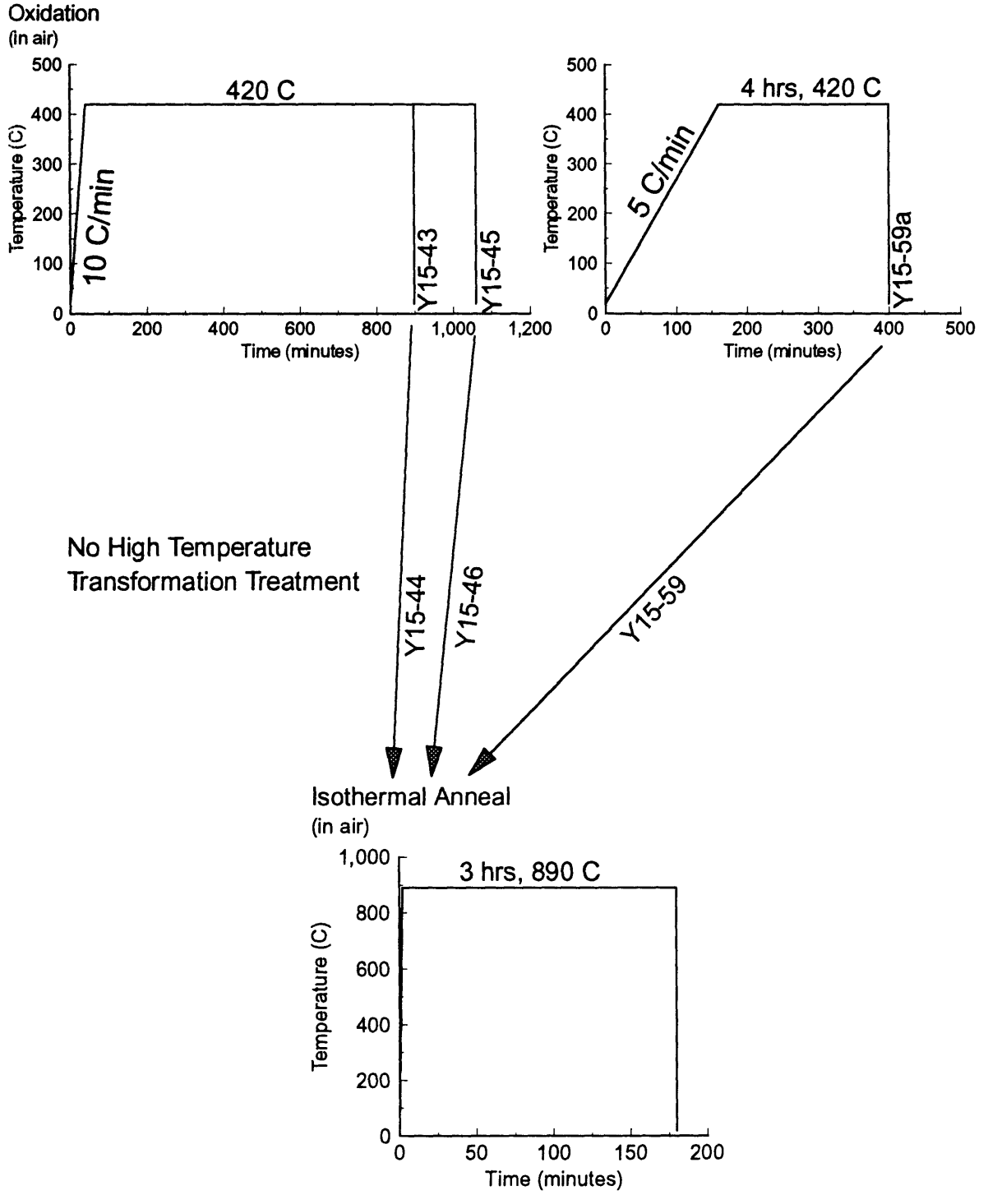

Figure 3-13. Schematic representation of temperature versus time treatments for samples which received oxidation treatments in air.

3.2.1 Summary of Low Temperature Oxidation Results

The effect of the low temperature oxidation stage treatment is illustrated schematically in Figure 3-14. This shows how an initially homogeneous melt-spun precursor ribbon (a) develops Ag nodules at the surface as the internal oxidation zone progresses inward (b). The completely oxidized ribbon (c) has larger Ag nodules at the surface and a solute free region at the center of the ribbon.

Section 3.3 High Temperature Transformation

The high temperature transformation stage was intended to allow the transformation of the elemental oxides formed during the oxidation stage to the desired $Y_1Ba_2Cu_3O_{7-x}$ superconductor phase. The high temperature transformation stage was done at both 850°C and 900°C for various times. Most of these samples were heated in air (in furnace R) at a rate of 10°C/min from room temperature to the desired temperature. Figure 3-15 shows a typical temperature profile for this ramp rate. In all cases, the samples were removed from the furnace at the end of the specified hold time and cooled in air. Table 3.1 contains a summary of the treatments for all of the samples. Refer to Figures 3-5, 3-7, 3-8, 3-9, and 3-13 for schematic representations of the temperature versus time treatments for various samples.

Sample Y15-9, which had no prior oxidation treatment, and sample Y15-15, which had treatment Ox-NH, were heated at the standard 10°C/min to 900°C and

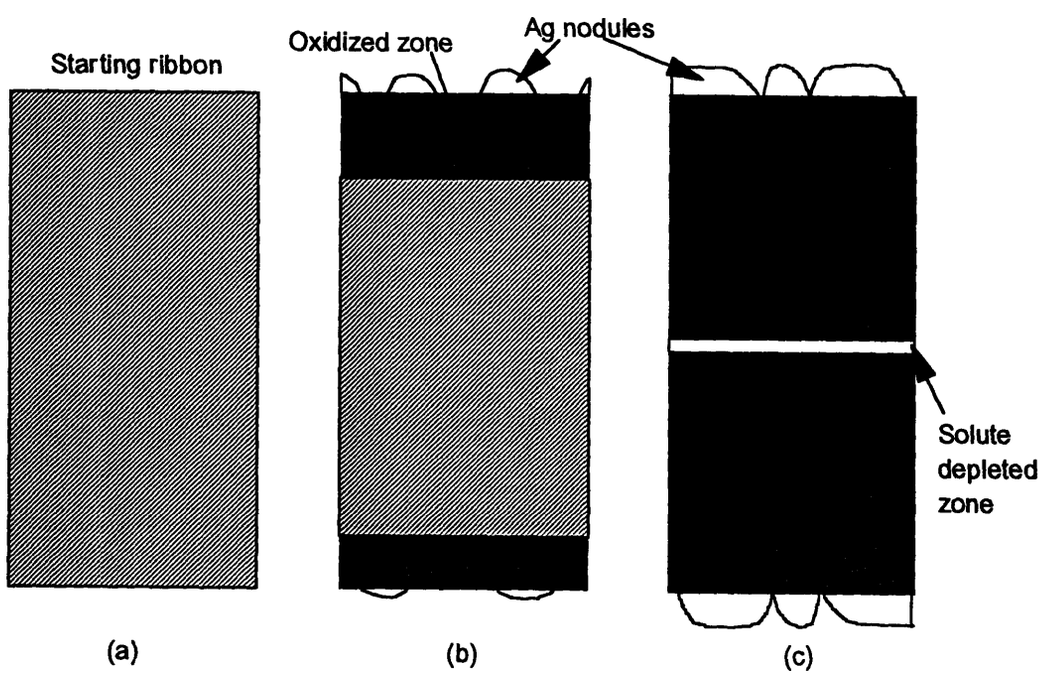

Figure 3-14. Schematic showing effect of oxidation treatment on ribbon microstructure: (a) melt-spun precursor ribbon; (b) partially oxidized ribbon; and (c) completely oxidized ribbon. To see actual microstructures, refer to Figures 3-1, 3-3, and 3-6.

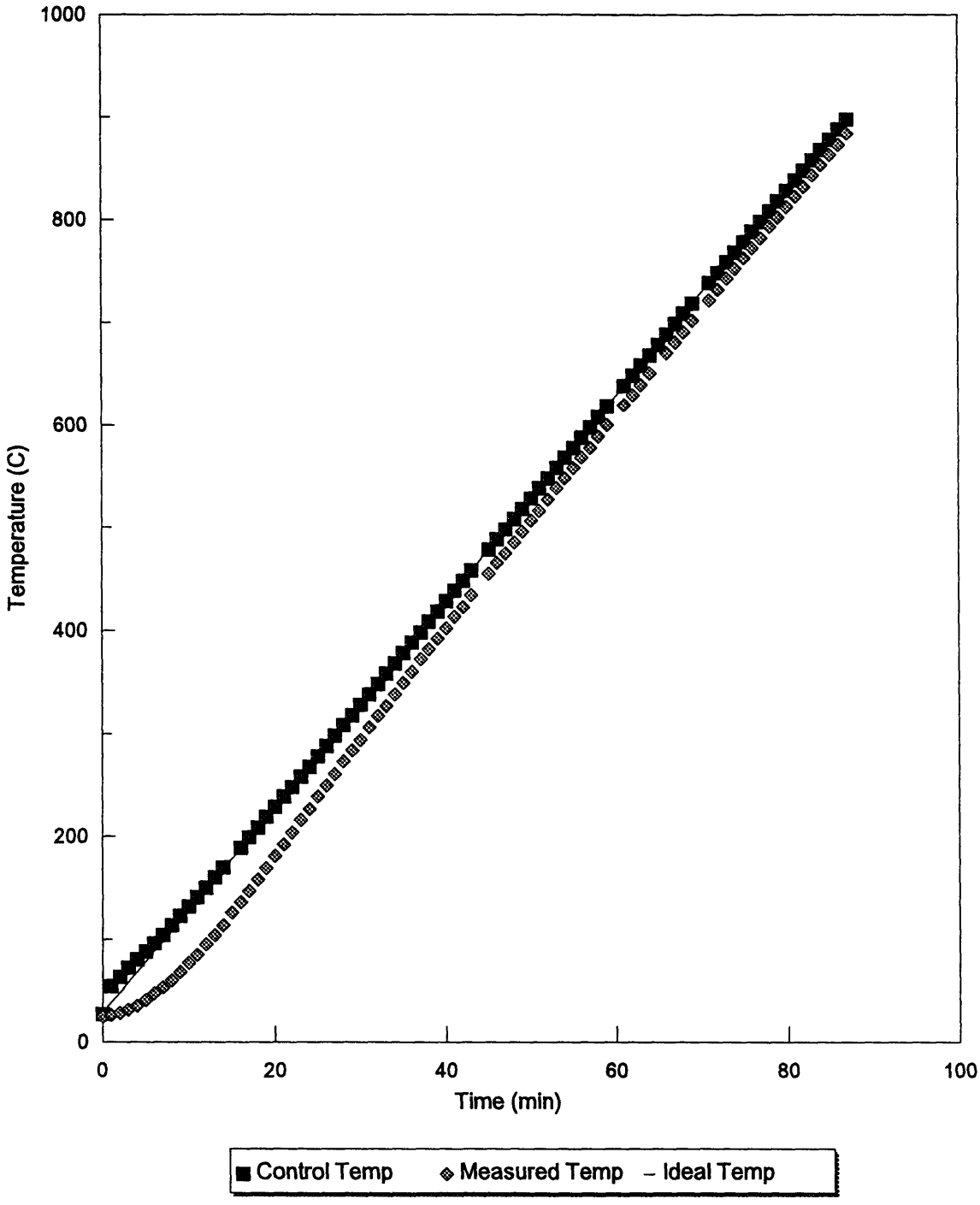

Figure 3-15. Typical temperature profile for ramp of 10°C/min from room temperature to 900°C.

removed immediately (no hold). Figure 3-16 contains an SEM photo of sample Y15-15. In the photo the lighter phase is Ag and the fine gray phase (around 1 micron in diameter) is $Y_1Ba_2Cu_3O_{7-x}$ (oxide phase) as verified by microprobe analysis. The larger gray features (2 to 3 microns in diameter) near the center are CuO. There are two distinct regions in this sample: a coarser central region, and an outer region with a finer microstructure that corresponds to the oxidation zone in the Ox-NH treatment. The boundary of the two regions is located 14 and 23 microns from the edges of the sample. Sample Y15-9 has a uniform microstructure throughout that resembles the central region of Y15-15 with slightly more connectivity between the oxide phase particles.

Sample Y15-4, which had no prior oxidation treatment, and sample Y15-16, which had treatment Ox-NH, were held at 900°C for 3 hours. Figure 3-17 contains an SEM photo of sample Y15-4. Sample Y15-16 has a very similar microstructure. In both cases, the additional time at 900°C resulted in significant coarsening of the oxide phase. The typical size of the oxide phase aggregates is 2 to 3 microns wide and up to 30 or 40 microns long in the plane of the photograph. The oxide phase aggregates are composed of grains of oxide (gray), and areas which appear very dark and are frequently barium cuprates The dark areas are sometimes voids.

Sample Y15-6 received the same treatment as Y15-4 but with a non-standard ramp rate of 5°C/min. That is, there was no prior oxidation treatment and the

Figure 3-16. Secondary electron image of sample Y15-15 (1200x).

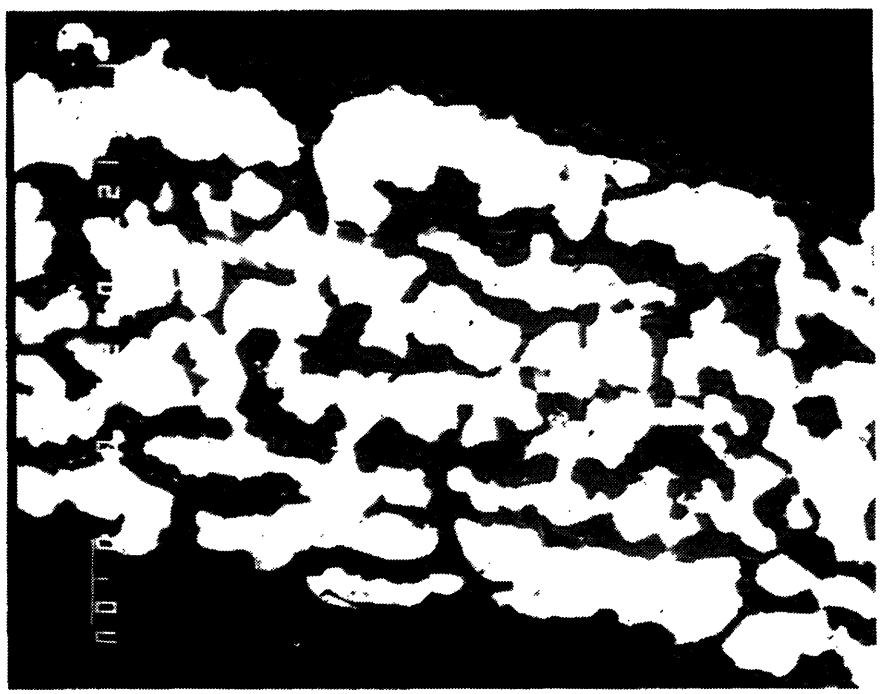

Figure 3-17. Backscatter electron image of sample Y15-4 (1200x).

sample was heated 5°C/min to 900°C in air and held for 3 hours. The sample was then removed from the furnace and cooled in air. Figure 3-18 shows two SEM photos of this sample. This sample is not quite as coarse as Y15-4, having aggregates typically measuring only 1 to 2 microns wide and 20 to 30 microns long. Y15-6 also shows some separation of the microstructure into bands such that one band contains only Ag and the next band contains Ag and the oxide phase as seen in Figure 3-18 (b). The Ag band at the upper surface is 11 microns thick and the Ag band at the center of the sample is 7 to 10 microns thick. There is no Ag band at the lower surface. The two phase Ag/oxide bands are 20 to 25 microns thick (upper band) and 35 to 40 microns thick (lower band).

Samples Y15-13 and Y15-14, which had treatment Ox-NH, were ramped at the standard 10°C/min to 850°C and held there for 1 1/4 hours and 3 hours, respectively. These samples have microstructures very similar to the microstructure of sample Y15-15 shown in Figure 3-16. In sample Y15-13 there is an outer region with a typical oxide phase particle size of less than 1 micron, and a central region with a typical oxide particle size of 1 to 2 microns. The boundaries between the regions are located 8 and 4 microns from the edges of the sample. In sample Y15-14, the oxide phase particles are somewhat elongated having typical dimensions of less than 1 micron by up to 3 microns. There is a higher density of oxide phase particles in the outer region than in the central region. The transition from the outer region to the central region occurs

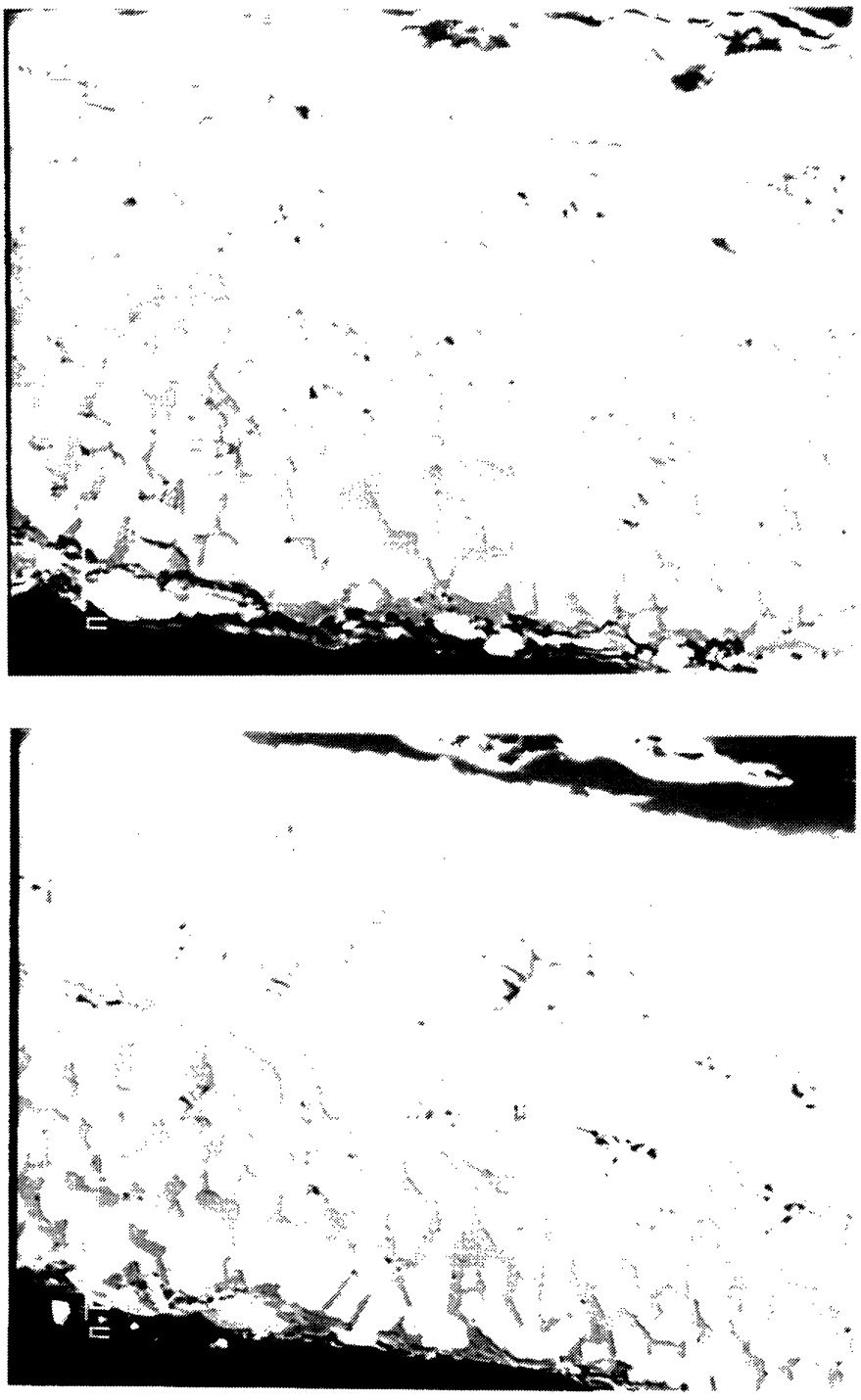

Figure 3-18. Secondary electron images of sample Y15-6 (1000x). Note the presence of Ag and Ag/oxide bands in (b).

at approximately 20 and 15 microns from the edge of the sample but is not as clearly defined as in Y15-15 and Y15-13.

Samples Y15-28 to Y15-31 were ramped 10°C/min to 850°C and held for 1 2/3 hours. In these samples, which had progressively longer low temperature oxidation hold times, the boundary between an outer region and a central coarser region is located 20 to 25 microns from the edge in samples Y15-28 to Y15-30. In sample Y15-31 the boundary has disappeared and a uniform microstructure remains that is like the typical outer region.

3.3.1 Summary of High Temperature Transformation Results

The results of the high temperature transformation treatments are shown schematically in Figure 3-19. A sample which had no prior oxidation and was treated at 900°C for a short time has a uniform microstructure of small isolated oxide particles in Ag. The same treatment on a sample which was partially oxidized resulted in a microstructure which had a finer outer region and a coarser inner region. Samples which received longer hold times at 900°C had microstructures with aggregates of oxide particles in a coarsened microstructure. Samples which were treated at 850°C for short and long hold times had microstructures like those treated at 900°C for short times.

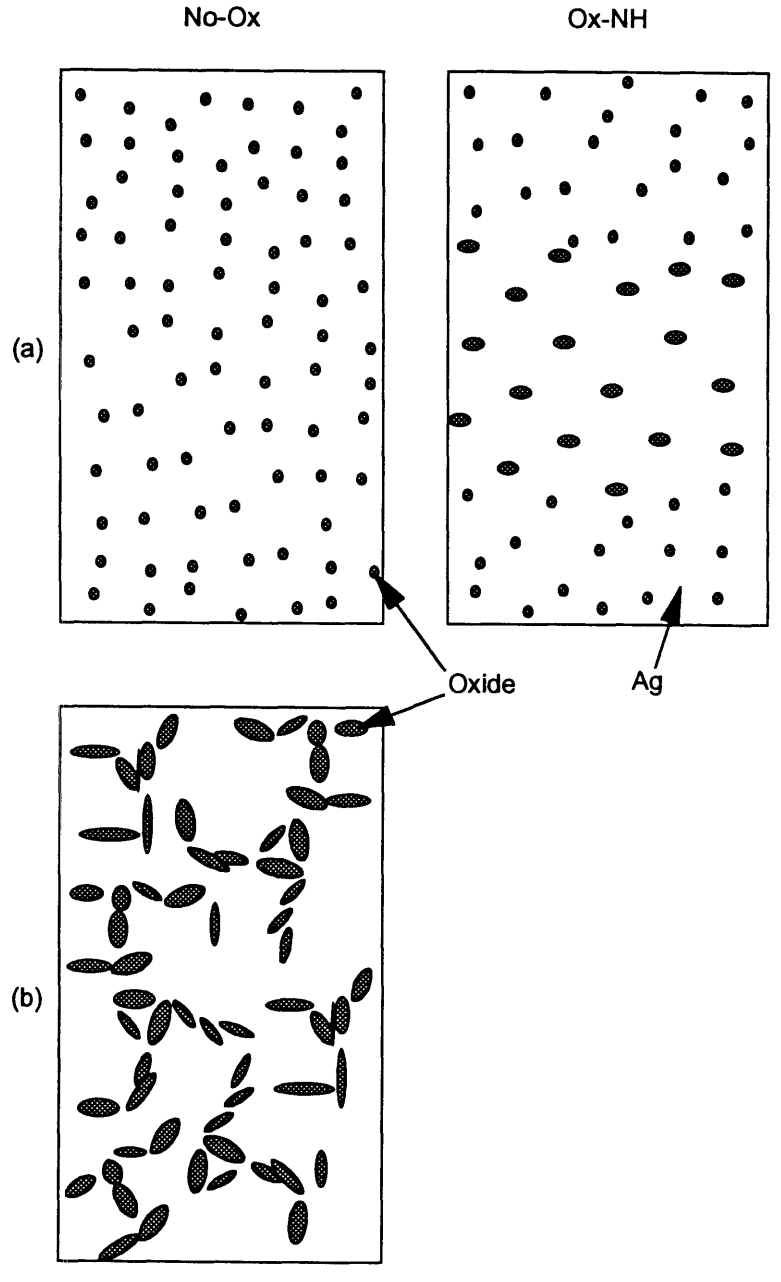

Figure 3-19. Schematic of high temperature transformation treatment results: (a) 900°C for a short hold time or 850°C for short or long hold times; (b) 900°C for long hold time. Note the difference in (a) based on the prior oxidation treatment. To see actual microstructures, refer to Figures 3-16 and 3-17.

Section 3.4 High Temperature Transformation in the Temperature Gradient Furnace

The high temperature transformation stage was also done in a temperature gradient furnace (TG) with different maximum temperatures, different sample velocities, and some experiments were done using an additional heating coil located just above the bottom of the furnace. Several velocities were used; one of approximately 26 cm/hr which is referred to as TG fast, one of approximately 2.8 cm/hr which is referred to as TG slow, and some slower velocities which were each used for only one experiment (exact velocity and maximum temperature ramp rate is given with the detailed results for each sample). TG slow results in a maximum temperature ramp rate of 13°C/min while TG fast results in a maximum temperature ramp rate of 84°C/min. Typical ramping profiles for TG slow and TG fast are shown in Figure 3-20 and Figure 3-21, respectively. The maximum temperatures ranged from 870°C to 900°C. The samples which received these treatments may be identified in Table 3.1 in the High Temperature Transformation Treatment column. The information found there includes the ramp rate (e.g. TG slow), the maximum temperature, and the hold time. The experiments in which the additional heating coil was used are identified as "with coil". For a more detailed description of the furnace or the experimental procedure see Chapter 2.

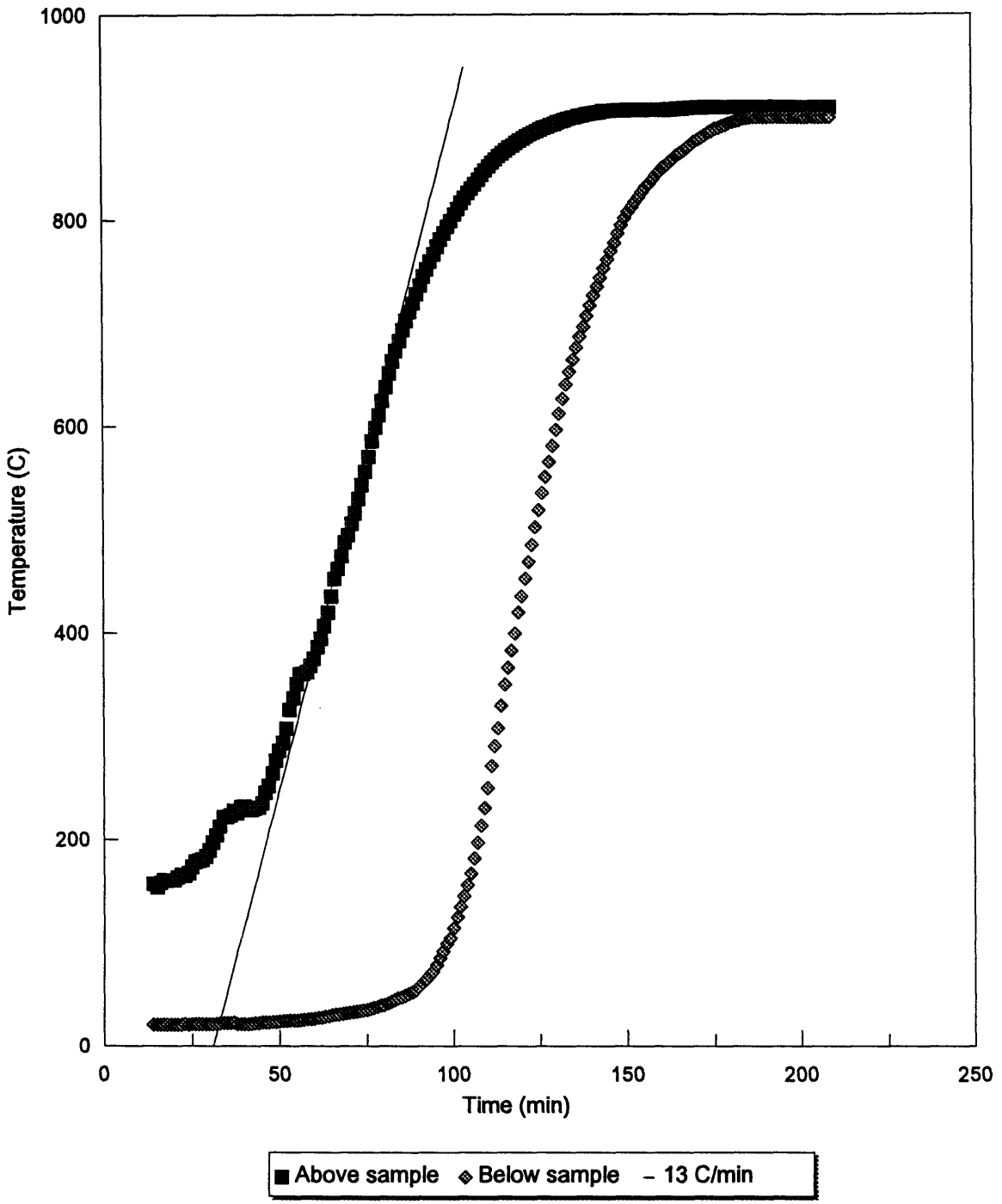

Figure 3-20. Typical temperature profile for ramp of TG slow from room temperature to 900°C.

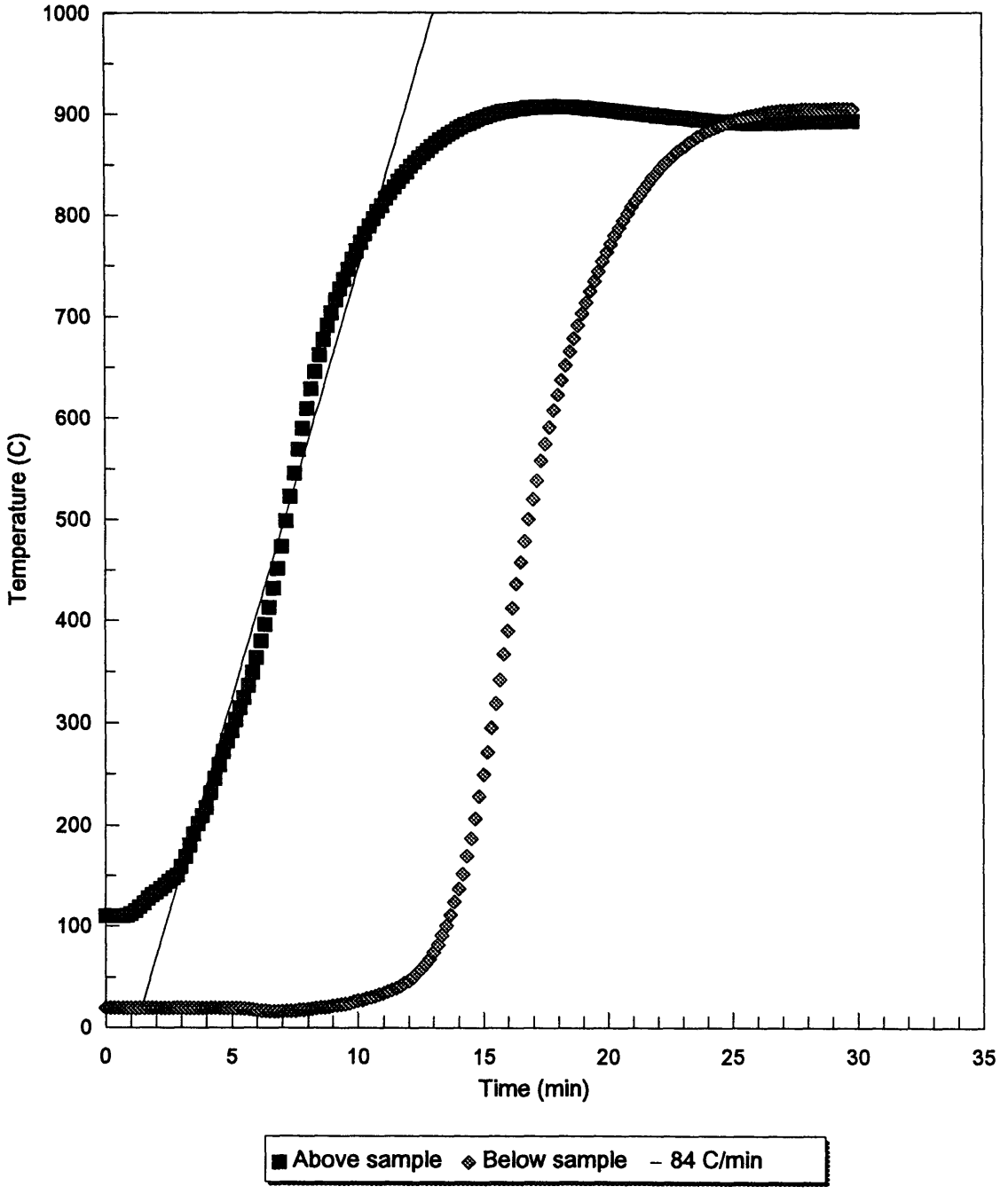

Figure 3-21. Typical temperature profile for ramp of TG fast from room temperature to 900°C.

3.4.1 Temperature Gradient Processing at Slow Velocity

Samples Y15-8 and Y15-11, which had no prior oxidation, were processed in TG slow without the coil, to a maximum temperature of 900°C. Y15-11 was removed immediately and Y15-8 received a 3 hour hold at temperature. Sample Y15-11, shown in Figure 3-22, has an Ag band 5 microns wide clearly present near the center of the sample and a typical oxide particle size of 2 to 5 microns. In sample Y15-8, shown in Figure 3-23, the center Ag band has widened to 12 microns and in some areas there are Ag bands 3 to 6 microns wide present at both surfaces. The oxide phase within the Ag/oxide bands has a typical size of 2 to 3 microns. The oxide phase particles at the edge of the two phase band form a nearly continuous path of oxide that is 2 to 4 microns thick.

3.4.2 Temperature Gradient Processing at Fast Velocity

All of the samples presented in this section were processed in the temperature gradient at the faster velocity. That is, at a velocity of 26 cm/hr which results in a maximum temperature ramp rate of 84°C/min (see Figure 3-21).

Samples Y15-21, Y15-53, and Y15-54, which had treatment Ox-NH, were all processed to a maximum temperature of 900°C with the coil on. Samples Y15-53 and Y15-54 were held for 10 minutes. Sample Y15-54 received a further isothermal anneal (see Section 3.5). SEM photos of Y15-53 showed a variable microstructure with some areas showing a uniform distribution of isolated round

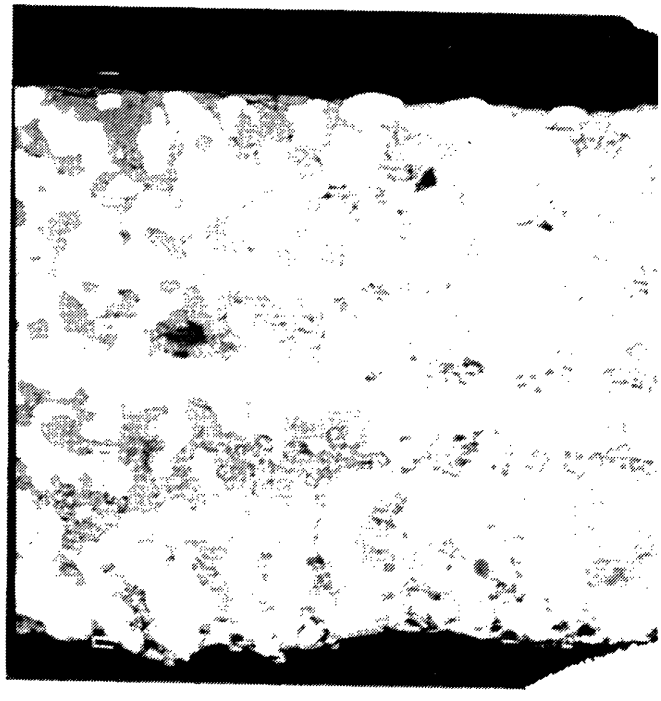

Figure 3-22. Backscatter electron image of sample Y15-11 (1200x).

Figure 3-23. Secondary electron image of sample Y15-8 (1200x).

oxide phase particles typically 2 to 6 microns in diameter and no banding. Other areas have nearly continuous bands of Ag, oxide, and two phase Ag/oxide as seen in Figure 3-24. Sample Y15-21 was held at temperature for 3 hours. This sample showed only occasional tendencies towards forming a central Ag band with many areas appearing nearly uniform across the thickness of the ribbon. Typical oxide particles were 2 to 4 microns with some aggregation of particles.

Samples Y15-34 and Y15-38 were independently given the same treatment of Ox-13 followed by TG fast without the coil to 900°C with a 10 minute hold. These samples show no banding, having a uniform microstructure of random, elongated oxide phase particles typically 1 micron wide by up to 3 microns long as shown in Figure 3-25. Sample Y15-39 was given this treatment followed by an isothermal anneal.

Samples Y15-33 and Y15-35 were independently given the same treatment of Ox-13 followed by TG fast without the coil to 900°C with a 3 hour hold. Although given the same nominal treatment, the microstructures of these two samples are different. Y15-35 has very large oxide particles typically 5 to 10 microns by 10 to 30 microns and shows only minimal tendency toward banding having a thin (less than 2 microns) band of oxide at the surface. Y15-33 has some banding present that resembles the banding seen in Y15-8 (see Figure 3-23), although in sample Y15-33 the center band of Ag is less well delineated

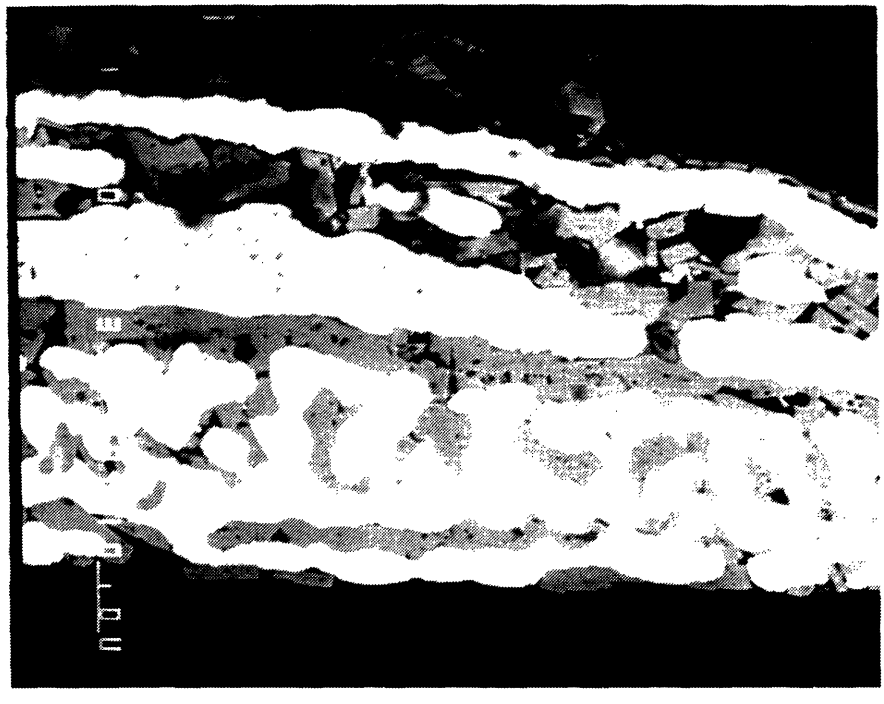

Figure 3-24. Backscatter electron image of sample Y15-53 (1000x).

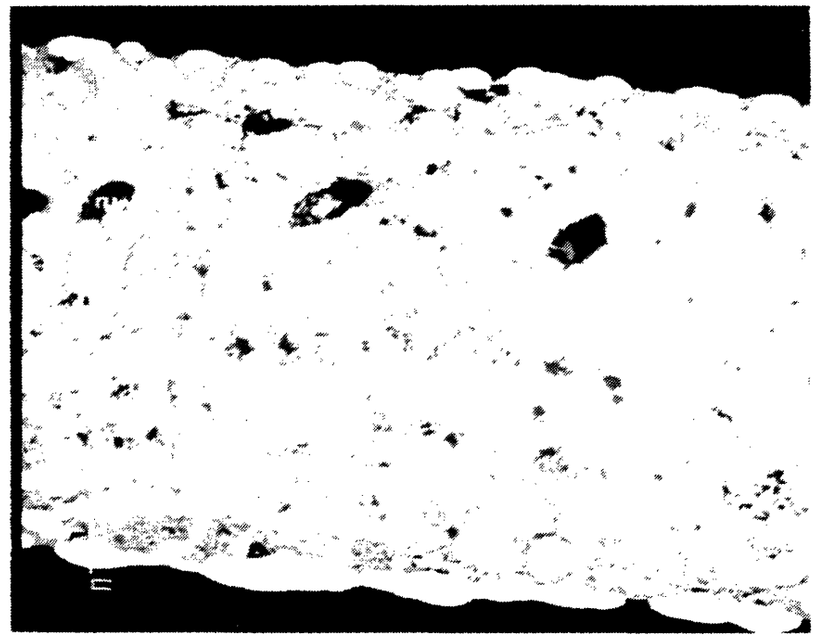

Figure 3-25. Backscatter electron image of sample Y15-38 (1000x).

and there are regions where the two Ag/oxide bands break down. In general, there is an upper Ag band 10 to 15 microns thick, then an Ag/oxide band 30 to 40 microns thick, a central Ag band 10 to 15 microns thick, another Ag/oxide band, this one only 10 to 20 microns thick, and a final Ag band 5 to 10 microns thick.

Sample Y15-51 was given the same treatment (Ox-13, TG fast without the coil, hold 3 hours) but the maximum temperature was 925°C. This sample has a variable microstructure with most of the sample having isolated oxide particles of up to 3 microns and no banding. There are a few areas of the sample which have some Ag and oxide bands present but these bands are not well defined or even consistent across the width of the sample.

Sample Y15-47, which had Ox-13, was given the treatment TG fast with the coil to 900°C and held for 10 minutes. This sample has well defined Ag bands at the center and at both surfaces. The Ag bands are approximately 4 to 5 microns thick. The remaining area consists of two Ag/oxide bands that have a high degree of oxide connectivity and nearly continuous oxide at the edge of the bands as shown in Figure 3-26. Sample Y15-48 was given the same treatment followed by an isothermal anneal (see Section 3.5). Sample Y15-49 was given the same treatment except that the maximum temperature was 925°C and the treatment was followed by a long isothermal anneal (see Section 3.5).

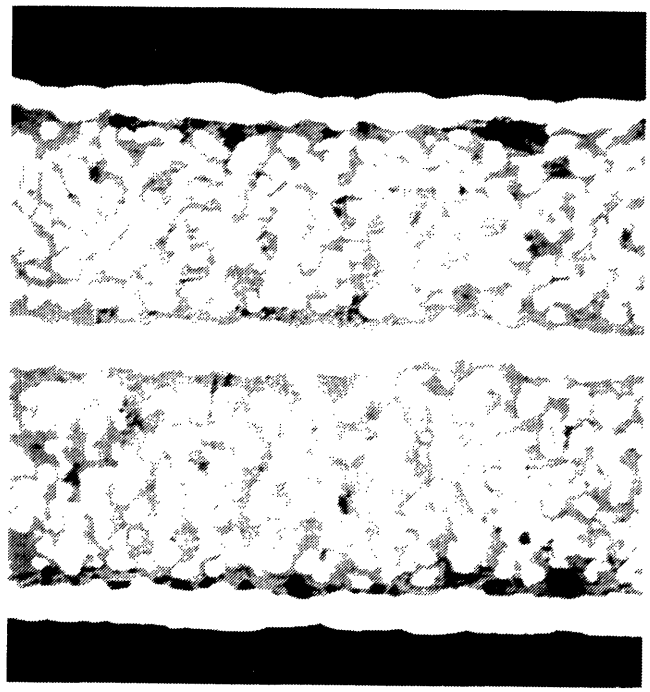

Figure 3-26. Backscatter electron image of sample Y15-47 (1000x).

Samples Y15-36 and Y15-42 were both given treatments of Ox-13, TG fast with the coil, and held for 3 hours at a maximum temperature of 900°C and 895°C, respectively. Sample Y15-36 has an Ag band at the center 12 microns thick and surface Ag bands 7 to 8 microns thick. The remaining area consists of Ag/oxide bands 15 to 25 microns thick in which the Ag forms irregular islands and the oxide is highly connected. Near the outer edges of the Ag/oxide bands the oxide phase is nearly continuous. However, near the inner edges of the Ag/oxide band, the oxide phase is neither continuous nor as straight as it is in Figure 3-26. Sample Y15-42, shown in Figure 3-27, has an unusual microstructure where there is a large amount of clustering of oxide phase but no typical banding behavior.

3.4.3 Temperature Gradient Processing at Very Slow Velocities

Samples Y15-68, Y15-70, and Y15-72 were given treatment Ox-13 and then processed in the temperature gradient furnace at very slow velocities to a maximum temperature of 900°C. The respective traveling velocities for the samples was 0.38 cm/hr, 0.13 cm/hr, and 0.26 cm/hr. The resulting maximum temperature ramp rates were 2.2°C/min, 0.72°C/min, and 1.3°C/min, respectively.

Figure 3-28 shows an SEM photo of sample Y15-70. Samples Y15-68 and Y15-72 had very similar microstructures. In all three samples the surface Ag bands were 10 to 20 microns thick with occasional areas where there was no Ag

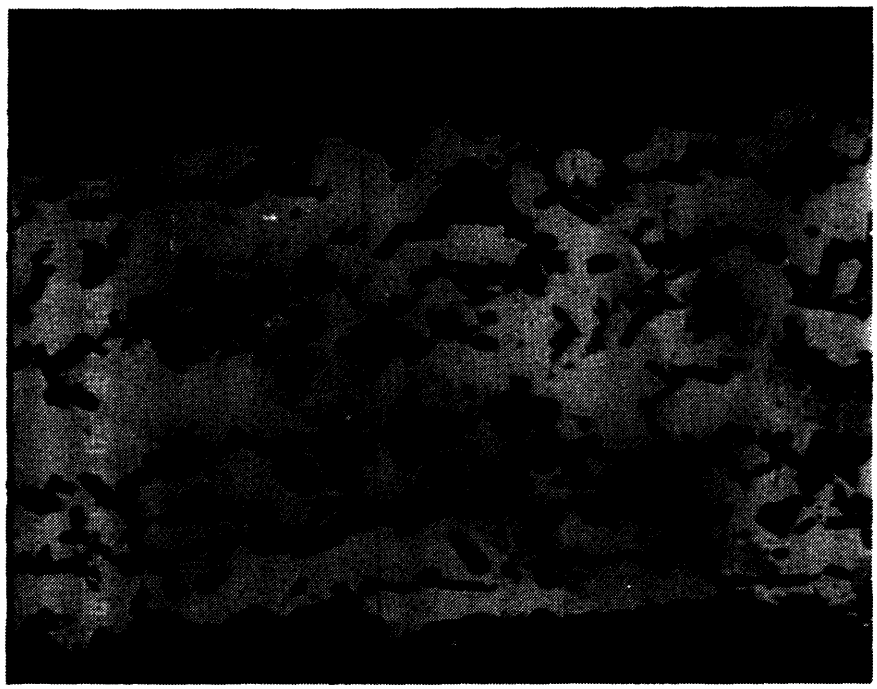

Figure 3-27. Backscatter electron image of sample Y15-42 (1000x).

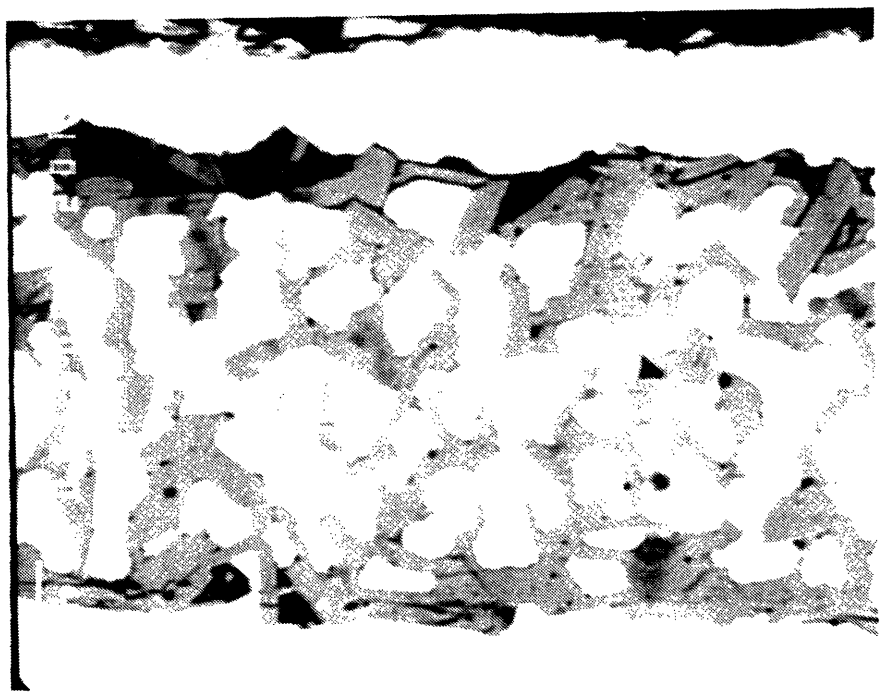

Figure 3-28. Backscatter electron image of sample Y15-70 (1000x).

band present at one of the surfaces. There was no center Ag band in any of these samples.

3.4.4 Summary of Temperature Gradient Processing Results

The results of the high temperature transformation treatments that were done in the temperature gradient furnace are shown schematically in Figure 3-29. In general, increasing the degree of oxidation, the hold time, and using the additional coil increased the tendency for forming Ag bands at the surface and center. The samples with the most delineated Ag bands had received complete oxidation and were treated in the temperature gradient furnace with the additional heating coil.

Section 3.5 Isothermal Anneal

Some samples were given an isothermal annealing stage in air. This stage was intended to determine what, if any, coarsening would occur during an isothermal anneal and to allow comparisons between isothermal anneals and longer hold times during the high temperature transformation stage. This process involved loading the sample directly into a furnace that was already at the desired temperature, holding for the specified time and removing the sample from the furnace. The standard anneal was 3 hours at 890°C.

Sample Y15-54 was given this standard anneal after receiving Ox-NH and TG fast to 885°C with the coil and a 10 minute hold (see Y15-53 in Figure 3-24

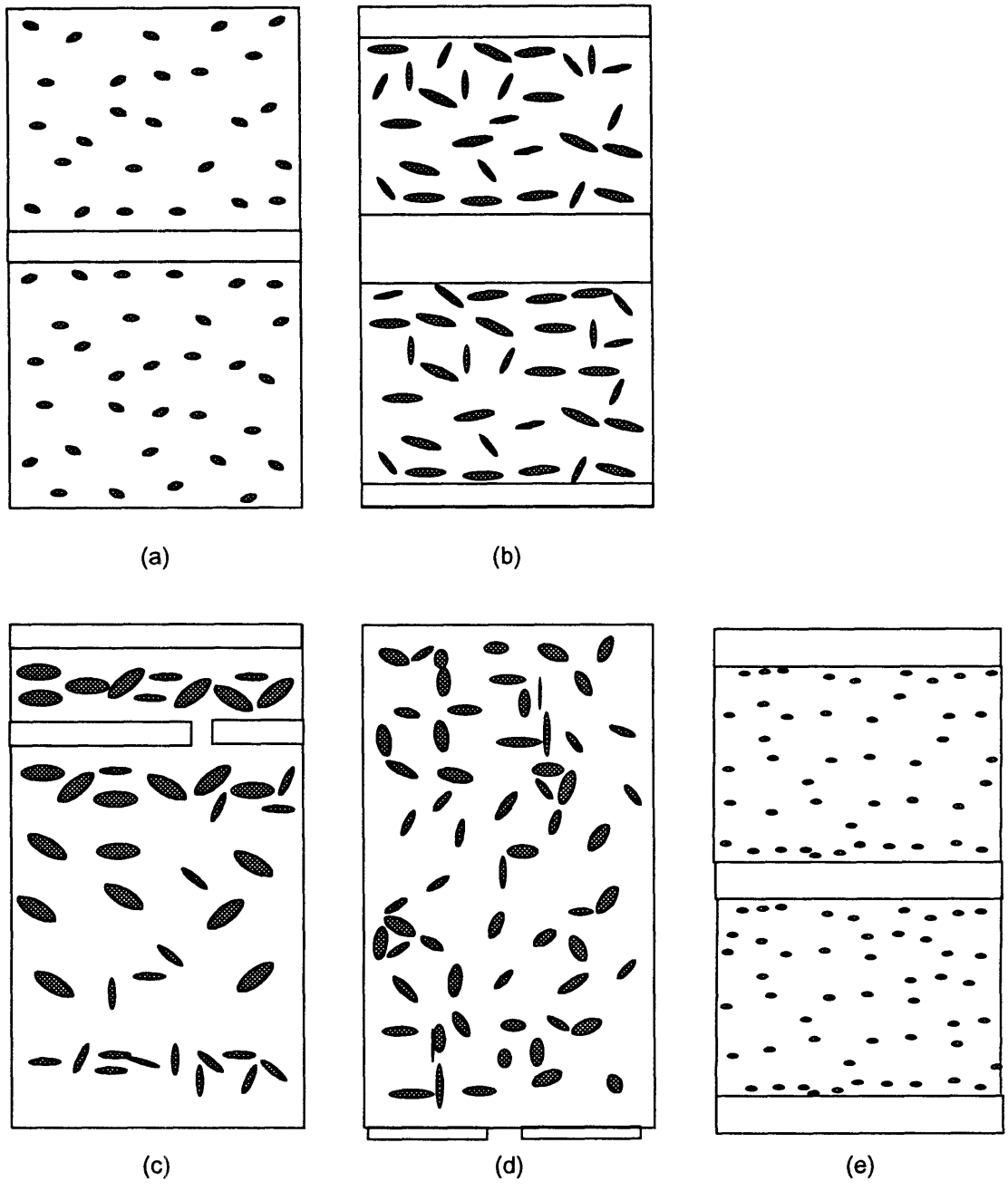

Figure 3-29. Schematic of results of high temperature transformation treatments in the temperature gradient furnace: (a) No-Ox and TG slow; (b) No-Ox and TG slow with hold; (c) Ox-NH and TG fast; (d) Ox-13 and TG fast; and (e) Ox-13 and TG fast with the coil. To see actual microstructures, refer to Figures 3-22 to 3-26.

for comparison). This sample had two continuous oxide bands typically 5 to 10 microns thick extending the length of the sample. The remaining area was Ag with occasional isolated oxide particles (typically less than 5 microns).

Sample Y15-39 was treated like Y15-34 and Y15-38 (Ox-13, TG fast without the coil to 900°C and held 10 minutes) followed by the standard isothermal anneal. This sample shows typical banding like that shown in sample Y15-8 in Figure 3-23 with surface Ag bands 7 to 8 microns thick, a central Ag band 10 to 15 microns thick, and Ag/oxide bands 15 to 30 microns thick.

Sample Y15-48, shown in Figure 3-30, was treated like Y15-47 (Ox-13, TG fast with the coil to 900°C and held for 10 minutes) followed by the standard isothermal anneal. This sample also shows the typical succession of bands. The center Ag band in this sample is 11 to 13 microns thick, two to three times as thick as in Y15-47. The oxide phase in the Ag/oxide bands has coarsened significantly so that the band now has the appearance of isolated Ag islands surrounded by oxide instead of an interconnected network of the two phases. The Ag/oxide bands are 16 to 22 microns thick and the Ag islands within this band are typically less than 5 microns wide by 10 microns long.

Sample Y15-49 was treated like Y15-48 with two changes; the maximum temperature was 925°C and the isothermal anneal at 890°C was for 30 hours instead of the standard 3 hours. The sample has Ag bands up to 20 microns wide. However, these bands are not consistently located at the surfaces and

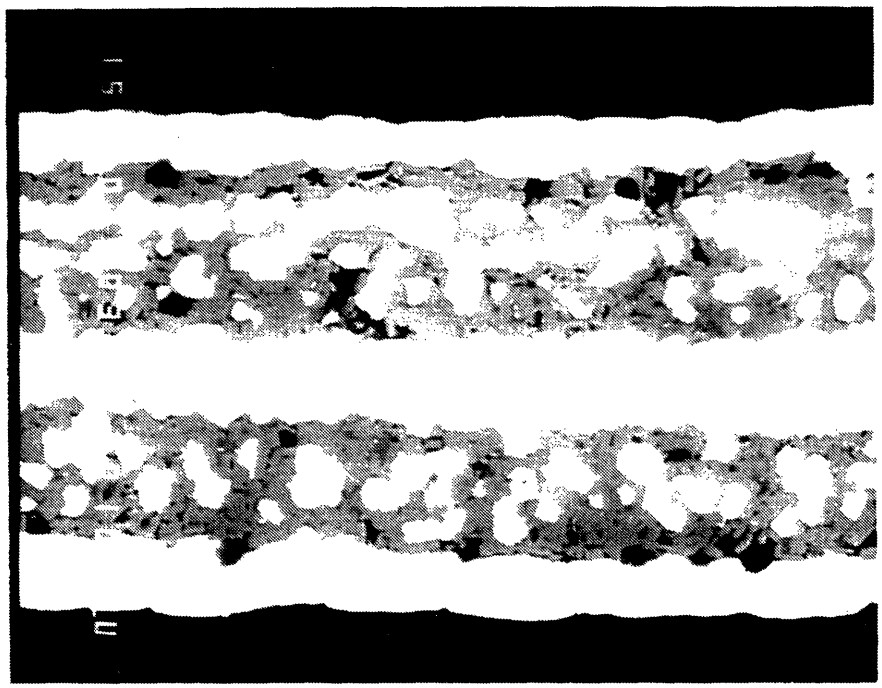

Figure 3-30. Backscatter electron image of sample Y15-48 (1000x).

center of the sample. In some areas the center band moves towards an edge and the Ag band at the edge disappears, leaving only two Ag bands. The Ag/oxide bands do not have continuous oxide phase at the edge of the bands as is frequently seen. The bands are also not of a consistent width.

Samples Y15-44, Y15-46, and Y15-59 received no high temperature transformation treatment. They received the standard isothermal anneal of 3 hours at 890°C after oxidation treatments of 10°C/min to 420°C in air, hold 14 1/4 hours; 10°C/min to 420°C in air, hold 17 1/3 hours and cool in the furnace; 5°C/min to 420°C in air, hold 4 hours, respectively. Sample Y15-44, shown in Figure 3-31, shows a minor amount of banding in the form of Ag bands located 2 to 10 microns from the surface and having a thickness of 5 to 15 microns. Sample Y15-46, shown in Figure 3-32, has oxide at the surface, frequently followed by Ag bands located 3 to 5 microns from the surface. The central region of this sample is unusual in that there are many areas in which the oxide phase appears to be aligned at an angle to the surface which ranges from a few degrees, as seen in Figure 3-32, to 45°. Sample Y15-59, shown in Figure 3-33, has bands of oxide that are 4 to 8 microns thick. In various regions of the sample the number of oxide bands ranges from 2 to 4. There are Ag bands between the oxide bands and a band of Ag/oxide near the surface.

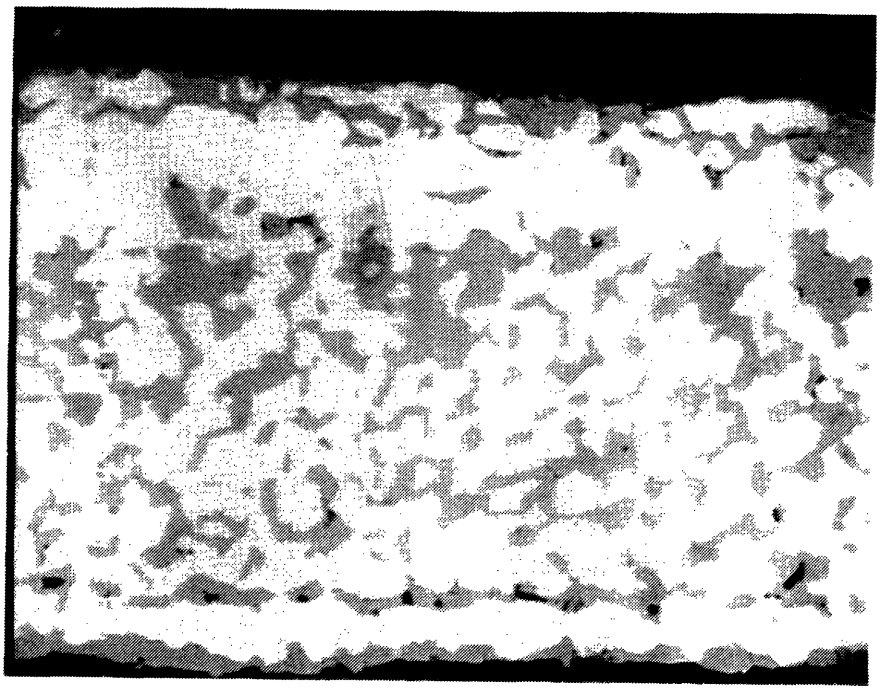

Figure 3-31. Backscatter electron image of sample Y15-44 (1000x).

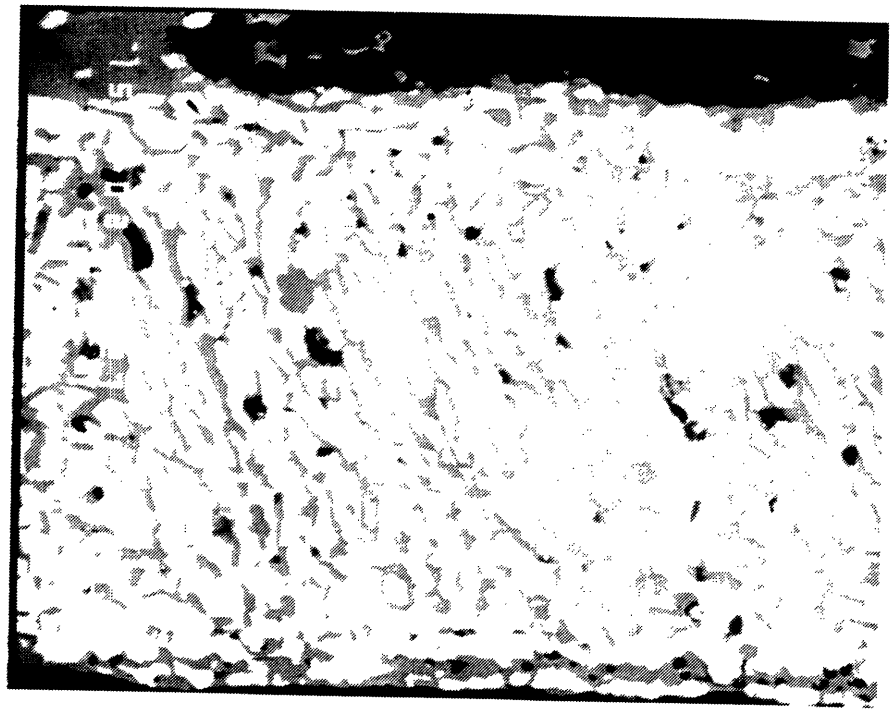

Figure 3-32. Backscatter electron image of sample Y15-46 (1000x).

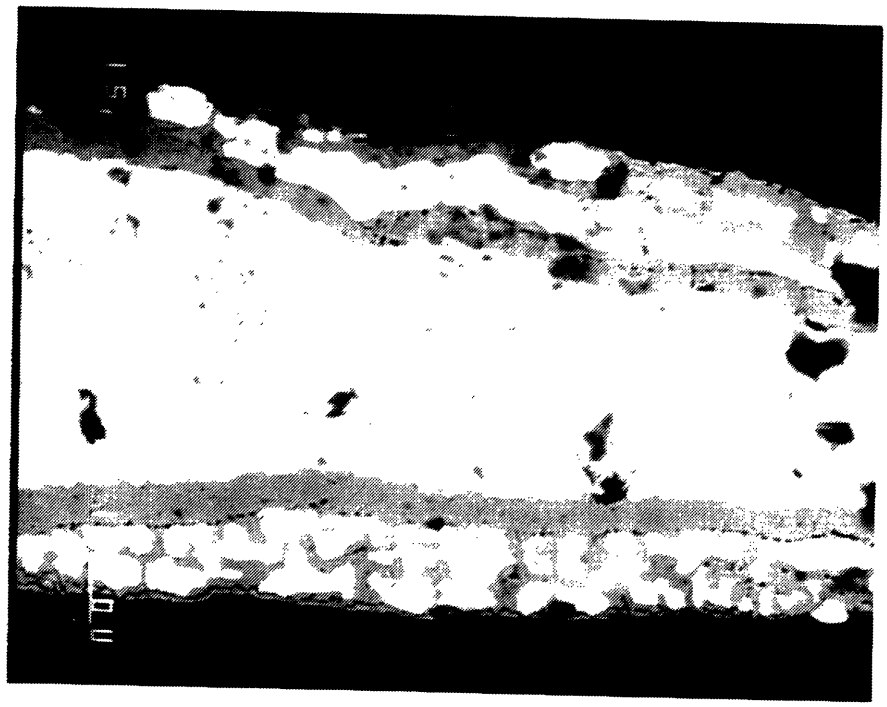

Figure 3-33. Backscatter electron image of sample Y15-59 (1000x).

3.5.1 Summary of Isothermal Anneal Results

An isothermal anneal results in coarsening of both the oxide particles and the Ag bands. Thus, the oxide particles are larger in a sample which received an isothermal anneal than in a sample which was treated similarly but without the isothermal anneal. In the cases where the sample treated without the isothermal anneal contained Ag bands at the surface or center, the thickness of these bands increased during the isothermal anneal. This is illustrated schematically in Figure 3-34.

Section 3.6 Oxygenation

Several samples were tested in a SQUID at 10 K and 30 G and all were found to be non-superconducting after the high temperature transformation treatments. Thus, an oxygenation treatment was done in order to increase the oxygen content of the $Y_1Ba_2Cu_3O_{7-x}$ phase (decrease x). After oxygenation, all of the Y15 samples tested were superconducting. For more information on the superconducting properties of the samples see the following section.

The standard oxygenation treatment was an isothermal hold at 500°C for 20 hours in flowing oxygen (see Section 2.2.2 for details of the experimental procedure). Samples Y15-38 and Y15-30 were given a different oxygenation treatment. These samples were loaded into a furnace at 600°C and held for 12 hours, cooled 0.5°C/min to 450°C, and held there for 24 hours in flowing oxygen. These samples were also found to be superconducting (see Section 3.7 for more

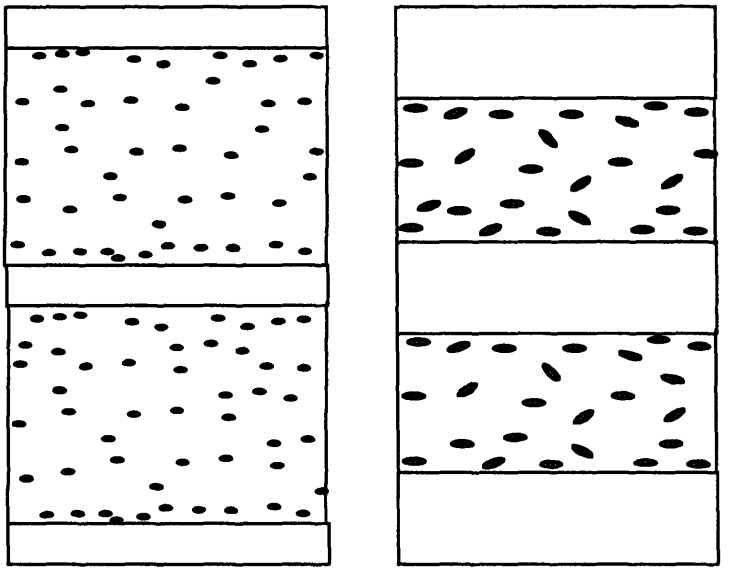

Figure 3-34. Schematic illustration of effect of isothermal anneal: (a) before isothermal anneal and (b) after isothermal anneal. To see actual microstructures, refer to Figures 3-26 and 3-30.

information on the superconducting properties of the various samples). Samples Y15-21 and Y15-53 were given additional oxygenation holds for 120 hours at 500°C in flowing oxygen.

Section 3.7 Superconducting Properties

3.7.1 SQUID Measurements of Critical Transition Temperature

SQUID measurements of the critical temperature (T_c) for transition from superconducting to normal material in a magnetic field of 30 G were performed on a few samples to confirm that the materials were behaving in an expected manner. A typical plot is shown in Figure 3-35. This plot is for sample Y15-42 and shows an onset temperature of 88 K. Onset temperatures were found from 86 K to 90 K for various samples. The resistance equals zero temperature can not be determined from this data.

3.7.2 Four Point Probe Measurement of Critical Current Density

Critical current density (J_c) measurements were made on samples Y15-36, Y15-47, Y15-48, Y15-53, and Y15-54 using a four point probe setup. The samples were immersed in liquid nitrogen (77 K) when the measurements were made. The ribbons that were tested were found to be unable to support a supercurrent at this temperature.

Samples Y15-21 and Y15-53 were given an additional oxygenation hold of 120 hours at 500°C and then tested. These samples were also found to be

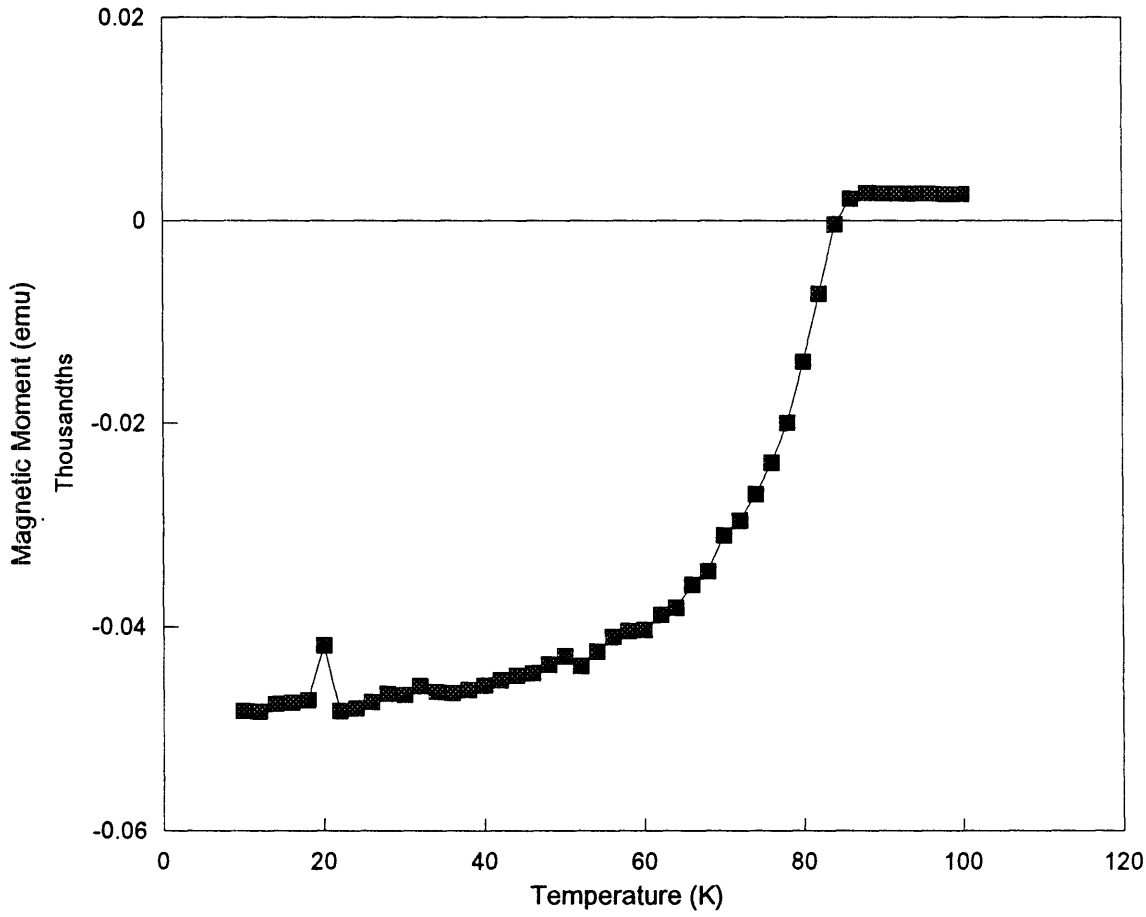

Figure 3-35. T_c plot for sample Y15-42 showing onset of superconductivity at 88 K.

non-superconducting at 77 K. Critical current density measurements were made on these samples and on sample Y15-48 immersed in liquid helium (4.2 K). All of the samples were found to be unable to support a supercurrent.

Section 3.8 $Yb_1Ba_2Cu_3Ag_{16}$ Samples

The initial ribbon referred to as Yb16 had a nominal composition of $Yb_1Ba_2Cu_3Ag_{16}$ and a composition determined by microprobe analysis of $Yb_{0.78}Ba_{1.78}Cu_3Ag_{15.57}$.

Sample Yb16-2, which had no prior oxidation, was given a high temperature transformation treatment of 10°C/min to 900°C (in Furnace R) and removed immediately. This sample has a uniform microstructure consisting of very fine oxide phase particles approximately 1/2 micron by 1 to 4 microns throughout the interconnected Ag phase. Microprobe analysis shows the average composition of the oxide phase to be $Yb_{1.20}Ba_{2.05}Cu_3O_{6.35}$-$Ag_{0.43}$. It is reasonable to assume that the Ag present in this analysis is actually from the Ag phase surrounding the oxide phase and not a component of the oxide phase. This occurs because the size of the particles (often only 1/2 micron thick) is less than the minimum affected area of the sample during the microprobe analysis (close to 1 micron).

Samples Yb16-3 and Yb16-4 were given treatment Ox-13 followed by TG fast with the coil to 870°C, held for 10 minutes and cooled in the furnace. Sample Yb16-4 was then given an isothermal anneal at 850°C for 3 hours. Sample

Yb16-3 has an Ag band 4 to 8 microns wide in the center of the ribbon and Ag up to 8 microns thick at the surface as shown in Figure 3-36. Sample Yb16-4, shown in Figure 3-37, shows no banding with a uniform distribution of elongated oxide phase particles, typically less than 1 micron by up to 3 microns, in the predominant Ag phase.

After receiving the standard oxygenation treatment, these samples were found to be superconducting. The critical transition temperature was measured for sample Yb16-4 and found to be 88 K.

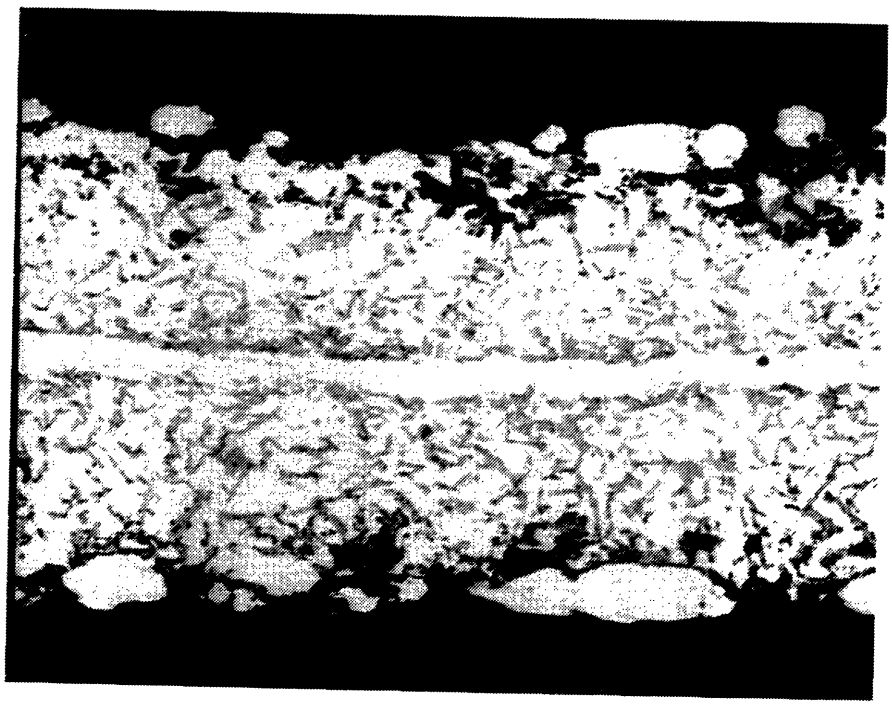

Figure 3-36. Backscatter electron image of sample Yb16-3 (1000x).

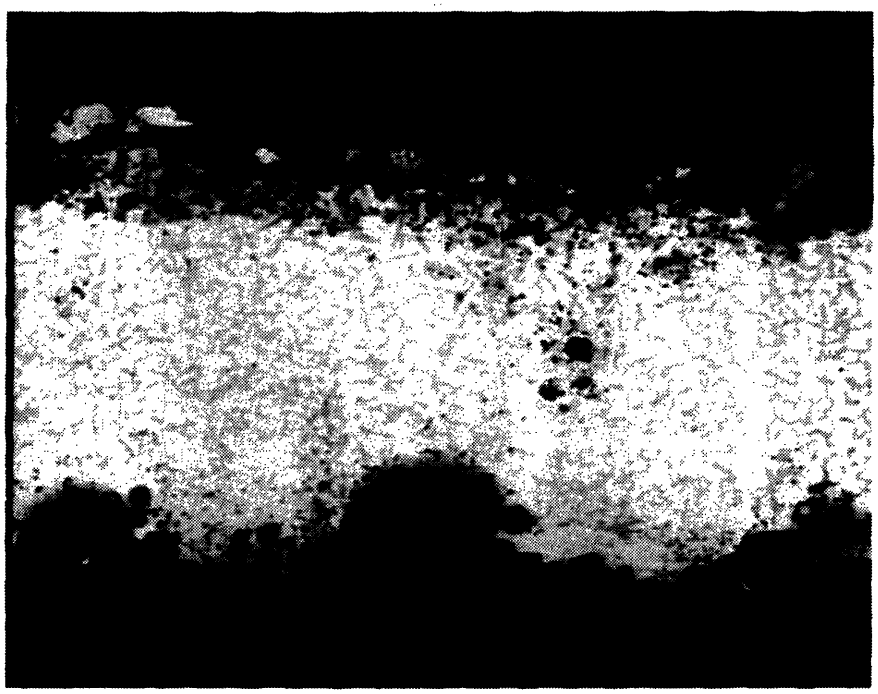

Figure 3-37. Backscatter electron image of sample Yb16-4 (1000x).

Chapter 4. Discussion

The discussion in this chapter is divided into sections according to the processing stage. Discussion related to the low temperature oxidation stage is in Section 4.1. Discussion related to the high temperature transformation stage is in Section 4.2. Discussion of the experimental results seen when the high temperature transformation stage uses solid state thermal gradient processing is in Section 4.3. Section 4.4 contains a theoretical analysis of solid state thermal gradient processing and a comparison of the theoretical and experimental results. A discussion of the superconducting properties of the materials is in Section 4.5. Section 4.6 contains a discussion of the relationship of the results seen for Yb16 samples to the Y15 samples. Section 4.7 contains suggestions for future work and a discussion of the applicability of the findings of this work to other materials systems.

Section 4.1 Low Temperature Oxidation Treatments

The low temperature oxidation treatments were designed to result in the formation of the elemental oxides Y_2O_3 or Yb_2O_3, BaO, and CuO, with formation of $BaCuO_{2.5}$ and $BaCuO_3$ also possible.

4.1.1 Internal Oxidation

There is no evidence of an external oxide scale being formed on the surface of the oxidized ribbons. Instead, there is a distribution of small oxide particles

throughout an unoxidized Ag phase. This indicates that internal oxidation occurred as expected from the criteria suggested by Wagner [29] and Combe and Cabane [33] (see Section 1.2.1 for more information).

An attempt was made and presented in Section 1.2.2 to predict the location of the oxidation front for the various low temperature oxidation treatments using the equation

$$\xi = 2\gamma(D_o t)^{\frac{1}{2}} \tag{4-1}$$

with

$$\gamma = \left[\frac{C_o^0}{2\nu C_B^0}\right]^{\frac{1}{2}} \tag{4-2}$$

where ξ is the thickness of the oxidation zone (cm), D_o is the diffusivity of oxygen in silver, C_o^0 is the solubility of oxygen in silver, C_B^0 is the concentration of the solute (Y, Ba, and Cu), ν is the ratio of oxygen to metal in the oxide, and t is the time (s). Various data for the diffusivity and solubility of O in Ag was found (see Section 1.2.2). The predicted location of the oxidation front using different combinations of the data are summarized in Table 4.1.

The best agreement between the predicted values and the experimentally determined values was found using the solubility value of 1.3×10^{-5} atomic fraction at 420°C from Sandhage [27] and the diffusivity approximation of 1.2×10^{-6} cm^2/s at 420°C from Kontoulis and Steele [34]. The results from this

Table 4.1. Predicted thickness of the oxidation zone using various combinations of the available solubility and diffusivity data.

Ramp Rate:		0.5°C/min (in flowing oxygen)				5°C/min (in air)		10°C/min (in air)		
Hold time:		ramp only	4 hr	8 hr	13 hr	ramp only	4 hr	ramp only	14 hr	17 hr
Solubility Source	Diffusivity Source	Thickness (microns)								
Podgurski & Davis [36]	Kontoulis & Steele [34]	1.76	3.12	4.04	4.96	0.38	1.78	0.27	3.26	3.6
Eichenauer & Muller[37]	Kontoulis & Steele [34]	1.29	2.31	3.01	3.7	0.28	1.33	0.19	2.44	2.69
Sandhage [27]	Kontoulis & Steele [34]	7.62	13.9	18.1	22.2	1.63	8.01	1.15	14.7	16.2
Podgurski & Davis [36]	Gryaznov et al. [38]	45.7	68.8	85.9	103	9.79	36.1	6.92	65.5	72.1
Eichenauer & Muller[37]	Gryaznov et al. [38]	32.6	50.4	63.4	76.6	6.98	27	4.94	49	53.9
Sandhage [27]	Gryaznov et al. [38]	189	300	379	459	40.6	16.2	28.7	29.5	32.5
Podgurski & Davis [36]	Sandhage [27]	1.75	3.1	4.02	4.93	0.38	1.77	0.27	3.25	3.58
Eichenauer & Muller[37]	Sandhage [27]	1.28	2.3	2.99	3.68	0.27	1.32	0.19	2.43	2.68
Sandhage [27]	Sandhage [27]	7.58	13.8	18	22.1	1.62	7.97	1.15	14.6	16.1

prediction are restated in Table 4.2. The values that were found experimentally are also summarized in this table.

There was very good agreement between the predicted results and the experimental results for all of the samples which were oxidized in flowing oxygen. The largest difference was seen in sample Y15-36a which received treatment Ox-13 (5°C/min to 140°C, 0.5°C/min to 420°C and hold 13 hours).

Table 4.2. Predicted and experimentally determined values for the oxidation zone thickness (microns).

Ramp rate:	0.5°C/min				5°C/min		10°C/min		
Atmosphere:	Flowing oxygen				Air		Air		
Hold time:	None	4 hours	8 hours	13 hours	None	4 hours	None	14 hrs	17 hrs
Predicted Thickness (microns)	7.62	13.9	18.1	22.2	1.63	8.01	1.15	14.7	16.2
Experimentally determined thickness (microns)	6.5	14	21	Comp.[a]	N/A	10.5	N/A	Comp.[a]	Comp.[a]
% difference	-15	1	16	(23)[b]		31		(87)[b]	(70)[b]
Sample #	Y15-2	Y15-66	Y15-64	Y15-36a		Y15-59a		Y15-43	Y15-45

a. Oxidation proceeded to completion with oxygen found evenly throughout the entire sample.
b. Values in parentheses are based on the oxidation front having just reached the center of the ribbon at the end of the hold time.

There was no oxidation front visible in this sample. Microprobe analysis showed a uniform oxygen content throughout the sample indicating that the oxidation was complete. Thus, the oxidation front must have traveled 27 microns to reach the center of the ribbon. This is 23% larger than the predicted results for this hold time.

It is interesting to note that the percentage difference between the predicted results and the experimental results increased as the hold time increased. This indicates that there was a diffusion path available for the oxygen that was faster than expected for diffusion through the Ag phase. This path could be along grain boundaries, along the newly formed Ag/oxide phase boundaries, or through flaws in the ribbon such as cracks and voids. This is supported by the presence of areas in some of the samples in which the oxidation front is not

parallel to the surface. Figure 4-1 shows an example of an area where the oxygen front bulges inward in an area in which flaws are visible.

Otto [67] determined the oxidation rate for similar samples based on weight gain. The samples that Otto used were from the same starting material as that used in these experiments. However, for the current experiments, the samples were stored for approximately three additional years. Otto's results indicate a higher diffusion rate than was observed in these experiments. This indicates that aging resulted in a reduction in the inward diffusion rate of oxygen. This may be due to the formation of a thin oxide surface layer while in storage at room temperature. Even a thin oxide that covers the surface should result in a slower observed rate of travel for the oxidation front because oxygen diffusion is likely to be slower through the oxide than through Ag. Diffusion rates for Cu through Ag [32,68] are three to four orders of magnitude larger than diffusion rates for Cu in Y-Ba-Cu-O thin films [69].

For the experiments done in air, fewer experimental results are available, but good agreement is again seen between the predicted location of the oxidation front and the experimental results. The 4 hour hold sample for the 5°C/min ramp rate (sample Y15-59a) was within 31% of the predicted value. In the samples for the 10°C/min ramp, the oxidation front was not clearly visible in the SEM and was not located using microprobe analysis. It is probable that the oxidation was complete in these samples; differences of 87% and 70% from the predicted

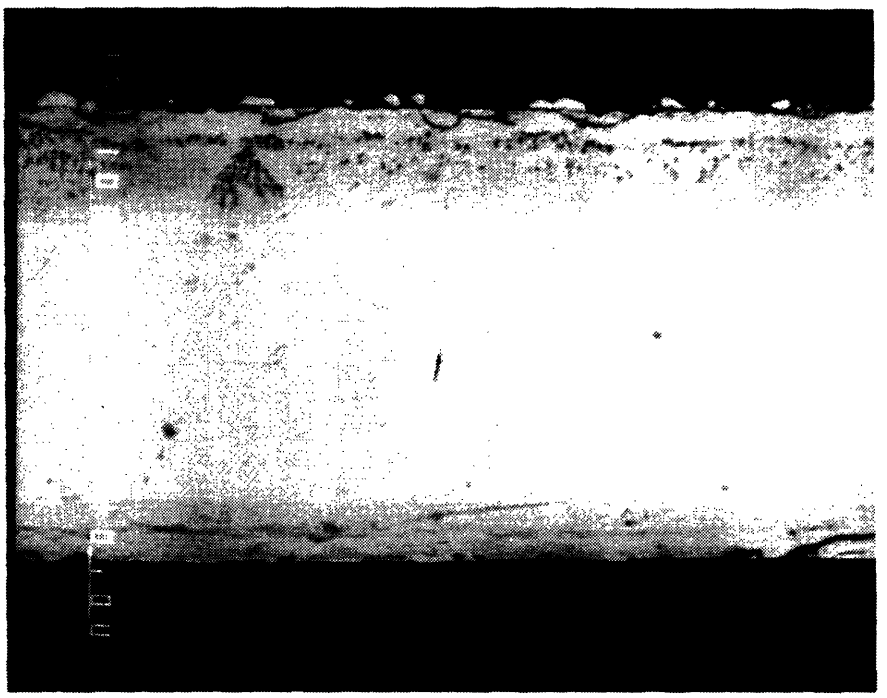

Figure 4-1. Microstructure showing rapid oxygen front ingression in region containing flaws.

oxidation zone thickness would have been necessary to result in complete oxidation. This is very possible given the long hold times if one assumes that there is a fast diffusion path available for the oxygen.

In the samples discussed so far, elemental dotmaps showed reasonably uniform distributions of each element throughout the ribbon, except for sample Y15-36a (Ox-13). In this sample, there is a very narrow (less than 1 micron wide) band at the center that is almost pure silver. There is a wider area (approximately 6 microns wide) that is Cu depleted. On each side of the Ag band, there is a row of features (3 to 4 micron diameter) that are very rich in Ba and Cu (see Figure 3-6). During the oxidation process, there is slow outward diffusion of the solutes as well as rapid inward diffusion of oxygen. During oxidation, the solutes are most concentrated ahead of the oxidation front; at the center of the sample, the solute concentration is decreasing. Thus, when the oxidation front nears the center of the sample, there is a region of high solute concentration which results in the Ba and Cu rich features. This is followed by an area that is nearly solute free. This area is the Ag band found at the center of the sample. Otto [67] noted that the thickness of this Ag band increased as the heating rate of the sample increased.

The other area of non-uniformity in these samples occurs at the surface where silver nodules form. The silver nodules cover an increasingly larger area of the surface as the oxidation process progresses. The formation of

noble-metal-rich nodules on the surface during internal oxidation is due to the relief of stress, associated with the volume change at the internal oxidation front. The stress is relieved by the migration of silver along dislocation pipes [27,39,40]. The volume of Ag nodules formed at the surface of sample Y15-36a is approximately 5% of the original sample. This is equivalent to a thickness of 1.4 microns if the Ag was spread over the surface uniformly. This is reasonable since the total volume change during oxidation is a few percent.

Considering both areas of non-uniformity, there is a solute free band of Ag formed at the center of the ribbon due to outward solute diffusion and there are Ag nodules that form at the surface due to stress relief which become Ag surface bands during the high temperature transformation treatment. Thus, an initially homogeneous material is processed through a known heat cycle and results in a five layer microstructure (for example, see Figure 3-26). Ag layers are located at both surfaces and the center while the intermediate two-phase layers consist of Ag and oxide. This ability to process a homogeneous material to produce a layered microstructure has potential applications in other materials systems. A discussion of the applicability of these findings to other materials systems and suggestions for future work are provided in Section 4.7.

In samples Y15-22 through Y15-27, some regions of enrichment or depletion of particular elements were seen. The enrichment of Y in the region near the surface of sample Y15-22 may be due to the fact that Y is the most reactive of

the metals present with respect to oxidation at 400°C. In samples which received one or more additional hold times, the Y has diffused so that it is once again distributed evenly throughout the sample.

While samples Y15-22 and sample Y15-28 were being removed from the furnace, all of the remaining samples (Y15-23 to Y15-27 and Y15-29 to Y15-31) were exposed to a decrease in temperature (estimated to be around 200°C) and decrease in oxygen partial pressure (to air, 0.21 atm O_2). This resulted in a temporary decrease in the velocity of the oxidation front followed by an increase when the samples are returned to the furnace. This resulted in the narrow region of Cu enrichment in sample Y15-24 which is located at the same distance from the surface as the boundary between the two regions in sample Y15-22. There is no region like this in samples Y15-64 and Y15-66 which did not see a decrease in temperature and oxygen partial pressure part way through the hold. This explanation is supported by the work done by Sandhage [27] in which cyclic temperature and oxygen partial pressure were used to produce microlaminates with alternating layers of Ag and oxide or a two-phase Ag/oxide.

4.1.2 Effect of Oxidation Stage on Otherwise Identical Samples

The effect of the low temperature oxidation stage on the final superconducting ribbons may be seen by comparing samples Y15-9 and Y15-15 which received the same high temperature transformation treatment (see Table 4.3). These samples had treatments No-Ox and Ox-NH, respectively, and both

were heated 10°C/min to 900°C in air and removed immediately. Sample Y15-9 has a uniform microstructure throughout the ribbon while sample Y15-15 has a two region microstructure with the central region being coarser than the outer region. Thus, the partial oxidation (Ox-NH) is conducive to a two region microstructure (oxidized and unoxidized). A two-region microstructure remains after high temperature processing at short times, although the boundary between the regions does begin to move toward the center of the ribbon. With longer hold times, significant coarsening has occurred and the difference due to the oxidation treatment is no longer present. For example, the difference is no longer present in the coarsened microstructures of samples Y15-4 and Y15-16 (treated like Y15-9 and Y15-15, respectively, but with a 3 hour hold at 900°C).

Table 4.3. Comparison of samples showing effect of oxidation stage.

Sample	Oxidation Treatment	High Temp Treatment & Anneal	Observed Results
Y15-9	No-Ox	10°C/min to 900°C, no hold	Uniform microstructure
Y15-15	Ox-NH		Two region microstructure
Y15-21	Ox-NH	TG fast with coil to 900°C, hold 3 hours	Oxide particles 2 - 4 microns
Y15-36	Ox-13		Clear Ag and Ag/oxide bands
Y15-53	Ox-NH	TG fast with coil to 900°C, hold 10 min	Isolated oxide particles 2 - 6 microns / some banding
Y15-47	Ox-13		Clear Ag and Ag/oxide bands
Y15-54	Ox-NH	TG fast with coil to 900°C, hold 10 min, Anneal 3 hours at 890°C	Oxide and Ag/oxide bands
Y15-48	Ox-13		Clear Ag and Ag/oxide bands

The effect of the low temperature oxidation treatment on samples which received high temperature treatments in the temperature gradient furnace may be seen by comparing sample Y15-21 to sample Y15-36 (TG fast w/ coil to 900°C, hold 3 hrs), sample Y15-53 to sample Y15-47 (TG fast w/ coil to 900°C, hold 10 min), and sample Y15-54 to sample Y15-48 (TG fast w/ coil to 900°C, hold 10 min, then anneal 3 hrs at 890°C). In each of the pairs, the first sample received treatment Ox-NH and the second sample received treatment Ox-13. The second sample in each case had clearly defined bands of Ag at both surfaces and in the center, with two-phase Ag/oxide regions in between. The first sample in each case had less clearly defined bands or no bands present.

The silver band at the center may be explained by referring to sample Y15-36a (Ox-13) where the solute-depleted central area was explained by slow outward solute diffusion and complete oxidation. It is reasonable that when the high temperature transformation occurs, the small amount of solute remaining in the central region diffuses outward to an area where more elemental oxide exists to make the transformation to superconducting oxide easier. An Ag region remains at the center which will thicken with increasing hold time. This thickening is discussed further in Section 4.2.4.

The silver bands at the surface are a result of the silver nodules formed at the surface during the oxidation process. During the high temperature transformation treatments, the silver nodules coalesce to form a continuous or

nearly continuous layer of Ag on the surface. These Ag layers are non-existent in samples which were not oxidized, and the layers are of increasing thickness for samples in which the oxidation was more complete. These Ag layers also thicken with increasing hold time due to coarsening; this will be discussed in Section 4.2.4.

Section 4.2 High Temperature Transformation Treatments

The high temperature transformation treatments were intended to result in the transformation of the elemental oxides to $Y_1Ba_2Cu_3O_{7-x}$. Microprobe analysis of the composition shows that the proper oxide phase was formed along with the Ag phase. In some cases, there is also barium cuprate present after the transformation.

4.2.1 Effect of Maximum Temperature

All of the samples that were treated at 850°C or below (samples Y15-13, Y15-14, and Y15-28 to Y15-31) were found to have microstructures that consist of a uniform distribution of oxide particles surrounded by Ag (see Table 4.4). The largest typical dimensions found in any of these samples was only 1 micron by 3 microns for elongated particles (sample Y15-14). The only indication of banding found in any of these samples is a very narrow (1 micron) band of Ag found at one surface of sample Y15-31. This sample had the longest oxidation hold time of the samples treated at 850°C, but the hold was not continuous. No samples which received the oxidation treatment Ox-13 were treated at this

temperature, nor were any of the samples treated in the temperature gradient furnace.

Table 4.4. Comparison of samples showing effect of maximum temperature.

Samples	Maximum Temperature	Observed Results	Explanation
Y15-13, Y15-14, and Y15-28 to Y15-31	850°C	Uniform distribution of oxide particles (up to 1 - 3 microns) in Ag	Temperature low enough that slow diffusion prevents rapid coarsening
Most samples	890°C - 900°C	Maximum effects due to type of treatment and hold time	Ideal range for experimentation
Y15-49 and Y15-51	925°C	Ag/oxide phase boundaries not smooth, unusual banding	Temperature high enough that partial melting may occur

The results found for samples treated at 850°C may be explained by considering the effect of temperature on the coarsening rate. At 850°C, either the driving force for coarsening (the free energy of the Ag/oxide interface) is not sufficient to drive the process rapidly, or the coarsening rate is limited by the rate at which solute atoms cross the Ag/oxide interface. The lack of any significant banding may be due to the combined effects of the oxidation treatments, which did not include any samples with long continuous holds, and the low rate of coarsening of any very narrow Ag bands which exist at the surface.

The ideal temperature range for experiments was found to be 890°C to 900°C. In this temperature range, the hold time and the type of transformation

treatment had the maximum effects on the microstructure. These effects will be discussed in Sections 4.2.2 to 4.2.4.

Two samples were treated with the maximum temperature of 925°C. In both samples (Y15-49 and Y15-51), the oxide phase had an unusual appearance. The Ag/oxide phase boundaries were not as smooth as in other samples. Also, the banding that would be expected for a sample which had oxidation treatment Ox-13 and high temperature treatment TG fast with the coil was not seen. Sample Y15-49 contained some Ag banding, but these bands were not consistently located either at the center or surface. It is very likely that partial melting occurs at temperatures above 900°C. This partial melting would explain the different appearance of the Ag/oxide phase boundaries and may explain how the Ag bands are able to be located away from the surfaces and center of the sample.

4.2.2 Effect of Hold Time

Microstructures of small isolated oxide particles in Ag, similar to the microstructures found in the samples treated at 850°C, are found for samples given short hold times and treated without the temperature gradient (samples Y15-15 and Y15-9) or given treatment TG fast (samples Y15-34 and Y15-38) (see Table 4.5). In these samples, the short hold time prevents significant coarsening from occurring just as the lower temperature prevented significant coarsening for the 850°C samples.

Table 4.5. Comparison of samples showing effect of hold time.

Samples	Hold Time	Ramp rate	Observed Results	Explanation
Y15-9 and Y15-15	No Hold	10°C/min	Small Oxide Particles (< 3 microns) in Ag	Short hold time prevents significant coarsening
Y15-34 and Y15-38	10 min	TG fast		
Y15-11	No Hold	TG slow	Significant Coarsening	Slow heating rate exposes sample to high temperatures for longer time
Y15-47 and Y15-53	10 min	TG fast with coil	Moderate coarsening (5 micron oxide particles)	Additional heating coil has an effect (see Section 4.3.2)
Y15-4, Y15-6, Y15-8, Y15-16, Y15-21, Y15-54, Y15-33, Y15-36, Y15-39, Y15-42, and Y15-48	3 hour hold or short hold and 3 hour anneal	various	Significant Coarsening	Temperature and Time are sufficient to allow coarsening to occur

However, in sample Y15-11, which had no hold but was given the high temperature treatment TG slow, the microstructure has the appearance of a sample with a much longer hold time. This is due to the slow heating rate that results from the slow rate of travel through the temperature gradient furnace. The sample was not held at the maximum temperature, but it was exposed to temperatures near the maximum temperature during the heating process for sufficient time for significant coarsening to occur. The thermocouple located above the sample (refer to section 2.2.3 for furnace details) measured temperatures greater than 850°C for 1 hour 14 minutes and a temperature of 900°C for 44 minutes. The thermocouple located below the sample measured

temperatures greater than 850°C for 24 minutes. Most of the sample was exposed to temperatures above 850°C for 40 to 60 minutes, allowing coarsening to occur.

The short hold time effect on the microstructure is reduced in samples which were given the high temperature treatment TG fast with the coil. Sample Y15-53 contains some regions with Ag banding near the surface and at the center. Some regions have no banding and the oxide phase has coarsened to a typical particle size of at least 5 microns. Sample Y15-47 has well developed Ag bands 5 microns thick at both surfaces and 6 microns thick at the center. The oxide phase in the two-phase regions shows some signs of coarsening and coalescence. The effect of the temperature gradient furnace and the additional heating coil will be discussed in Section 4.3.

For samples with hold times of 3 hours at 900°C or a short hold time followed by a 3 hour anneal at 890°C, significant coarsening and coalescence occur. This occurs because the temperature is high enough for an adequate driving force for coarsening to exist, and the time at temperature is adequate to allow diffusion to occur rapidly.

Among the samples with hold times of 3 hours or a short hold time followed be a 3 hour anneal, the samples treated to a high temperature transformation without the temperature gradient show the least tendency for banding. However, none of these samples received oxidation treatment Ox-13. The samples which

received treatment TG fast were all given the oxidation treatment Ox-13 and show a moderate tendency for banding. The samples which were given the oxidation treatment Ox-NH and the high temperature transformation treatment TG fast with the coil also show a moderate tendency for banding. The samples which were given the oxidation treatment Ox-13 and the high temperature transformation treatment TG fast with the coil show a strong tendency for banding. The tendency for the degree of banding to increase as the degree of oxidation increases was explained in Section 4.1. The formation of Ag nodules which become the surface Ag bands were due to relief of the stresses resulting from the volume change. The presence of a narrow solute free region at the center of a sample that proceeded to complete oxidation was due to outward solute diffusion. This becomes the center Ag band. There was a tendency for the degree of banding to increase when the additional heating coil was used. This will be discussed in Section 4.3.2.

4.2.3 Explanation of Oxide Phase Coarsening

The traditional theory for coarsening in a two-phase system is the Ostwald ripening theory. The work of Lifshitz and Slyozov [70] advances the Ostwald theory. This and some more recent developments in coarsening theory development are summarized in Voorhees [71]. The fundamental equation for diffusion controlled coarsening in a two-phase system is

$$r^3 = r_0^3 + kt \qquad (4\text{-}3)$$

where

$$k = \frac{8\gamma C_e D\Omega^2}{9RT} \qquad (4\text{-}4)$$

and r is the average radius of the particles, γ is the free energy of the particle/matrix interface, C_e is the solute concentration in equilibrium with a particle of infinite size, D is the diffusion coefficient of the solute in the matrix, Ω is the molar volume of the precipitate, R is the gas constant, T is absolute temperature, and t is time.

Using values on the order of γ = 100 erg/cm^2 = 10^{-5} J/cm^2, C_e = 0.1, D = 10^{-10} cm^2/s, Ω = 100 cm^3/mole, R = 8.3 J/mole K, and T = 1200 K , gives a value for k of 10^{-16} cm^3/s. However, the overall diffusion rate is likely to be more rapid than the rate for diffusion through the matrix when diffusion along grain boundaries is considered. Thus, a more appropriate value for D is 10^{-8} cm^2/s which gives a value for k on the order of 10^{-14} cm^3/s. Using an initial radius of 1 micron, a final radius of 5 microns is predicted for a time of 3 hours. This is within the range of results seen experimentally. Thus, the increase in average size of the oxide particles and decrease in number of particles can be explained by diffusion controlled coarsening theory.

4.2.4 Explanation of Ag Band Thickening

The coarsening of the Ag band was more complicated to predict than that of the oxide phase. No model for this situation was found. Allen [72] indicated that

the Ag bands could be considered as infinite plates adjacent to two-phase bodies. The surface of the plates are regions of infinitely high curvature. Since matter moves from regions of low curvature to regions of high curvature, the plates are predicted to thicken with longer hold times. This is the behavior seen in the experimental results.

When the Ag layers form and thicken, there is an increasing tendency for the oxide phase to be nearly continuous near the edges of the two-phase Ag/oxide regions. This is due in part to the removal of Ag from the two-phase region leaving á higher concentration of oxide remaining. That is, in a constant volume sample, as the Ag bands thicken, the oxide phase is pushed out of the Ag band region. All of the oxide remains, but it is in a two-phase region of reduced volume. Thus, within the two-phase region, there is a higher concentration of oxide phase remaining, particularly near the edges of the two-phase region.

The increasing tendency for nearly continuous oxide phase near the edges of the two-phase Ag/oxide region may also be due in part to the tendency of oxide superconductors to have preferential faceting along Ag/oxide interfaces [28]. In Ag clad Bi-Sr-Ca-Cu-O materials, there was (001) faceting along the Ag/oxide interface. In the current case, if the Ag bands function the same as the Ag cladding and result in (001) faceting (that is, with the c-axis perpendicular to the interface and thus, perpendicular to the length of the ribbon), this will result in orientations of grains which favor rapid growth along the length of the ribbon.

This type of behavior would also be likely to result in a high concentration of oxide phase extending along the edges of the two-phase Ag/oxide regions. See Figure 3-26 and Figure 3-28 for examples of microstructures in which there is a significant concentration of oxide phase near the edge of the Ag/oxide region. There are some grains that are elongated along the interface indicating that there may be some (001) faceting. There are also many grains located at the interface that are oriented in other directions. This indicates that the oxide phase being pushed out of the thickening Ag band is probably the explanation for most of the increase in concentration of oxide at the edge of the two-phase region.

If oscillations in the surface of the infinite Ag plate are considered, it is possible that the planar front will become unstable and the plate will shrink and eventually disappear. A similar situation in which rod-shaped particles become unstable and eventually form spheres has been examined by Nichols [73] and Cline [74]. This provides another possible explanation for the lack of smoothness at the interface of the Ag bands found in samples Y15-49 and Y15-51 which were exposed to long hold times at high temperatures (10 minutes at 925°C followed by 30 hours at 890°C, and 3 hours at 925°C, respectively).

4.2.5 Summary of Experimental Observations

The experimental observations noted thus far are summarized in Table 4-6. A short explanation of each observation is provided.

Table 4-6. Summary of experimental observations and a brief explanation for each observation.

Observation	Explanation	Relevant Section
During low temperature oxidation stage:		
Y_2O_3, BaO, CuO in Ag	Internal oxidation results in formation of elemental oxides of solute elements.	4.1.1
Solute depletion at center of sample	Due to outward diffusion of solute elements during oxidation.	4.1.1
Ag nodules at surfaces	Due to stress relief associated with the volume change during internal oxidation.	4.1.1
During high temperature transformation stage:		
$Y_1Ba_2Cu_3O_{7-x}$ grains in Ag	Transformation of the elemental oxides to superconducting oxide.	4.2
Ag bands at surfaces	Ag nodules formed during oxidation spread out to form surface Ag bands.	4.2
Ag band at center	Due to the outward diffusion of solute during complete internal oxidation.	4.2
Oxide phase coarsening	Ostwald ripening theory.	4.2.3
Ag band thickening	Coarsening theory if bands are considered as infinite plates (infinitely high curvature) adjacent to two-phase bodies.	4.2.4

Section 4.3 Effect of the Temperature Gradient

An effect due to processing in the temperature gradient is consistently seen. The Ag bands tend to be more clearly defined as a result of processing in the temperature gradient. Within the two-phase Ag/oxide regions, the oxide phase tends to be more connected. Often, the oxide phase is nearly continuous at the edges of the two-phase region as a result of processing in the temperature gradient. However, there is no indication of the superconductor grains being elongated along the length of the ribbon or oriented in any preferential direction.

4.3.1 Increased Degree of Banding

The effect of the temperature gradient on the degree of banding may be seen by comparing sample Y15-11 to sample Y15-9, and sample Y15-8 to sample Y15-4 (see Table 4.7). All of these samples had no prior oxidation treatment. Samples Y15-11 and Y15-8 were given treatment TG slow to 900°C with no hold and a 3 hour hold, respectively. Samples Y15-9 and Y15-4 were given high temperature transformation treatments of 10°C/min to 900°C with no hold and a 3 hour hold, respectively. In sample Y15-11, the oxide phase is coarser and has a higher degree of connectivity than in sample Y15-9. There is an Ag band present in the center of sample Y15-11 for most of the sample. There is no indication of this type of band forming in sample Y15-9. In both samples, there are a small number of Ag nodules present on the surface. In sample Y15-8, there are Ag bands at both surfaces and at the center of the sample. Within the two-phase Ag/oxide regions, the oxide phase has some regions in which it is nearly continuous at the edge of the two-phase region. This behavior is not seen throughout the entire sample. Sample Y15-4 does not have clear Ag bands at either the surfaces or the center of the sample, although there are some regions in which the oxide phase has coalesced with barium cuprate to form long aggregate regions (refer to Figure 3-17). The differences in the microstructure of these samples indicates that processing in the temperature gradient furnace encouraged more complete oxidation of the sample. This may be due to a longer exposure time at high temperatures than in the similar

experiments done in an isothermal furnace and is not necessarily a direct effect of the temperature gradient.

Table 4.7. Comparison of samples showing increased degree of banding due to temperature gradient processing.

Sample	Oxidation Treatment	High Temp. Treatment	Observed Results	Explanation
Y15-9	No-Ox	10°C/min, no hold	Small oxide phase particles, Ag nodules, no banding	Processing in the temperature gradient furnace encouraged more complete oxidation of the samples
Y15-11		TG slow, no hold	Oxide phase coarser and more connected, Ag nodules, center band	
Y15-4	No-Ox	10°C/min, hold 3 hours	Oxide phase aggregates, no bands	
Y15-8		TG slow, hold 3 hours	Ag and Ag/oxide bands	
Y15-15	Ox-NH	10°C/min, no hold	minimal Ag banding on one surface	Differences in microstructure can be explained by difference in oxidation treatment (see Section 4.1.2), not necessarily as a direct effect of TG processing
Y15-34 and Y15-38	Ox-13	TG fast, hold 10 min	discontinuous Ag bands	
Y15-16	Ox-NH	10°C/min, hold 3 hours	No bands	
Y15-33	Ox-13	TG fast, hold 3 hours	Ag bands at surface and center	
Y15-39	Ox-13	TG fast, hold 10 min, anneal 3 hours		

The effect of TG fast may be seen by comparing samples Y15-34 and Y15-38 to sample Y15-15, and samples Y15-33, Y15-35, and Y15-39 to sample Y15-16.

All of the samples that were given treatment TG fast (Y15-34, Y15-38, Y15-33, Y15-35, and Y15-39) first received oxidation treatment Ox-13; samples Y15-15 and Y15-16 were given oxidation treatment Ox-NH. Thus, the differences in the microstructures of these samples is due largely to the different oxidation treatment.

Samples Y15-34 and Y15-38 were given treatment Ox-13 followed by TG fast to 900°C with a 10 minute hold. Sample Y15-15 was given treatment Ox-NH followed by a high temperature treatment of 10°C/min to 900°C with no hold. In samples Y15-34 and Y15-38, there are discontinuous bands of Ag at the surface 2 to 3 microns thick. Sample Y15-15 has only a minimal amount of Ag on one surface and none on the other surface. In the regions of samples Y15-34 and Y15-38 in which the Ag bands are continuous, there is also a nearly continuous oxide phase located adjacent to the Ag band. This is the expected difference in final microstructure for the difference in oxidation treatment and does not indicate any direct effect of processing in the temperature gradient furnace.

Samples Y15-15 and Y15-16 were given treatment Ox-NH followed by a high temperature treatment of 10°C/min to 900°C with no hold and a 3 hour hold, respectively. Samples Y15-33 and Y15-35 were given identical treatments of Ox-13 followed by TG fast to 900°C with a 3 hour hold. Sample Y15-39 was given treatment Ox-13 followed by TG fast to 900°C with a 10 minute hold and a 3 hour anneal at 890°C. Samples Y15-33 and Y15-39 have Ag bands at the

surfaces and at the center of the sample. The bands are nearly continuous, but not consistently straight or of a uniform thickness. Within the two-phase Ag/oxide regions, there is a tendency for the oxide phase to be present at the edge of the two-phase region. In samples Y15-15 and Y15-16, there are no bands present. These differences in microstructure are due largely to the difference in oxidation treatment and do not indicate any direct effect of processing in the temperature gradient. Sample Y15-35 has an unusual microstructure in which the oxide phase has coarsened into large (often > 10 micron) isolated particles. There is no indication of banding in this sample. No explanation for the microstructure of this sample, which was treated in the same way as sample Y15-33, is available.

4.3.2 Effect of the Additional Heating Coil During Thermal Gradient Processing

An effect due to the presence of the additional heating coil during processing in the temperature gradient furnace was seen. The additional coil increased the tendency for well-delineated Ag bands to form and increased the tendency of the oxide phase to be continuous at the edges of the two-phase regions.

The effect of the additional heating coil may be seen by comparing sample Y15-47 to samples Y15-34 and Y15-38, sample Y15-36 to samples Y15-33 and Y15-35, and sample Y15-48 to sample Y15-39 (see Table 4.8). All of these samples received oxidation treatment Ox-13. Samples Y15-47, Y15-36, and Y15-48 were given treatment TG fast with the Coil to 900°C and held for 10

minutes, 3 hours, and 10 minutes followed by a 3 hour anneal at 890°C, respectively. The samples to which each of these will be compared were given treatment TG fast without the coil and given the same hold times. The samples treated with the coil all have well developed Ag bands of a uniform thickness and very well connected oxide phase. The bands are more clearly defined than in the samples treated without the coil, and there is a greater tendency for the oxide phase to be continuous at the edge of the two-phase Ag/oxide regions.

Table 4.8. Comparison of samples showing effect of additional heating coil.

Sample	Oxid. Stage	Ramp Rate	Hold & Anneal	Observed Results	Explanation
Y15-47	Ox-13	TG fast with coil	hold 10 min	uniform, well-developed Ag bands, well connected oxide phase in Ag/oxide bands	Use of the additional heating coil results in increased banding and increased connectivity of the oxide phase within the Ag/oxide bands. This may be due to a shift in the temperature gradient such that less heat is dissipated during the transformation
Y15-34 and Y15-38		TG fast		less uniform bands, less oxide phase connectivity	
Y15-36	Ox-13	TG fast with coil	hold 3 hours	uniform, well-developed Ag bands, well connected oxide phase in Ag/oxide bands	
Y15-33		TG fast		less uniform bands, less oxide phase connectivity	
Y15-48	Ox-13	TG fast with coil	hold 10 min, anneal 3 hours	uniform, well-developed Ag bands, well connected oxide phase in Ag/oxide bands	
Y15-39		TG fast		less uniform bands, less oxide phase connectivity	

Sample	Oxid. Stage	Ramp Rate	Hold & Anneal	Observed Results	Explanation
Y15-53	Ox-NH	TG fast with coil	hold 10 min	Ag and Ag/oxide bands in some places	The use of the additional heating coil increases the degree of banding and the continuity of the oxide phase within the Ag/oxide regions. However, TG processing with the coil will not result in uniform, well-developed bands unless oxidation treatment Ox-13 (complete oxidation) is used.
Y15-15		10°C/ min	no hold	minimal banding at one surface	
Y15-21	Ox-NH	TG fast with coil	hold 3 hours	minimal center band in some places	
Y15-54		TG fast with coil	hold 10 min, anneal 3 hours	Ag and Ag/oxide bands	
Y15-16		10°C/ min	hold 3 hours	no banding	

The combined effect of the temperature gradient and the heating coil on samples which received oxidation treatment Ox-NH may be isolated from the effect of oxidation treatment by comparing sample Y15-53 to sample Y15-15, and samples Y15-21 and Y15-54 to sample Y15-16. All of these samples were given oxidation treatment Ox-NH. Samples Y15-15 and Y15-16 were given a high temperature treatment of 10°C/min to 900°C with no hold and a 3 hour hold respectively. Samples Y15-53, Y15-21, and Y15-54 were given treatment TG fast with the coil to 900°C and held for 10 minutes, 3 hours, and 10 minutes with a 3 hour anneal at 890°C, respectively. In the samples given treatment TG fast with the coil, there is some tendency for banding that is not present in the samples treated without the temperature gradient. Sample Y15-53 has Ag

bands at the surface and in the center in part of the sample and no banding in other parts of the sample. Sample Y15-21 shows only a minimal tendency to form a band in the center in one part of the sample and no banding in other parts of the sample. Sample Y15-54 has Ag bands at both the surfaces and the center of the sample. The bands are much less uniform than in the samples that were given oxidation treatment Ox-13 prior to being given treatment TG fast with the coil. Thus, it is concluded that the use of the additional heating coil increases the degree of banding and the continuity of the oxide phase within the two-phase region. However, treatment in the temperature gradient with the additional heating coil will not produce uniform, well-developed bands unless the oxidation treatment Ox-13 (complete oxidation) is used.

One possible explanation for the effects of the additional heating coil is that in shifting the temperature gradient towards the cold end of the system, the location of the region in which transformation took place was shifted so that it was in the region of the alumina tube in contact with the insulating layer at the bottom of the furnace (see Figure 4-2). This insulation surrounding the alumina tube in the region of the reaction could have slowed the dissipation of the heat that was generated as a result of the transformation. The additional heating coil is located much closer to the sample than the original heaters; this positioning may also decrease the rate of heat dissipation. It is possible that this has the effect of increasing the temperature seen by the sample, while not being

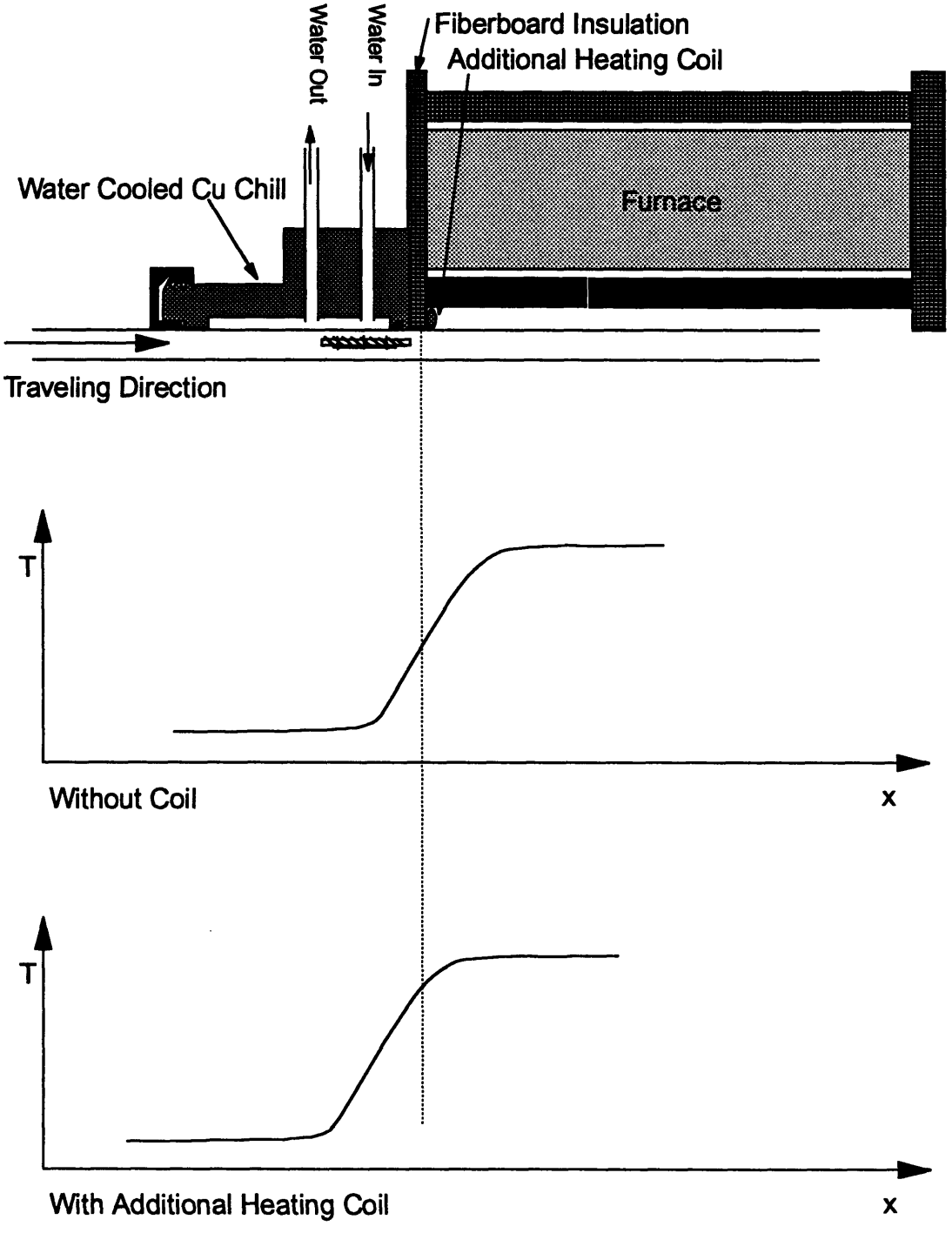

Figure 4-2. Schematic of thermal gradient furnace and temperature shift associated with the use of the additional heating coil.

recorded on the thermocouple that was located 2 to 5 millimeters above the top of the sample.

In order to determine the difference in temperature seen by the sample as a result of the use of the additional heating coil, a determination of the heat generated by the reaction was made. The Gibbs free energy for the transformation from elemental oxides to the $Y_1Ba_2Cu_3O_{6.5+y}$ phase is

$$\Delta G^0_{123+y} = -109.0 + 4.6 \times 10^{-3} T + 6.7 \times 10^{-3} yT \text{ kJ/mole [75].} \quad (4\text{-}5)$$

At 900°C and y = 0.2, ΔG^0_{123+y} is -102.21 kJ/mole. For each mole of $Y_1Ba_2Cu_3O_{6.5+y}$ present, there are 15 moles of Ag present. Thus, there is 6.81 kJ/mole Ag present if none of the heat generated by the transformation is dissipated. With a value of $\Delta H = 9.63 \times 10^{-3}$ kJ/mole K for Ag (calculated from data presented on a graph in Rosenqvist [32]), this results in the ribbon being heated up to 169 K. Since some of the heat will be dissipated, the actual change in temperature will be less. However, if the presence of the additional coil reduces the rate of heat dissipation significantly, this will result in the sample being exposed to a higher temperature for a longer time in these experiments than in the experiments that were done without the additional heating coil. This may explain the additional tendency for banding seen in the samples treated with the additional heating coil.

Section 4.4 Lack of Elongation and Alignment Due to Thermal Gradient Processing

No elongation of the superconductor phase along the length of the ribbon was seen. Nor was any preferential orientation seen. As mentioned in the Introduction (see Section 1.3), theory for predicting microstructures as a result of processing in a temperature gradient is very limited. At the time these experiments were designed, the modeling attempt that was closest to the current experimental conditions was that of Otto [66]. The relevant equations from Otto's model are presented in Section 1.3 and the derivation of the equations is summarized in Appendix 1. Otto's model predicts a very strong dependence of aspect ratio on temperature gradient. It also predicts a moderate inverse dependence of aspect ratio on velocity. Thus, the samples which were treated with TG slow would be expected to have a larger aspect ratio than the samples treated with TG fast and the samples treated with TG very slow should have even larger aspect ratios. In order to understand the discrepancy between the experimental results and the predictions made by Otto's model, it is necessary to reconsider what happens during nucleation and growth for the specific case of multiple elemental oxides transforming to the superconducting oxide in the presence of a noble metal. Section 4.4.1 will examine nucleation and section 4.4.3 will examine growth. Section 4.4.2 will examine the likelihood of rotation of the superconducting grains after nucleation. Section 4.4.4 will provide a summary of these predictions.

4.4.1 Nucleation

Nucleation of a new phase in a single phase solid material would generally result in randomly oriented nuclei. In the current case, the presence of a temperature gradient and the fact that the starting material is multiphase must be considered. In the following discussion, nuclei refer to the nuclei of the oxide phase that will become the superconducting phase upon oxygenation.

4.4.1.1 Nucleation in a Temperature Gradient

In order to determine the effect of processing in the temperature gradient furnace on the nucleation, it is beneficial to calculate the ratio of the nucleation rate at the hot end of a nucleus to the nucleation rate at the cooler end of the same nucleus.

Consider critical nucleus lengths of 20A and 30A. Also consider a worst case critical nucleus length of 300A. For a temperature gradient of 250°C/cm, the temperature difference over the nucleus length, is 5×10^{-5} °C, 7.5×10^{-5} °C, and 7.5×10^{-4} °C.

The nucleation rate, I, is related to temperature, T (K), such that

$$I \propto \exp -\left[\frac{\Delta H_a'}{kT} + \frac{A}{RT(\Delta T)^2}\right] \approx \exp -\left[\left(\frac{1}{T}\right)\left\{\frac{\Delta H_a'}{k} + \frac{A}{R(\Delta T)^2}\right\}\right] \qquad (4\text{-}6)$$

where $\Delta H'_a$ is the free energy associated with an atom jumping across the energy barrier between an adjacent grain and the nuclei in J, $k = 1.38 \times 10^{-16}$ erg/K is Boltzmann's constant, $R = 8.3 \times 10^{7}$ erg/mol K is the gas constant, ΔT is

the difference between T and the equilibrium transition temperature in K, and $A/(\Delta T)^2$ is the free energy associated with the formation of a nucleus. Assuming values of $\Delta H_a^{'} = 1$ eV $= 3.2 \times 10^{-13}$ erg, and $A/(\Delta T)^2 = 10^{11}$ erg/mol gives a value of 3500 for the $\Delta H_a^{'}/k + A/R(\Delta T)^2$ term in equation 4-6. If T is around 1100 K then the ratio of I $(T+7.5 \times 10^{-4})$ to I(T) is 1.0000021. Thus, even for the worst case analysis, the effect of the temperature gradient on nucleation is negligible. Since the effect of the temperature gradient is negligible, the nuclei will be oriented randomly in this case as in the case of a single phase solid material during an isothermal transformation.

4.4.1.2 Nucleation in a Multi-Phase Material

Nuclei are most likely to form at heterogeneous nucleation sites. In a polycrystalline material, grain boundaries and triple points provide likely nucleation sites. In the current experiments, the interfaces and triple points between elemental oxide grains are particularly good nucleation sites because the necessary elements are readily available. That is, the Y, Ba, Cu, and O needed to form a critical nucleus only need to diffuse short distances and the grain boundaries provide a likely rapid diffusion path.

The orientation of a particular nucleus may well be influenced by the orientation of the interface at which it is forming. Nuclei which are located such that the fastest growth direction lies along a triple junction line or, to a lesser extent, along an interfacial boundary are favored because of the short diffusion

distances required to form these nuclei. This preference for nucleation at triple junction lines is shown schematically in Figure 4-3. However, on a global scale, the interfaces and triple junction lines are located at a wide variety of orientations. Thus, the resulting nuclei, even though they may have been influenced by the local orientation of interfaces, appear to be randomly oriented throughout a sample. This is supported by the experimental results which show that the grains of the superconductor phase have randomly distributed orientations (for example, see Figure 3-28).

4.4.2 Rotation

It was shown in the Section 4.4.1 that nucleation will result in nuclei which have a random distribution of orientations. It is necessary to consider the possibility that the superconductor grains will rotate after nucleation. Rotation of superconductor grains has been observed in some cases where a uniaxial compressive stress [76] or a magnetic field [77-79] was applied. In the case of the uniaxial compressive stress, the reduction of stress that results upon rotation provides a driving force for rotation. Thus, the application of a uniaxial compressive stress may be used to align superconductor grains. Similarly, when a magnetic field is applied and the superconductor grains are above a critical size, there is a driving force for the magnetic domains within individual grains to align themselves parallel to the magnetic field in order to reduce the energy of the system. In the presence of a thermal gradient, there is no energy reduction

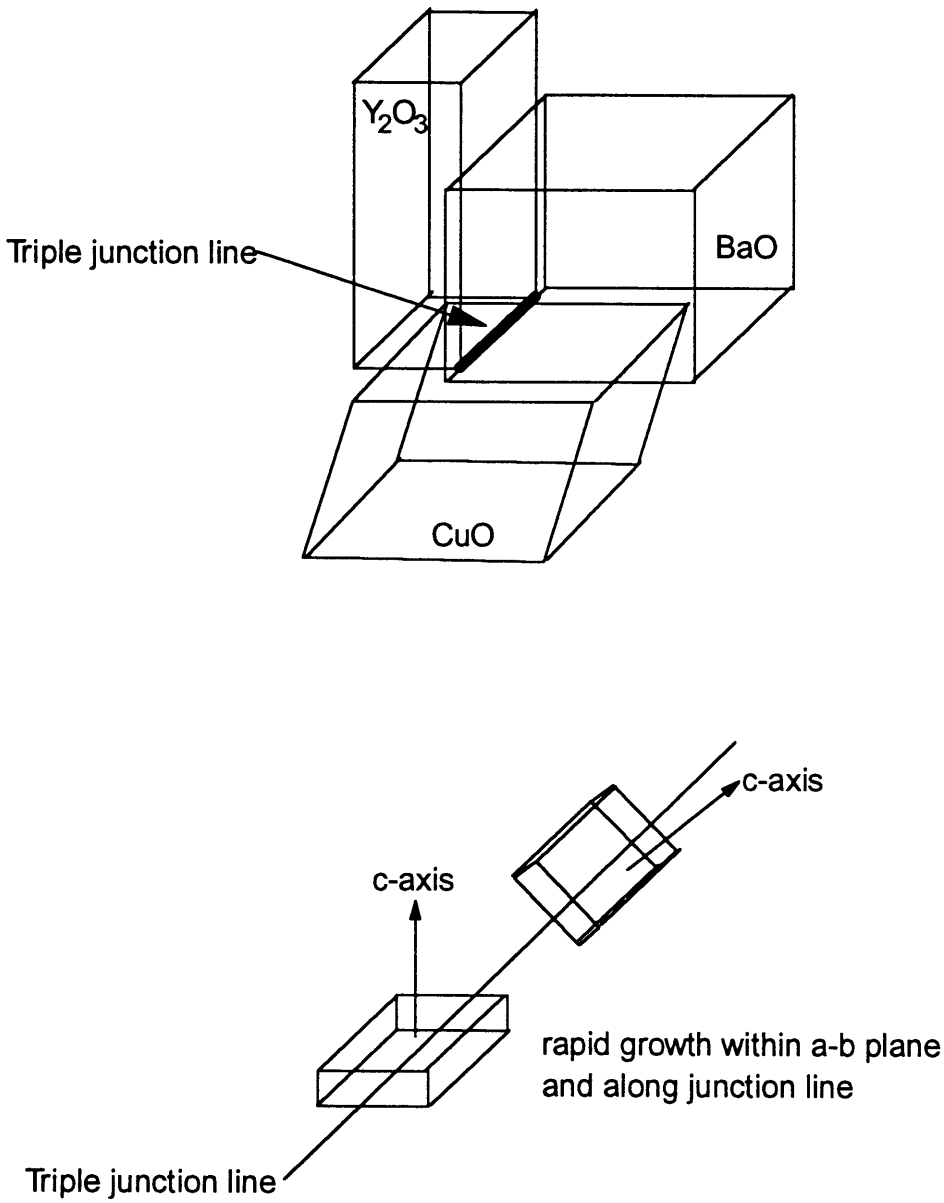

Figure 4-3. Schematic of nucleation at triple junction lines.

by alignment of grains in any particular direction. Thus, there is no driving force for rotation of the superconductor grains after nucleation. Each grain will continue to have the same orientation as its nucleus and the overall result will be grains with a random distribution of orientations.

4.4.3 Growth

Consider the case where a sample is traveling up a temperature gradient. When the sample reaches temperature T_n, nucleation will occur. See Figure 4-4 for a schematic illustration. As shown in the previous section, the nuclei will have random orientations and will often be located at boundaries and triple points between elemental oxide grains.

According to Otto's model, growth will be sufficiently rapid that the grains will extend down the gradient to a temperature T_g where the growth rate is equal to the traveling velocity. If $T_g < T_n$, then nucleation will be suppressed and the grains will extend the length of the sample. See Figure 4-5 for a schematic illustration. If $T_n < T_g$, then nucleation will occur in each segment of sample as it reaches T_n. See Figure 4-6 for a schematic illustration. In the steady state condition, the elongation of the grains may be predicted using the equation

$$\Phi = \frac{E_r^3 m^4 v^4 (E_n+2E_r)^{\frac{3}{2}}}{2\pi B_n B_r^3 E_n^{\frac{1}{2}} T_g^8 k^4 \exp\left(\frac{-(E_n+E_r)}{kT_g}\right)} \qquad (4\text{-}7)$$

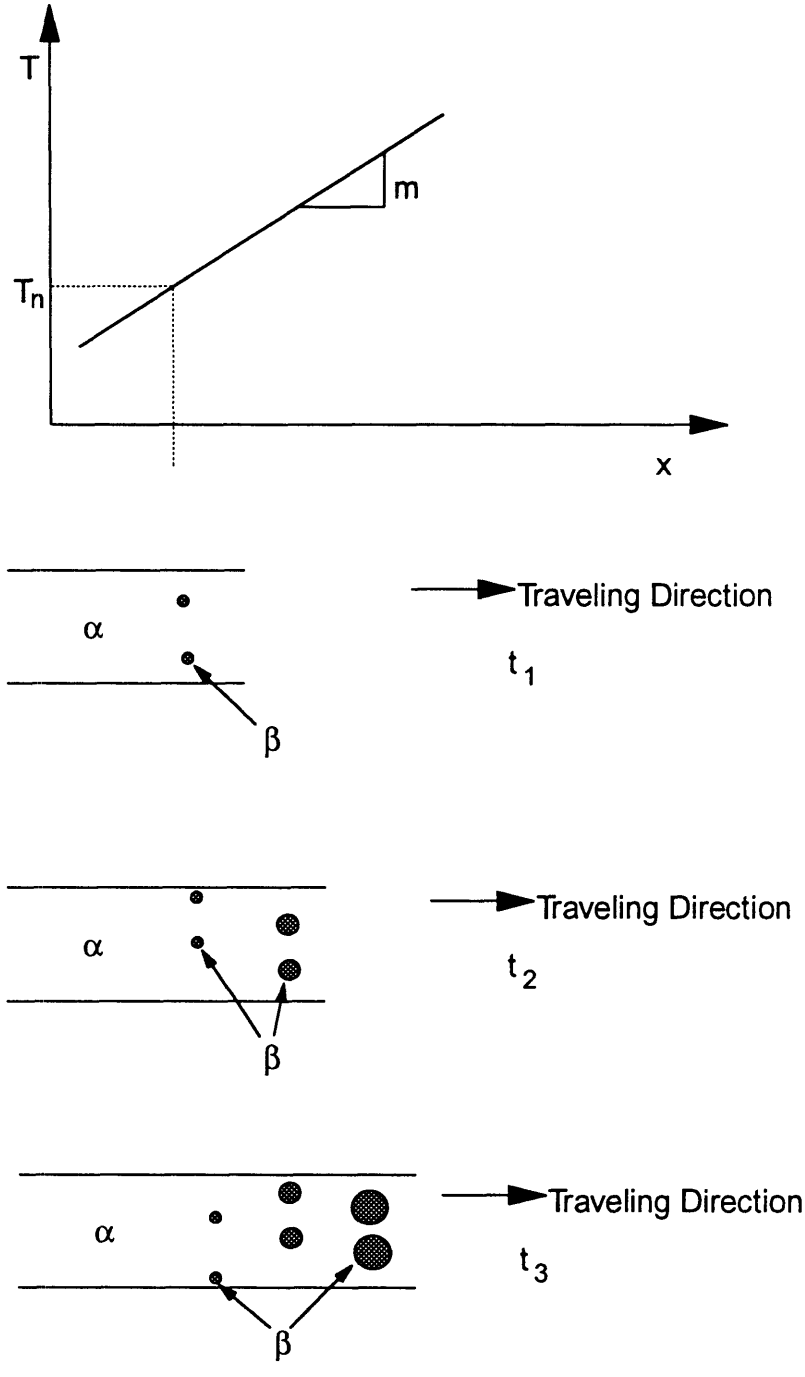

Figure 4-4. Schematic illustration of nucleation at T_n.

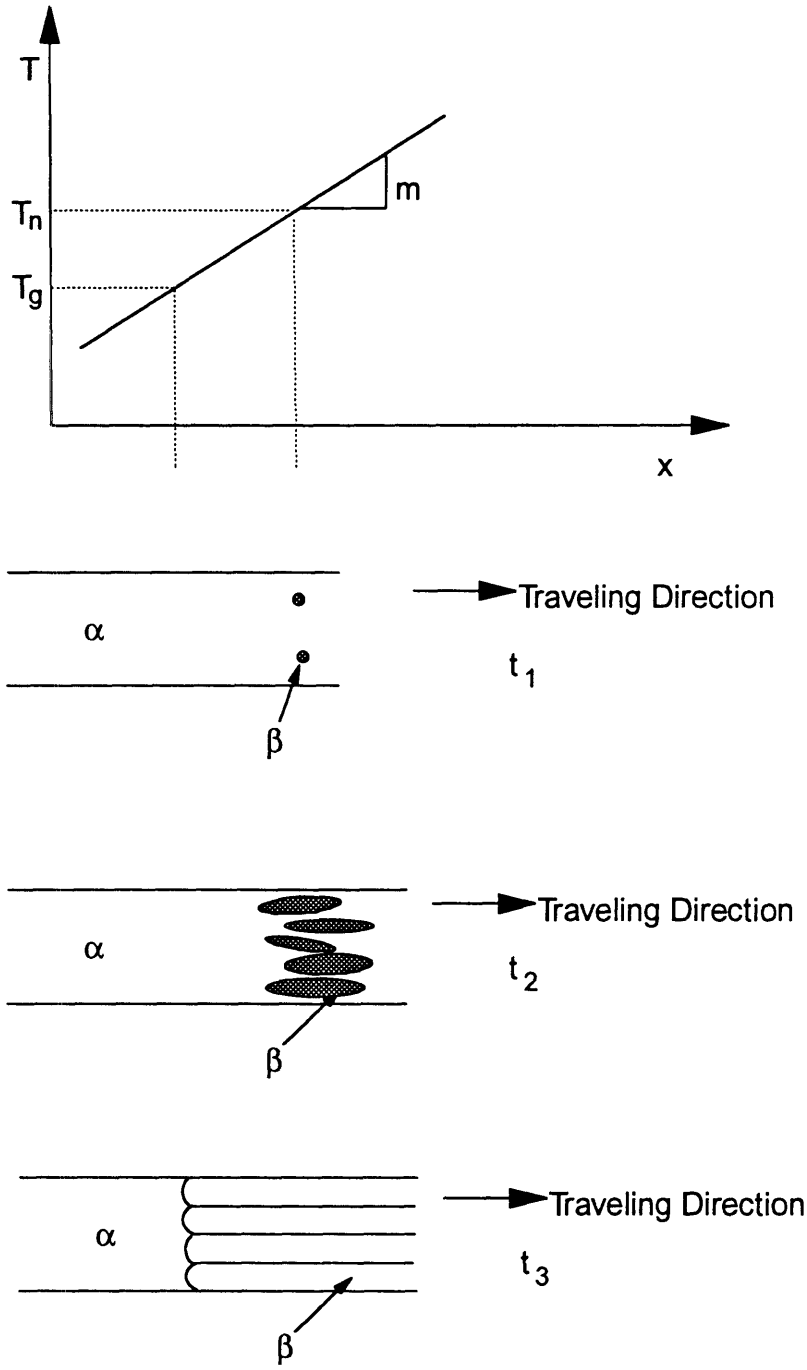

Figure 4-5. Schematic illustration of thermal gradient processing when $T_g < T_n$ and the new grains fill the cross section of the sample.

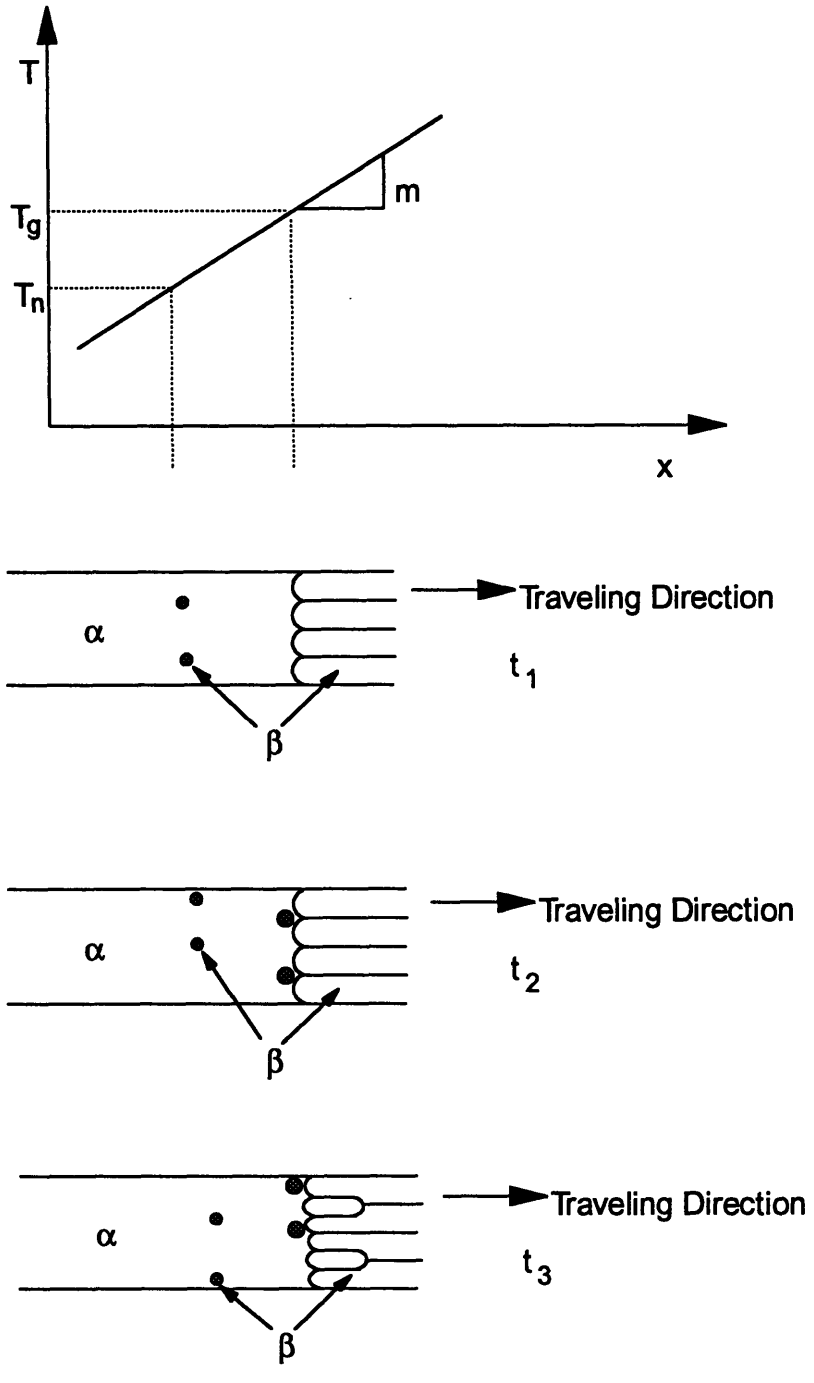

Figure 4-6. Schematic illustration of thermal gradient processing when $T_n < T_g$ and the new grains fill the cross section of the sample.

where Φ is the aspect ratio, m is the temperature gradient, v is the traveling velocity, E_n and E_r are the activation energies for nucleation and growth, B_n and B_r are the nucleation and growth rate coefficients when the Arrhenius approximation to the temperature dependence is used, and k is Boltzmann's constant. This method of approximation may be valid for some single-phase isotropic materials.

However, in the present experiments, the additional factors of the multi-phase starting material (including the presence of the noble metal) and the anisotropic growth of the superconducting phase grains must be considered. Once again, the schematic illustration of thermal gradient processing shown in Figure 4-4 is considered and growth is assumed to occur on nuclei of random orientations.

4.4.3.1 Multi-Phase Considerations

Growth may occur only when a sufficient number of atoms of each element of the growing phase are present. Thus a supply of Y, Ba, Cu, and O must all be present for growth of the superconductor grain to continue. Oxygen can effectively be ignored because it will be present whenever the metallic elements from the elemental oxides, Y_2O_3, BaO, and CuO, are present. Also, the superconductor can be O deficient. Diffusion of the metallic elements may occur through the grains and along grain boundaries. Diffusion along grain boundaries is likely to be the rapid diffusion path. When all of the nearby

sources of these elements have been consumed and these elements have to diffuse over longer distances, the growth rate will decrease. When all of one of the elements has been entirely consumed by the various superconductor grains in a particular segment of the sample, growth is effectively stopped. The grains will continue to coarsen as shown in Section 4.2.3. At this stage the process resembles two-phase coarsening with grains of superconductor and grains of Ag present.

Impingement never forces the grains to become elongated along the length of the sample. The grains effectively stop growing before they impinge due to a lack of the necessary metallic elements. Ag remains to effectively separate the superconductor grains. The conditions modeled by Otto are different; when considering only a simple transition (α -> β), it is reasonable to assume that the grains grow until the entire cross section has been transformed to the new phase. Thus impingement must occur. In the current case, the grains effectively stop growing when they run out of available metallic elements (Ag remains). Impingement does not occur to force the grains to extend along the length of the ribbon.

The differences between the physical conditions considered by Otto's model and the experimental conditions and the subsequent difference in microstructure are shown in Figure 4-7. In both cases, new grains are nucleated at T_n. When the grains grow beyond a certain size, the cases differ greatly. In the case

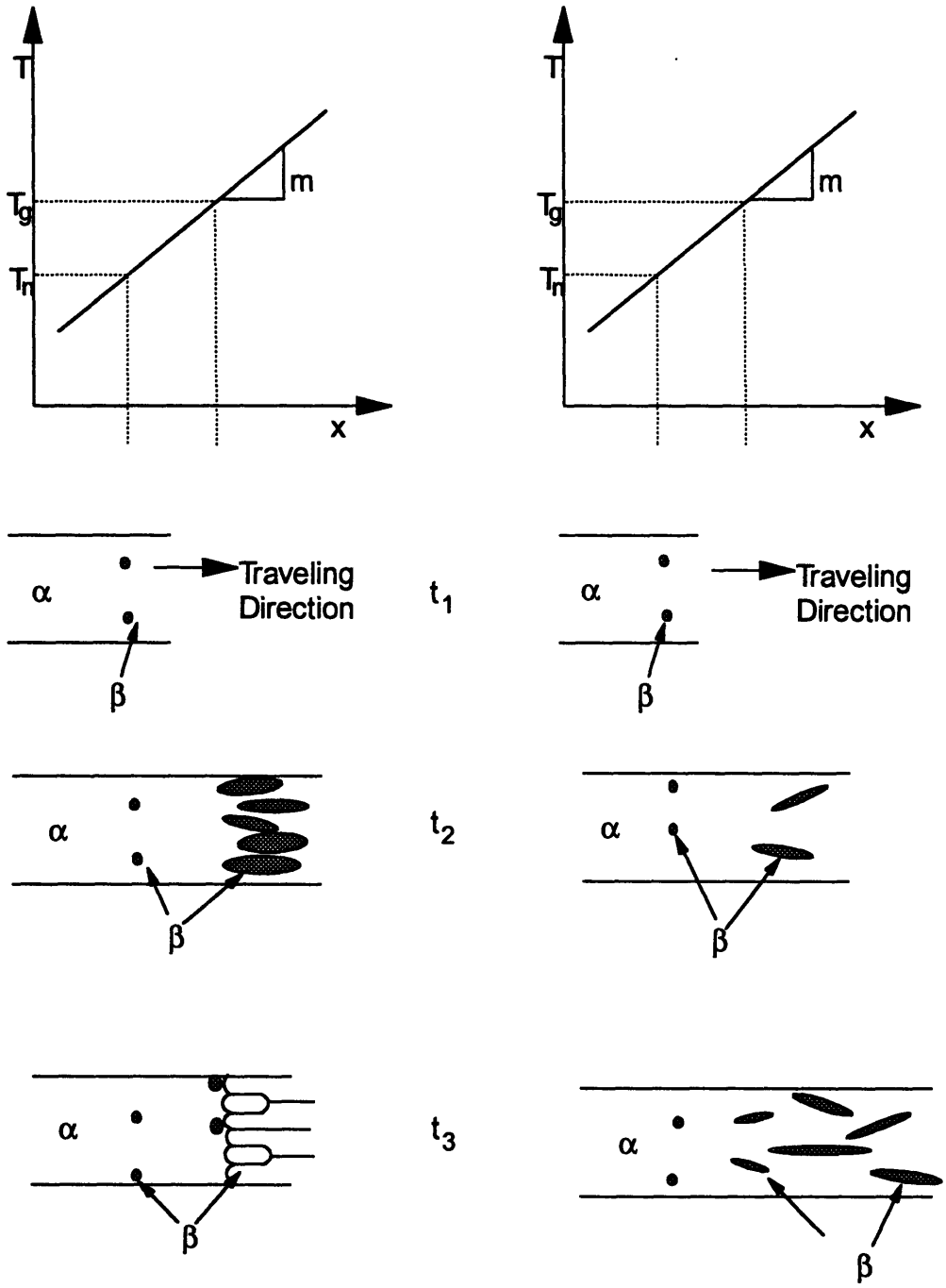

Figure 4-7. Illustration of difference in microstructure resulting from difference in physical conditions between case modeled by Otto and experimental conditions.

treated by Otto, the grains grow until they fill the entire cross section. That is, the material is entirely transformed to the new phase and impingement of the grains must occur. This results in the grains being able to extend down the gradient to form a growth front at T_g. During the conditions seen experimentally, the growth of the new grains is effectively stopped when the necessary elements are consumed. Thus, the Ag phase remains to separate the superconducting oxide grains and very little impingement of the new oxide grains occurs. This effective halting of the growth of the oxide grains means that the grains do not form a growth front at T_g. Instead, the resulting microstructure is that of isolated grains of oxide surrounded by Ag and occasionally other phases such as barium cuprates.

The presence of Ag grains around the superconductor grains as well as the presence of voids, grains, and other phases such as barium cuprates results in the superconductor phase not having a continuous path along the length of the ribbon as needed for carrying a supercurrent. The effect on the superconducting properties will be discussed further in Section 4.5.

Although the presence of the Ag complicates the process and prevents significant impingement of the oxide grains, it is not possible to merely remove the Ag from the precursor ribbon. In the Y-Ba-Cu system, 33 wt% Ag was necessary to form a miscible liquid from which a homogeneous precursor ribbon could be melt-spun [26]. This corresponds to a precursor of $Y_1Ba_2Cu_3Ag_{2.5}$. The

addition of more Ag results in a considerable increase in the ductility of both the precursor and the composite ribbon, enabling the experiments to be carried out without breaking the samples. The additional Ag also reduces the likelihood that the sample will disintegrate upon oxidation. When a sample with a low Ag content is oxidized, the stresses due to the change in volume due to oxidation may not be entirely relieved by Ag traveling to the surface and the samples sometimes form a powder rather than an oxide/metal composite ribbon [80].

4.4.3.2 Anisotropic Growth

If the transition to the superconductor phase is carried out isothermally, the anisotropic growth rates result in the formation of plates which extend in the a-b plane. Growth is slowest in the c-direction (by approximately an order of magnitude). Thus a grain would grow as shown in Figure 4-8.

If anisotropic growth in the presence of a temperature gradient is considered for the single phase case treated by Otto, the aspect ratio of new grains which embed in the growth front at T_g will be influenced by their orientation. The grains which are oriented with their fast growth direction along the length of the ribbon will grow fast enough to extend to the growth front at T_g until a new grain occludes that space. Grains which are oriented in other directions will not grow fast enough to remain at the T_g growth front of the fast growth direction. The slower growth directions would have a higher theoretical T_g value because of their slower growth rate for any given temperature. Thus, grains which are not

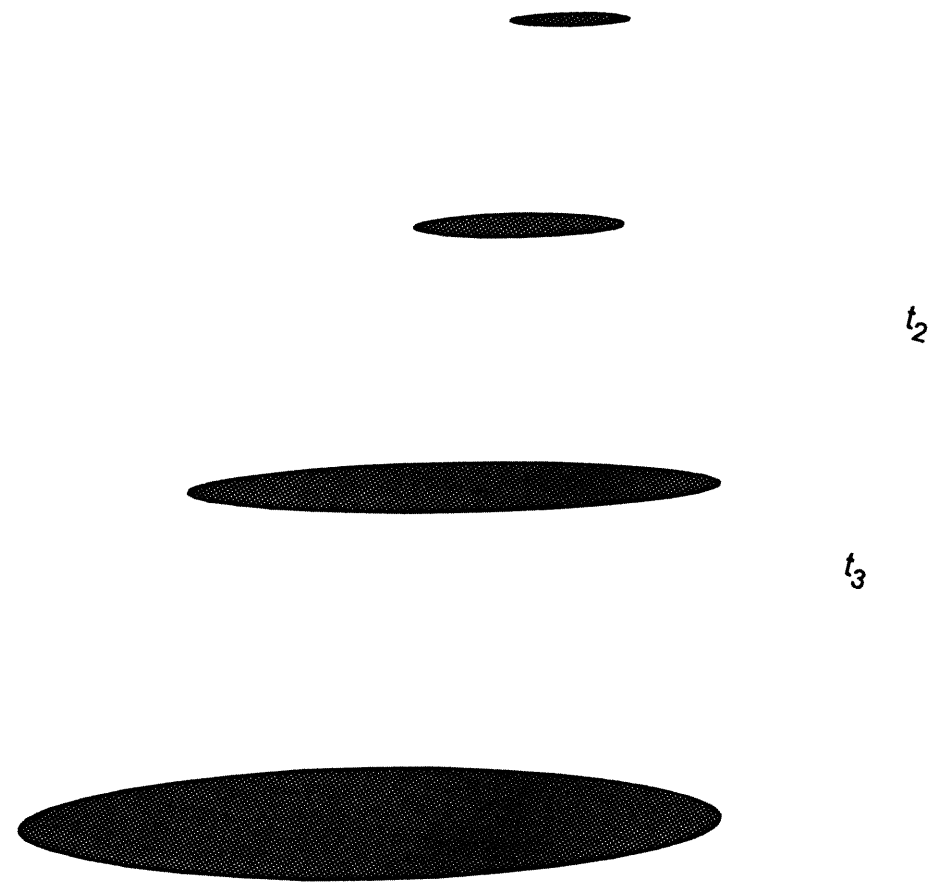

Figure 4-8. Schematic illustration of isothermal anisotropic growth.

oriented with their fast growth direction along the length of the ribbon will have a shorter length and a correspondingly smaller aspect ratio than that predicted by Otto. The grains which are oriented favorably to remain at the growth front at Tg must then expand to fill the cross section of the ribbon in the area left unoccupied by the less favorably oriented grains. This results in a larger than initially predicted cross section per grain and a correspondingly reduced aspect ratio. Thus, anisotropic growth during solid state thermal gradient processing results in grains having a variety of aspect ratios which depend on their orientation and an overall aspect ratio that is less than that predicted for isotropic grains with a growth rate equal to that of the fast growth direction in the anisotropic grains. This occurs when the new grains expand to fill the cross section of the ribbon and the grains impinge.

In the multiphase case seen experimentally, significant impingement does not occur. In order to examine the effect of anisotropic growth in the presence of a temperature gradient for the multiphase case, it is necessary to consider two conditions. The first condition is when the growing grain does not extend sufficiently far down the temperature gradient to reach T_g. The other condition is when the grain does reach T_g. In both cases, a grain can be treated independently of surrounding superconductor grains because growth will usually stop before impingement occurs to any significant degree.

The relative frequency of occurrence of these two conditions depends on whether or not T_n is less than T_g. If $T_n < T_g$, then grains nucleate and grow as they travel up the gradient to T_g. If all of the necessary elements are still available, then a growth front for the individual grain will be established at T_g. When there are no longer sufficient elements available to maintain a growth rate equal to the traveling velocity, the grain will travel away from the growth front. If $T_g < T_n$, then a segment of sample travels up the temperature gradient to T_n where nucleation of new superconductor grains can occur. The temperature is high enough that rapid growth takes place immediately in all directions on a new nuclei. A schematic illustration is shown in Figure 4-9. Depending on the orientation of the grain and the availability of the necessary elements, the grain may grow rapidly enough to extend down the gradient to Tg until the required elements are no longer available.

For the first condition, where no growth front is encountered, growth will occur in all directions. The most rapid growth will occur in the a-b plane and slower growth will occur in the c-direction. The effect of the temperature gradient can be determined by calculating the difference in growth rate at the hot and cold ends of the grain due to the difference in temperature at these locations.

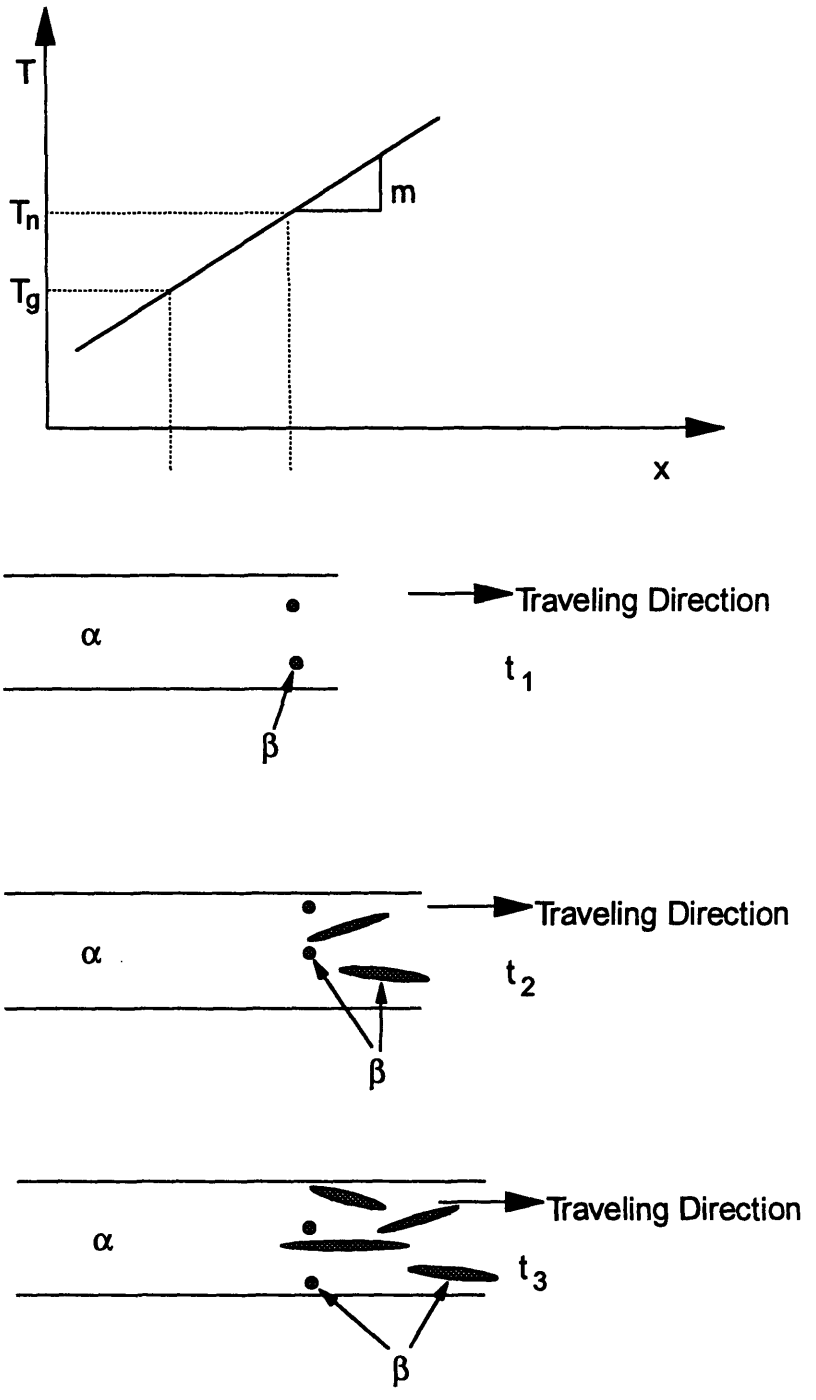

Figure 4-9. Schematic illustration of thermal gradient processing when $T_g < T_n$ but new grains do not expand to fill the cross section of the sample.

The growth rate is dependent on the diffusion rate which is a function of temperature such that

$$D \propto \exp -\left(\frac{\Delta H}{kT}\right) \tag{4-8}$$

where D is the diffusion constant, ΔH is the free energy associated with the diffusion, k is Boltzmann's constant, and T is temperature in K. The ratio of the diffusion rate at the hot end of a grain to the diffusion rate at the cold end of the grain is

$$\frac{D_h}{D_c} = \exp\left(\frac{-\Delta H}{kT_h} + \frac{\Delta H}{kT_c}\right) \tag{4-9}$$

where T_h and T_c are the temperatures at the hot and cold ends of the grain, respectively. Consider grains having lengths of 50A, 0.05 microns, and 5 microns. The gradient is on the order of 250°C/cm giving a temperature difference between the ends of 1.25×10^{-5} °C, 1.25×10^{-3} °C, and 1.25×10^{-1} °C, respectively. For the worst case of 0.125°C, if ΔH is on the order of 1 eV, and T_h is 850°C, then the ratio of the diffusion constants is 1.0004. Thus, even in the worst case, the difference can be considered negligible. The temperature gradient does not have a significant effect on the growth of a superconductor grain.

For the second condition, when growth occurs such that the grain extends down the temperature gradient to T_g, it is necessary to consider surface energy. It is reasonable to consider one isolated grain because this is effectively the

case encountered by each superconductor grain until the time that there is a shortage of metallic elements resulting in a slowing of the growth rate. Consider one grain which extends to the growth front at T_g and has a circumference, C, in the plane of the growth front (see Figure 4-10). It is necessary to determine the direction of the next incremental segment of superconductor grain. Assume the superconductor has a surface energy γ_c on surfaces perpendicular to the c-axis, and γ_a on surfaces parallel to the c-axis (perpendicular to the a-axis and b-axis). The next segment could grow perpendicular to the c-axis or parallel to the traveling direction. The angle between the c-axis orientation and the traveling direction is θ. Consider the length of the next segment to be L when measured parallel to the traveling direction.

If the segment is added as a segment whose length is perpendicular to the c-axis of the grain (see Figure 4-10a), then the added surface has a surface energy

$$\Delta G = \frac{\gamma_c LC}{\sin\theta}. \tag{4-10}$$

If the segment is added parallel to the traveling direction (see Figure 4-10b), then the added surface has a surface energy

$$\Delta G = LC\left(\gamma_a \cos^2\theta + \gamma_c \sin^2\theta\right). \tag{4-11}$$

In order for growth perpendicular to the c-axis to be favored,

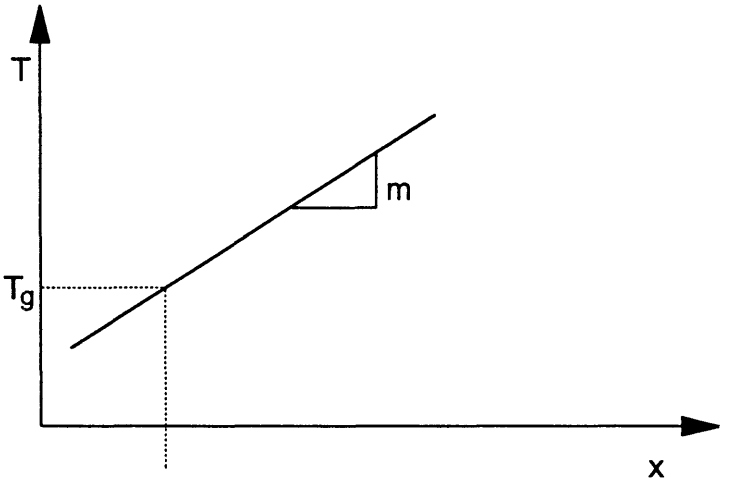

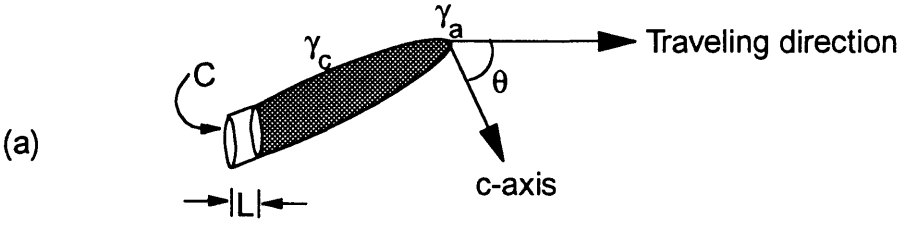

$$\Delta G = \frac{\gamma_c LC}{\sin \theta}$$

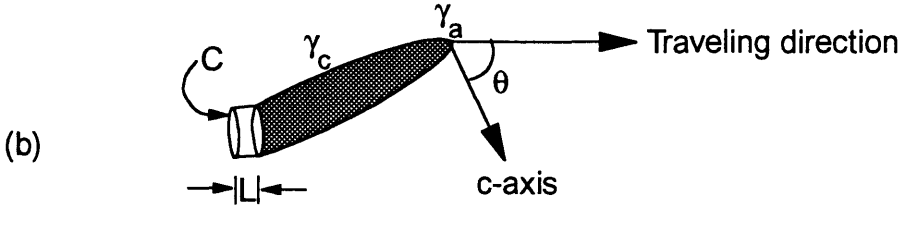

$$\Delta G = LC(\gamma_c \sin^2\theta + \gamma_a \cos^2\theta)$$

Figure 4-10. Schematic illustration of one grain which has grown sufficiently to reach the growth front at T_g with (a) the next segment growing perpendicular to the c-axis of the grain and (b) the next segment growing parallel to the traveling direction.

$$\frac{\gamma_c LC}{\sin\theta} < LC\left(\gamma_a \cos^2\theta + \gamma_c \sin^2\theta\right) \tag{4-12}$$

must be true.

$$\gamma_c < \gamma_a\left(\frac{\cos^2\theta \sin\theta}{1-\sin^3\theta}\right) = \gamma_a f \tag{4-13}$$

If

$$\frac{\gamma_c}{\gamma_a} < f, \tag{4-14}$$

then growth perpendicular to the c-axis direction will be favored. A few values of f for a given angle θ have been tabulated in Table 4-9.

Table 4-9. Tabulated values of f for a given θ.

θ (degrees)	f
0	0
5	0.087
15	0.246
30	0.429
45	0.547
60	0.618
89	0.666
89.9	0.667

At first glance, it appears that when θ is small the energy calculations show that growth parallel to the traveling direction would be favored. However, when θ is small, the growth rate will be slow parallel to the traveling direction. Thus, it is unlikely that a grain oriented in this way would extend far enough down the temperature gradient to reach the growth front. This is illustrated schematically in Figure 4-11. This grain would grow as in the first case presented. Thus, the

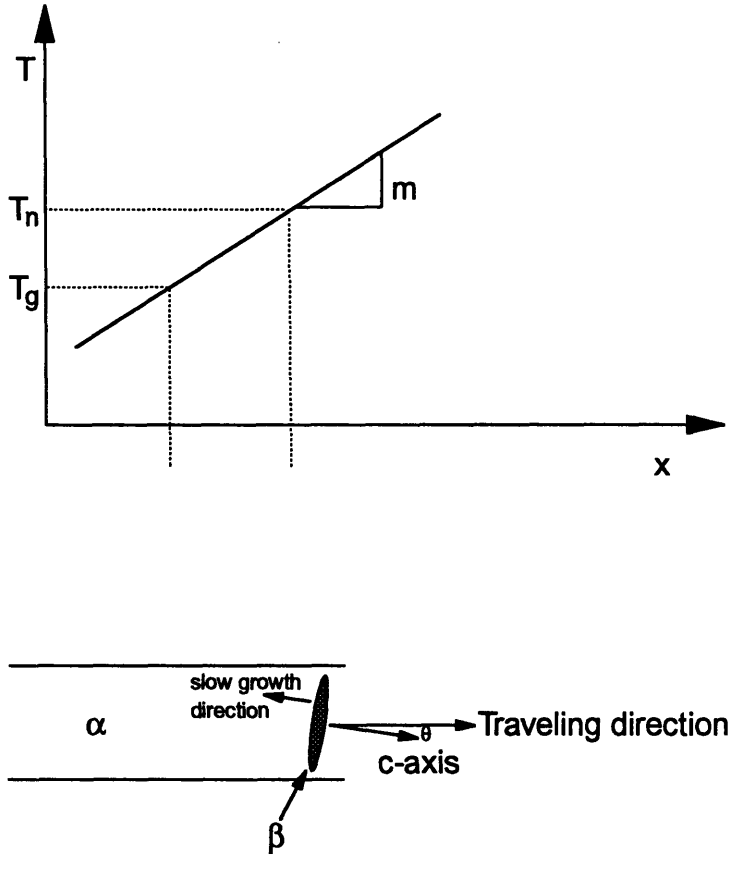

Figure 4-11. Schematic illustration of growing grain when θ is small. Note that it is unlikely for this grain to grow sufficiently to reach T_g.

vast majority of grains will grow along the directions favored by anisotropic growth and not along the traveling direction. When a grain with a small θ does reach the growth front, growth will occur parallel to the traveling direction. Experimentally, these conditions were rarely met. Figure 3-28 contains an SEM photo of sample Y15-70 which clearly shows rectangular superconductor grains (planar in three dimensions) having a wide variety of orientations, not extending along the length of the ribbon. There are also some larger grains which appear less elongated in the plane of the photograph. These are probably planar grains that are intersected at a plane closer to the a-b plane of the grain. This is illustrated schematically in Figure 4-12. Thus, the experimental results agree with the predictions of growth extending in the randomly oriented basal plane, not parallel to the traveling direction.

4.4.4 Summary of Thermal Gradient Processing

When all of the separate parts of the analysis are combined, there is very good agreement between the predicted results and the observed experimental results. Nucleation will occur at orientations that are approximately randomly distributed. There is no driving force for rotation so a superconductor grain will retain the orientation of its nucleus. Growth will be favored within the a-b plane of each grain resulting in plate-like grains with a wide variety of orientations. Coarsening of the grains will occur. Thus, plate-like grains which have a wide variety of orientations and an average size which increases according to

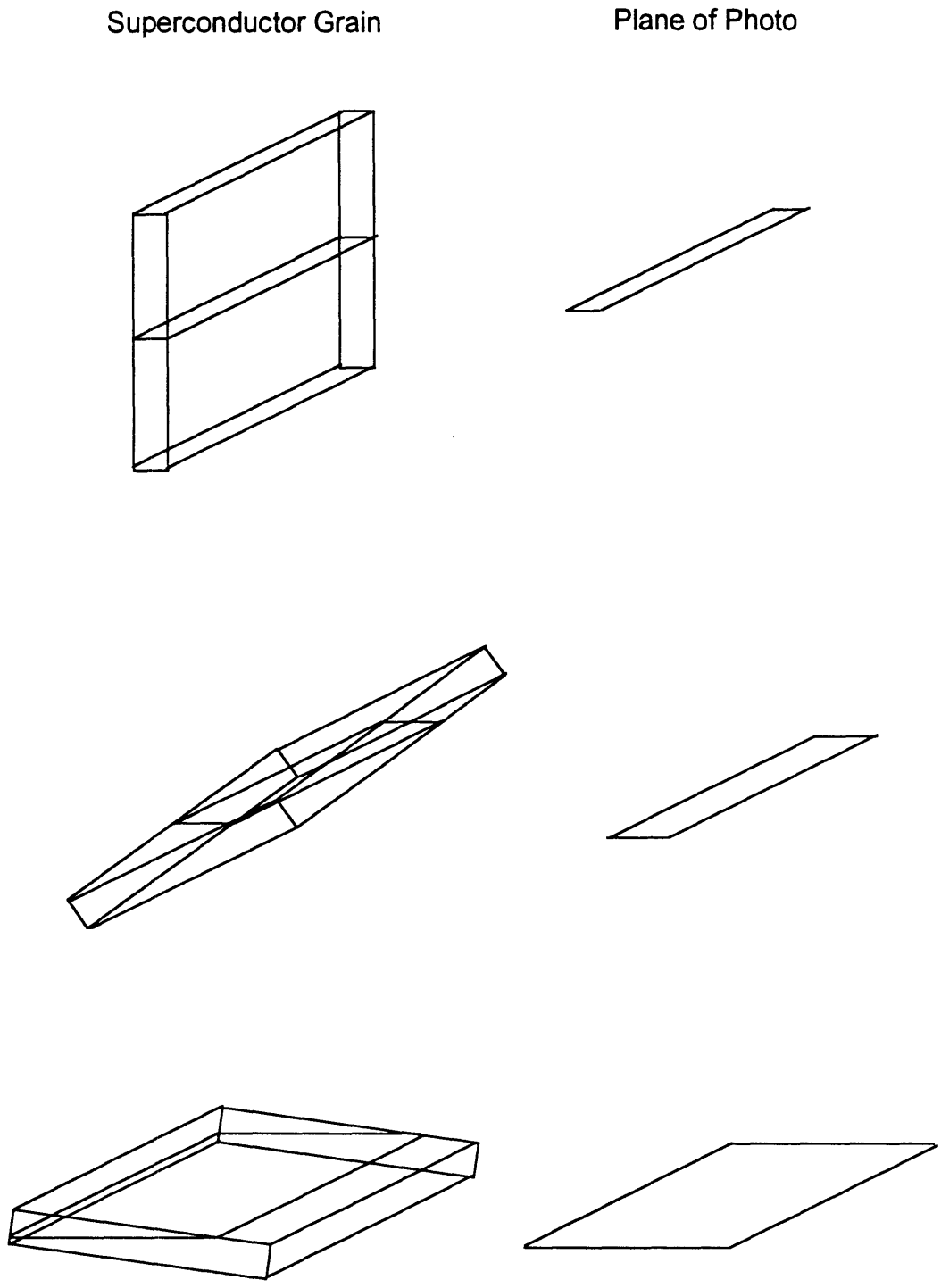

Figure 4-12. Schematic illustration of 2-D appearance of 3-D intersections of the plane of a photograph and superconductor grains of different orientations.

coarsening predictions are expected. This agrees very well with the results which were seen experimentally.

Since it has been shown that the superconductor grains will maintain the random orientations of their nuclei, no preferential alignment will occur as a result of processing in a temperature gradient. Similarly, since it has been shown to be energetically favorable for grains to grow as plates which extend in the crystallographic a-b plane and not in the direction of travel, elongation of grains along the length of the ribbon will not occur. Thus, changing experimental conditions such as the temperature gradient, maximum temperature, and travel velocity is not expected to result in the desired changes in superconducting properties. The experimental results support this theory and show that Otto's model is not applicable to the current experimental conditions. Otto's model is only applicable when the new grains impinge on one another and fill the cross section of the sample resulting in the establishment of a growth front at T_g.

Both the experimental results and the theoretical analysis show that solid state thermal gradient processing alone will not result in improved electrical properties as a result of elongation or preferential alignment. The experiments were beneficial in providing an improved understanding of the effects of the different processing stages on the final microstructure. This improved understanding could be beneficial in designing future experiments.

For a discussion of the potential applications of solid state thermal gradient processing for producing texturing in other materials systems see Section 4.7. This section also includes a discussion on the potential ways of combining solid state thermal gradient processing with another processing method, such as mechanical deformation, to produce improved superconducting composite ribbons.

Section 4.5 Superconducting Properties

4.5.1 SQUID Measurements of Critical Transition Temperature

The critical transition temperatures (onset T_c) were found to be in the range of 86 to 90 K for various samples. This is within the expected range for the $Y_1Ba_2Cu_3O_{7-x}$ phase and provides further proof that the desired phase was formed during the high temperature transformation treatments and subsequent oxygenation. The temperature at which the transition is complete (resistance, R, is zero) cannot be determined from this information. A plot of R versus T would be required to determine this. It is impossible to produce this data because these samples, although containing superconducting material, are not capable of carrying a superconducting current. This inability to carry a supercurrent is due to a lack of a continuous superconducting path in the sample and is explained more completely in the next section.

4.5.2 Four Point Probe Measurement of Critical Current Density

Measurements of critical current density (J_c) were attempted at 77 K (submerged in liquid nitrogen) without a magnetic field being present. No critical currents were established. Some further J_c measurements were attempted at 4.2 K (submerged in liquid helium). Once again, no critical currents were found.

The fact that no supercurrent was found may be explained by examining the microstructure of the samples. In order for a supercurrent to exist, there must be a continuous path on which the supercurrent may travel throughout the sample. In these samples there is a large Ag content which greatly reduces the cross sectional area available for a supercurrent and decreases the likelihood of the superconductor grains being continuously interconnected. There are voids, cracks, and other non-superconducting phases such as barium cuprates present in these samples. All of these further interrupt the flow of a supercurrent. It is impossible for the current to cross these interruptions. Thus, in the sample as a whole, there is either no path available for a supercurrent, or the path has such a small cross section that the current it could support is too small to measure and is of no practical value.

Otto [67] reported critical current density values of 125 to 145 A/cm^2 for superconducting composite ribbons produced using a starting ribbon composition of $Yb_1Ba_2Cu_3Ag_3$. The Ag content is small enough that the oxide grains are in contact with other grains and they occupy a large enough cross

section of the ribbon that a supercurrent may be supported. In the current work, the starting ribbon composition of $Y_1Ba_2Cu_3Ag_{15}$ results in a much smaller volume fraction of oxide grains. Thus, a continuous supercurrent path either does not exist or occupies such a small fraction of the cross section that the resulting supercurrent is too small to measure.

Section 4.6 $Yb_1Ba_2Cu_3Ag_{16}$ Samples

The results of the few Yb16 samples that were tested may be evaluated by comparing them to Y15 samples which received similar treatments.

Sample Yb16-2 was treated like sample Y15-4 (No-Ox, 10°C/min to 900°C and hold for 3 hours). Sample Yb16-2 had an Ag band at the surface on 90% of the sample, unlike sample Y15-4 which showed no Ag band at the surface. This indicates that Ag nodules are more likely to form on the Yb16 samples. Sample Yb16-2 had much smaller oxide phase particles than sample Y15-4, but both cases had a high degree of connectivity. This indicates that coarsening occurs more slowly in the Yb16 samples than in the Y15 samples, but the mechanism is very similar.

Sample Yb16-3 was given treatment Ox-13 followed by TG fast with the coil to 870°C, hold 10 minutes and slowly cool in the furnace. Sample Yb16-4 was given this treatment followed by a 3 hour anneal at 850°C. Sample Yb16-3 shows the expected microstructure for the given treatment. It has a well

developed Ag band at the center of the ribbon, indicating that the oxidation was complete and the outward solute diffusion rate was the same order of magnitude as in the Y15 samples. There was also a band of Ag at the surface. This band was not continuous, however, indicating that the formation of a smooth Ag sheath on the surface was less likely to occur than in the Y15 samples. Sample Yb16-4 had an unusual microstructure for the treatment that it received. There was no sign of a central Ag band in this sample, and only a few regions of Ag on the surface which resembled nodules more than a continuous sheath.

The critical temperature was in the expected range (88 K for Yb16-4). This provides further confirmation that $Yb_1Ba_2Cu_3O_{7-x}$ was the superconducting oxide present in these samples. No supercurrent was established in these samples.

Section 4.7 Applicability to Other Materials Systems and Suggestions for Future Work

Much of the information learned from this work can be applied to other materials systems. This section contains a discussion of potential applications of this information to other materials and recommendations for future work. The discussion is divided into three distinct areas: the production of layered microstructures, solid state thermal gradient processing of non-superconducting materials, and superconducting composite materials.

4.7.1 Production of Layered Microstructures

It was shown in Section 4.1.1 that an initially homogeneous metallic precursor material could be oxidized so that a five layer microstructure resulted if certain conditions were met. A solute-free layer resulted at the center of the sample due to outward diffusion of the solute during internal oxidation. Nodules of the noble metal, which eventually became a continuous layer, formed during internal oxidation in order to relieve the stress due to the volume change upon oxidation. This results in the formation of layers of noble metal at both surfaces and the center of the material while the intermittent layers consist of both the noble metal and the oxide phases. It should be possible to predict similar behavior in other materials systems. This process has potential usefulness as a processing method for other materials applications in which layers are important.

One area of recommended future work is the determination of the applicability of this process for producing layered structures of commercial importance such as multilayer capacitors. The traditional method of producing barium titanate multilayer capacitors involves firing $BaCO_3$ and TiO_2 at temperatures of 1100-1200°C to form $BaTiO_3$ powders [81-83]. More recently, wet chemical preparation methods have been used to produce barium titanate powders [81-83]. The method of oxidizing a metallic precursor has the potential to eliminate the necessity of producing oxide powders by proceeding directly to a structure having alternating layers of noble metal and oxide/noble metal.

4.7.2 Solid State Thermal Gradient Processing in Non-Superconducting Materials

Solid state thermal gradient processing has potential for producing texturing in many materials systems. SSTGP may be beneficial to any system in which a thermally activated solid state phase transition occurs. Otto's model provides a way of predicting the aspect ratio of grains associated with the formation of an isotropic phase that completely fills the cross section of the sample. The theory developed here explains what will occur when the new phase transforms such that each new grain is effectively isolated from the other new grains.

Recommendations for future work include applying solid state thermal gradient processing to other materials systems in an attempt to verify the predictions of aspect ratio given in Otto's model. The use of a materials system that is much simpler than for the superconducting composites is recommended for this work.

Theoretic modeling of the intermediate case between that of Otto's model (complete impingement) and the case treated in this work (no impingement) would also be helpful in defining the limiting conditions for the application of SSTGP. Theoretical modeling can also be done for the case of anisotropic growth when the new phase fills the cross section of the sample (no noble metal present). In this case, the aspect ratios of the new grains will have a range of predicted values and an average that is greater than in the case of isotropic growth (Otto model).

4.7.3 Superconducting Composite Materials

In the future, solid state thermal gradient processing of superconductors would be most useful when there could be a benefit to the superconducting properties of the material. Improved properties as a result of elongation or preferential alignment will not occur when a metallic precursor containing a large amount of noble metal is used during SSTGP, as in the current experiments. When there is little or no noble metal present, there may benefits due to elongation. When there is a large amount of noble metal present, it prevents the superconducting grains from impinging on one another. When the Ag phase does not prevent impingement from occurring and effectively isolate each grain, the conditions will be closer to those treated by Otto. However, the effect of the anisotropic growth rate on surface energy considerations will still need to be considered.

There may be ways to use solid state thermal gradient processing in conjunction with another process to result in a final material with improved properties. For example, deformation processing might be used to preferentially align nuclei or small grains of superconductor along the length of a sample. If the noble metal content of the material is small enough that the superconductors will impinge on one another during growth, then solid state thermal gradient processing could be used as a potential way of elongating the superconductor grains along the length of the ribbon. The strain which is placed on the material during deformation encourages elongation during solid state thermal gradient

processing as in strain annealing and directional recrystallization. This elongation would maintain the favorable orientation of the grains with their c-axis perpendicular to the length of the ribbon. This combined use of deformation processing and solid state thermal gradient processing has the potential to produce superconductors that are better than those produced by either method alone; it combines the benefits of preferential alignment from the deformation processing with the benefits of elongation from the thermal gradient processing. A supercurrent passing through a material with this preferential alignment and elongation experiences the increased critical current density found in the basal plane and decreased problems caused by grain boundaries, especially grain boundaries having a large misorientation angle.

Unlike the use of deformation, the use of an applied magnetic field is less likely to be benefit from combined use with solid state thermal gradient processing. Preferential alignment of grains in an applied magnetic field does not occur until the grains have grown to a size large enough that the energy required to rotate the grains is less than the energy of the magnetic misalignment. It is impossible to use this method to align small grains. The potential benefits of elongation due to additional processing in a thermal gradient are reduced because most of the material has already been transformed to the superconducting phase.

Recommendations for future work include determining whether or not the predicted benefits of combining mechanical deformation and SSTGP are seen experimentally. Specific experiments would involve starting materials of $Y_1Ba_2Cu_3Ag_{15}$ and a material with a lower Ag content such as $Y_1Ba_2Cu_3Ag_3$. These ribbons should be oxidized fully, heated in a traditional furnace until small elongated grains of superconducting oxide begin to form, and cooled rapidly. The ribbons should be mechanically deformed to align the small superconductor grains. The ribbons should then be processed in the temperature gradient to allow elongation to occur during complete transformation to the superconducting oxide.

Most of the knowledge gained about processing Y-Ba-Cu-O superconductors in a temperature gradient is applicable to other superconductor systems. The few experiments that were done with $Yb_1Ba_2Cu_3Ag_{16}$ precursors indicate that processing samples in the Yb-Ba-Cu-O superconductors is very similar to the Y-Ba-Cu-O system. Thus, the suggestions for future experiments are also applicable to the Yb materials. The most promising use of solid state thermal gradient processing for producing superconducting composites with improved properties is thought to be the combination of thermal gradient processing and another processing method. For example, mechanical deformation could be used to preferentially align nuclei or small oxide grains which are then elongated by solid state thermal gradient processing. This would work best in a material with only a moderate amount of noble metal present. There must be sufficient

noble metal present to gain the benefits of improved ductility and ease of making electrical contact. There should not be so much noble metal present that it prevents impingement of the oxide grains. Impingement of the oxide grains is necessary in order to force the grains to grow along the length of the ribbon. Also, too much noble metal will make it very difficult for the material to find a path on which to carry a supercurrent.

The Bi-Sr-Ca-Cu-O (BiSCCO) system is expected to behave similarly to the Y-Ba-Cu-O system. There is an anisotropic growth rate which results in plate like $Bi_2Sr_2Ca_2Cu_3O_y$ grains forming [76]. Thus, all of the anisotropic growth rate considerations that were discussed in Section 4.4.3.2 are applicable to the BiSCCO system. When a Bi-Sr-Ca-Cu-Ag metallic precursor is used, the same multi-phase considerations are encountered as in the YBCO systems. There are complications due to the presence of many different elemental oxides and the presence of the noble metal. Thus, solid state thermal gradient processing alone is not expected to result in significant elongation or preferential alignment of the superconducting oxide grains along the length of composite ribbons. In cases where the amount of noble metal present is small enough that impingement of the oxide grains will occur, there may be some elongation of grains along the length of the ribbon during solid state thermal gradient processing. In order to get improved superconducting properties due to preferential alignment, it will be necessary to combine solid state thermal

gradient processing with another processing method such as mechanical deformation.

Chapter 5. Conclusion

$Y_1Ba_2Cu_3Ag_{15}$ metallic precursor ribbons were oxidized to form the elemental oxides Y_2O_3, BaO, and CuO in Ag. The elemental oxides were formed by the method of internal oxidation. The best agreement between the predicted oxidation zone thickness and the experimentally determined oxidation zone thickness was found using a diffusivity constant for O in Ag of 1.2×10^{-6} cm^2/s from Kontoulis and Steele [34] and a solubility value for O in Ag of 1.3×10^{-5} from Sandhage [27]. Complete oxidation was achieved by heating the samples in flowing oxygen 5°C/min to 140°C, 0.5°C/min to 420°C, and holding for 13 hours. Ag nodules form at the surface during the oxidation process to relieve the stress due to the volume change. An Ag band forms at the center of the sample as a result of the outward solute diffusion in a sample that is completely oxidized. This formation of a five layer microstructure form an initially homogeneous metallic precursor is reproducible. This method of forming a layered structure has potential applications in many other materials systems.

The high temperature transformation treatments (e.g. 10°C/min to 900°C) resulted in transforming the elemental oxides to $Y_1Ba_2Cu_3O_{7-x}$. During the high temperature transformation treatment, the Ag nodules which formed on the surface during the oxidation treatment spread out to become a surface band of Ag. Coarsening results in an increase in the average oxide particle size and a

thickening of the Ag bands as the hold time increases at temperatures in the range of 890°C to 900°C.

After oxygenation at 500°C in flowing oxygen, the superconducting properties of the composite $Y_1Ba_2Cu_3O_{7-X}$/Ag ribbons were tested. The samples were found to contain superconducting $Y_1Ba_2Cu_3O_{7-x}$. The T_c was determined by SQUID analysis to be in the range of 86 K to 90 K for various samples. The samples were found to be unable to support a supercurrent at either 77 K or 4.2 K. This was attributed to the lack of a continuous supercurrent path due to the presence of cracks, voids, Ag grains, and other non-superconducting phases such as barium cuprates.

The use of solid state thermal gradient processing during the high temperature transformation treatment was examined experimentally and theoretically. This is the first time that thermal gradient experiments were done in the Y-Ba-Cu-O system. It is also the first systematic examination of the use of a thermally activated phase transition for producing microstructural changes in the presence of a temperature gradient.

A new model for solid state thermal gradient processing resulted from the theoretical examination. Nucleation will occur at orientations that are approximately randomly distributed in the presence of the temperature gradient just as in the isothermal case. The temperature gradient does not provide a driving force for rotation as in mechanical deformation or the application of a

magnetic field. Thus, a superconductor grain will maintain the orientation of its nucleus. Anisotropic growth favors the formation of plate-like grains which extend in the a-b plane. Surface energy considerations show that growth will occur perpendicular to the c-axis; the c-axis may or may not be perpendicular to the traveling direction. Thus, plate-like grains are expected to form having a wide variety of orientations and an average size that increases according to coarsening predictions. The theoretical predictions agree very well with the experimental results. Thus, solid state thermal gradient processing alone is not likely to result in either elongation of superconductor grains along the length of the ribbon or preferential alignment. However, enough has been learned about the process of solid state thermal gradient processing to predict that the combination of mechanical deformation and solid state thermal gradient processing will result in superconducting composites with improved superconducting properties. The understanding of solid state thermal gradient processing that was gained can be applied to the production of elongation and texturing in many other materials systems including other superconducting composites and non-superconducting materials systems.

Appendix 1. Otto Model for Thermal Gradient Processing with Isotropic Growth

The information contained in this appendix is taken largely from an unpublished manuscript of Otto [66]. The aspect ratio resulting from a thermally activated transformation that takes place in a temperature gradient will be calculated as a function of process variables and nucleation and growth parameters. Section A1.5 relates the model to the content of this thesis.

Section A1.1 The Fundamental Model

Consider the case of a rod of α, having unit area, traveling up a temperature gradient at a velocity, v. A thermally activated transformation occurs from α to β. The rod is divided into consecutive segments of length D (see Figure A1-1). As each segment reaches a temperature sufficient for nucleation to occur, T_n, nuclei are formed. The grains expand to fill the cross-section of the rod. The grains grow along the length of the rod to the point at which the decreasing temperature slows the growth rate to equal the traveling velocity. The temperature at this growth front is T_g.

If $T_n > T_g$, then at steady state no new nucleation may occur and the grains extend to the end of the rod (see Figure A1-2). However, if $T_n < T_g$, new nuclei may form. These nuclei become grains that embed in the α/β interface at T_g (see Figure A1-3). The total area fraction of new β grains formed in a segment

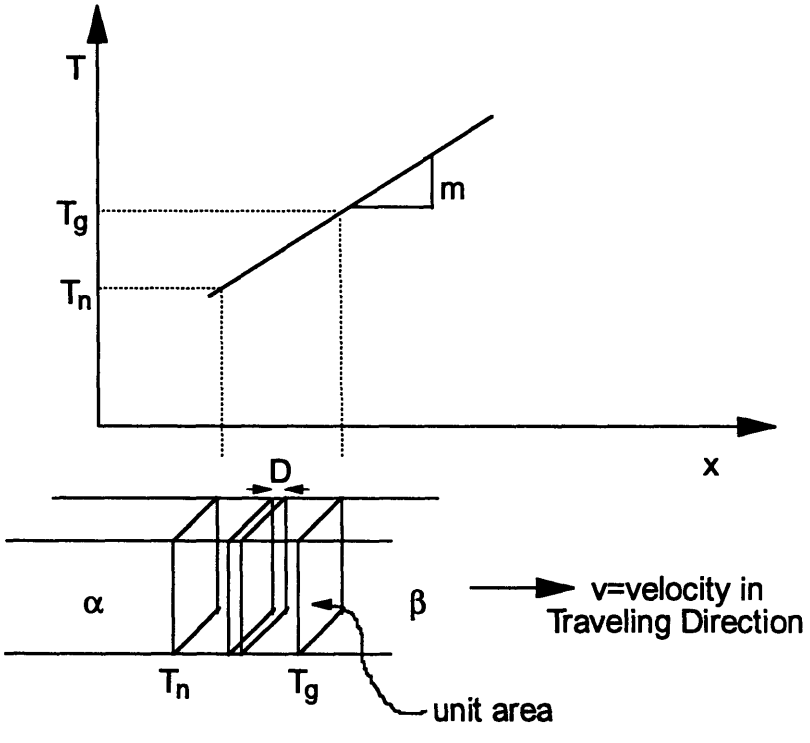

Figure A1-1. Schematic of SSTGP as treated by Otto model.

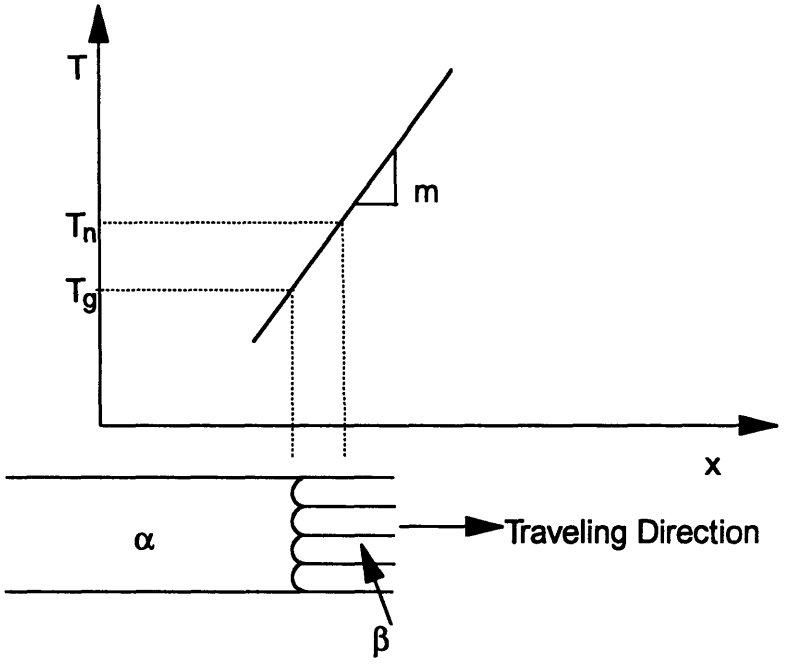

Figure A1-2. Steady state SSTGP with no new nucleation ($T_g < T_n$).

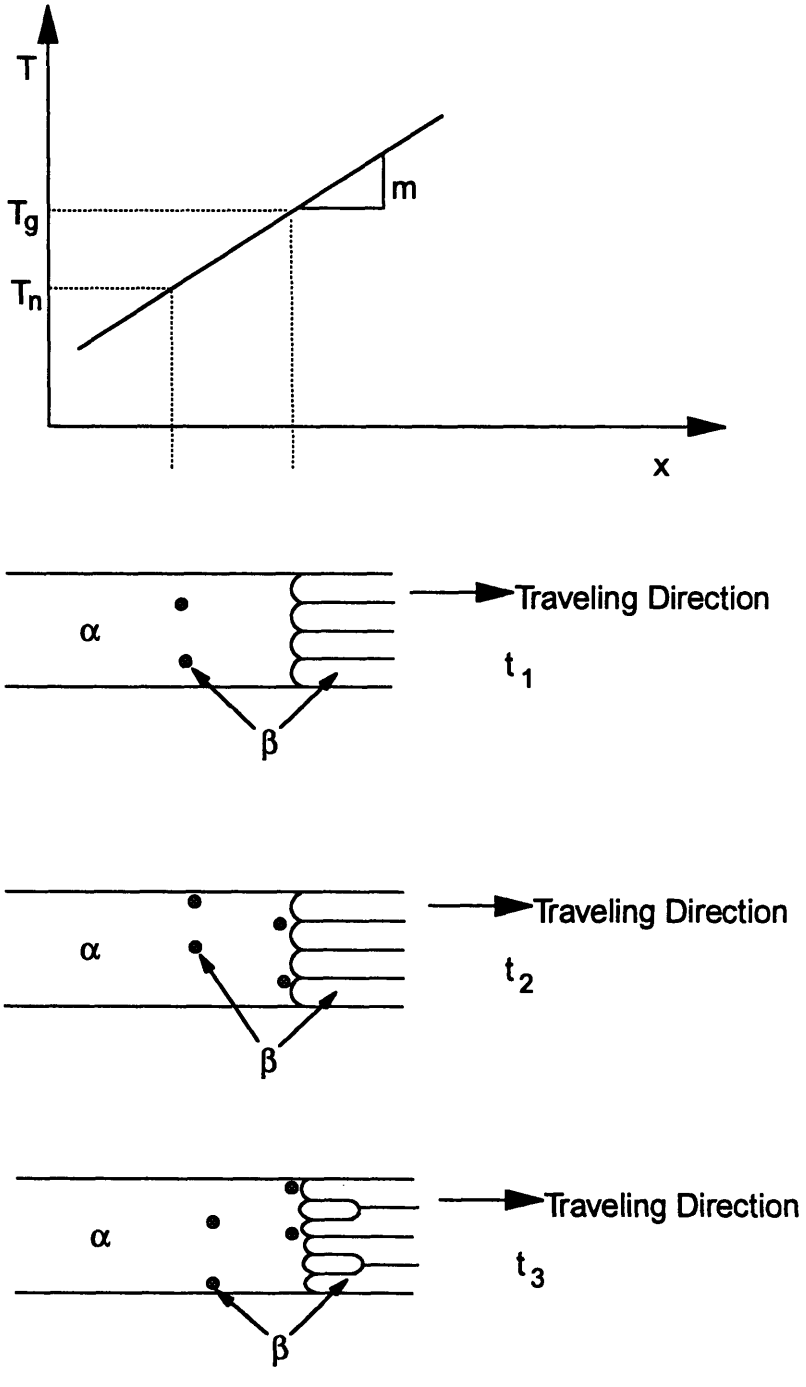

Figure A1-3. Schematic showing how new grains embed in the interface at T_g.

of length D projected onto the α/β interface is F. The average number of segments per grain is N. The average radius of a grain is r_a. Thus, the aspect ratio is

$$\Phi = \frac{ND}{2r_a} \tag{A1-1}$$

In order to maintain the validity of the two-dimensional approximation of nucleation and growth which applies when $F << 0.5$, the average repeating length of a segment has a maximum of $2r_a$. Thus,

$$D = 2r_a \tag{A1-2}$$

and

$$\Phi = N \tag{A1-3}$$

Section A1.2 Calculating N in Terms of F

If A_n is the area fraction occluded at T_g by randomly distributed β grains in n consecutive D lengths and P is the probability that a site is occluded, then $P = A_n$ and the most probable value [84] of n, N, is given by

$$\int_{n=0}^{n=N} \left(\frac{\partial P}{\partial n} = \frac{\partial A}{\partial n}\right) dn = 0. \tag{A1-4}$$

The most probable number of D lengths required for occlusion of a site at T_g must account for occlusion of already occluded sites. Consider n segments arriving consecutively at an initially unoccluded α/β interface at T_g. The

probability of occluding an as-yet unoccluded site by a segment following (n-1) segments is given by

$$\Delta P_n = \Delta A_n = F(1 - A_{n-1}) = F\left(1 - \sum_{i=1}^{n-1} \Delta A_i\right) \quad \text{(A1-5)}$$

where ΔA_n is the change in total occluded area per incoming nth segment following (n-1) segments. A_{n-1} is the area occluded by (n-1) prior segments:

$$A_{n-1} = A_n - F(1 - A_{n-1}) = \sum_{i=1}^{n-1} \Delta A_i = \frac{A_n}{1-F} - \frac{F}{1-F} \quad \text{(A1-6)}$$

Substituting equation A1-6 and

$$\Delta A_n = \left(\frac{dA_n}{dn}\right)_{n \in i} \quad \text{(A1-7)}$$

into equation A1-5 and integrating yields

$$\int_0^A \frac{dA}{(1-A)} = \int_0^n \frac{F}{(1-F)} dn \quad \text{(A1-8)}$$

$$A = 1 - \exp\left(\frac{F_n}{F-1}\right) \quad \text{(A1-9)}$$

Thus, for the most probable number of D lengths, N is calculated in terms of F for the general case as

$$N = \frac{0.693}{F} - 0.693 \quad \text{(A1-10)}$$

and for the case of very small F as

$$N = \frac{0.693}{F} \quad \text{(A1-11)}$$

When the two dimensional approximation is valid

$$\Phi = \frac{0.693}{F} \qquad \text{(A1-12)}$$

Section A1.3 Calculating F in Terms of Nucleation and Growth Parameters That Depend Exponentially on Temperature

The Arrhenius nucleation and growth rates are approximated as exponentially increasing with respect to temperature such that

$$I_v = B_n \exp(\frac{-E_n}{kT}) \qquad \text{(A1-13)}$$

and

$$R = B_r \exp(\frac{-E_r}{kT}) \qquad \text{(A1-14)}$$

where k is Boltzmann's constant, B_n and B_r are constants, and E_n and E_r are activation energies for nucleation and growth, respectively. The two-dimensional nucleation rate, I, is given by

$$I = I_v D = 2r_a I_v \qquad \text{(A1-15)}$$

when $D = 2r_a$ and $F << 0.5$.

If the rate yielded by the Arrhenius equation at a particular temperature, T*, is multiplied by exp(q(T*-T)) in the approximating equation, then the equations' values match at $T^* = T_g$. Their temperature dependencies diverge gradually as the temperature decreases below T_g. By definition $v = R(T_g)$, so equation A1-13 yields

$$T_g = \frac{-E_r}{k \ln\left(\frac{v}{B_r}\right)} \qquad \text{(A1-16)}$$

Using the substitutions

$$\frac{E}{kT} = \frac{ET_g}{kT_gT} \tag{A1-17}$$

and

$$\frac{T_g}{T} = \frac{T_g - T}{T} + 1 \approx \frac{T_g - T}{T_g} + 1 = \frac{\Delta T}{T_g} + 1 \tag{A1-18}$$

in equations A1-13 and A1-14 yields

$$I_v \approx I_v^e = B_n \exp\left(\frac{-E_n}{kT_g}\right) \exp\left(\frac{-E_n \Delta T}{kT_g^2}\right) \tag{A1-19}$$

$$R \approx R^e = B_r \exp\left(\frac{-E_r}{kT_g}\right) \exp\left(\frac{-E_r \Delta T}{kT_g^2}\right) \tag{A1-20}$$

where R^e and I^e are the exponential approximations. If $T_g > T$, then $R^e > R$ and $I^e > I$.

Substituting the dimensionless parameters

$$\gamma = \frac{E_r}{kT_g} \tag{A1-21}$$

and

$$\phi = \frac{T_g - T}{T_g} \tag{A1-22}$$

reduces equations A1-13 and A1-20 to

$$R = B_r \exp\left(\frac{\gamma}{\phi - 1}\right) \tag{A1-23}$$

$$R^e = B_r \exp(-\gamma) \exp(-\gamma\phi) \tag{A1-24}$$

If the maximum acceptable error between the Arrhenius form and the exponential approximation is ε then the lowest acceptable temperature limit of the approximation is found using

$$\left|\frac{R-R^e}{R}\right| = \exp\left(\frac{-\gamma\phi^2}{\phi-1}\right) - 1 \leq \varepsilon \qquad \text{(A1-25)}$$

A similar analysis for the nucleation rate can also be used. The temperature limit, T_n, where nucleation is negligible must equal or exceed the lower limit from both error criteria.

Assuming the temperature increase is linear between T_n and T_g, let m be the temperature gradient. With the time axis shifted so that t = 0 at T_g and

$$\frac{-\theta}{m} \leq t \leq 0 \qquad \text{(A1-26)}$$

where

$$\theta = T_g - T_n, \qquad \text{(A1-27)}$$

$$T_g - T(t) = -mvt = \Delta T \qquad \text{(A1-28)}$$

Substituting into equations A1-19 and A1-20 yields

$$I_v^e = B_n a_n \exp(b_n mvt) \qquad \text{(A1-29)}$$

$$R^e = B_r a_r \exp(b_r mvt) \qquad \text{(A1-30)}$$

where

$$a_n = \exp\left(\frac{-E_n}{kT_g}\right) \qquad \text{(A1-31)}$$

$$a_r = \exp\left(\frac{-E_r}{kT_g}\right) \tag{A1-32}$$

$$b_n = \frac{E_n}{kT_g^2} \tag{A1-33}$$

and

$$b_r = \frac{E_r}{kT_g^2} \tag{A1-34}$$

The differential volume fraction of β formed is defined with respect to two identical time coordinates, t and τ, as shown in Figure A1-4. Both nucleation and growth impingement can be ignored without significant error because small F values yield aspected structures.

In two dimensions, the number of nuclei formed at τ over dτ is $dI_\tau = I_\tau d\tau$. The nuclei grow over time t - τ. At time t, the nuclei interfaces travel dr_t normal to the local interface lines in two dimensions. If $\lambda_{t/\tau}$ is the interface length at t of the grains formed at τ over dτ without impingement, then the area fraction, $d^2F_{t/\tau}$, of β formed at t by growth dr_t of the nuclei formed at τ over dτ is

$$d^2F_{t/\tau} = I_\tau d\tau_\tau \lambda_{t/\tau} dr_t \tag{A1-35}$$

Substituting $\lambda_{t/\tau} = 2\pi r_{t/\tau}$ for round grains and equation A1-15 for two dimensional nucleation and integrating from $r_{t/\tau} = 0$ at τ to $r_{t/\tau}$ at t yields

$$dF_{t/\tau} = \pi I_{v\tau} r_{t/\tau}^2 d\tau \tag{A1-36}$$

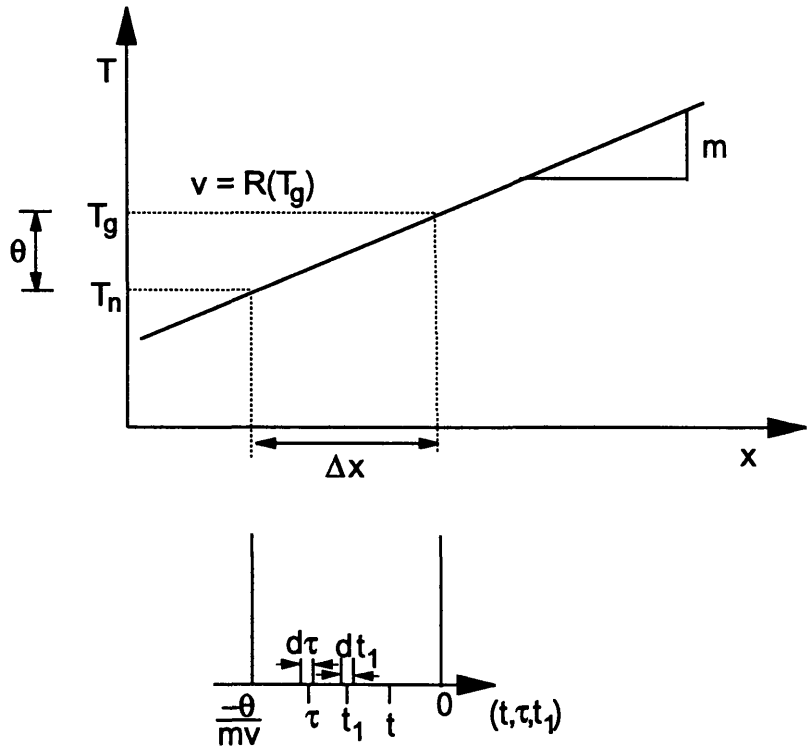

Figure A1-4. Time axis for exponential approximation in Otto model.

The radius at t due to nucleation at τ and growth over $t_1 = t - \tau$ with $R = f(t_1)$ is obtained by expanding $dr_{t/\tau}$ to include time variation. Substituting into equation A1-30 and integrating yields

$$\int_0^{r_{t/\tau}} dr = \int_{t_1=\tau}^{t} \left(\frac{\partial r}{\partial t_1}\right) dt_1 = B_r a_r \int_{t_1=\tau}^{t} [\exp(b_r m v t_1)] dt_1 \qquad \text{(A1-37)}$$

$$r_{t/\tau} = \frac{B_r a_r}{b_r m v}[\exp(b_r m v t) - \exp(b_r m v \tau)] \qquad \text{(A1-38)}$$

Substituting equations A1-30 and A1-38 into equation A1-36 yields

$$\int_0^F dF_{t/\tau} = Q \int_{\tau=\frac{-\Delta T}{mv}}^{0} \left\{e^{mv(2b_r t + b_n \tau)} - 2e^{mv[b_r t + (b_n + b_r)]\tau} + e^{mv(2b_r + b_n)\tau}\right\} d\tau \qquad \text{(A1-39)}$$

where

$$Q = \pi D B_n a_n \left(\frac{B_r a_r}{b_r m v}\right)^2 \qquad \text{(A1-40)}$$

Substituting equation A1-40 for Q and $D = 2r_a$ where $\Delta T \Rightarrow \theta$ yields

$$F = \frac{2\pi r_a B_n a_n (B_r a_r)^2}{b_r^2 (mv)^3}\left\langle \frac{1}{b_n}\left[e^{-2b_r\theta} - e^{-(b_n+2b_r)\theta}\right] - \frac{2}{b_n + b_r}\left[e^{-b_r\theta} - e^{-(b_n+2b_r)\theta}\right] + \frac{1}{b_n + 2b_r}\left[1 - e^{-(b_n+2b_r)\theta}\right]\right\rangle \qquad \text{(A1-41)}$$

If I_r is the number of nuclei formed on a cross section, then

$$r_a = \left(\frac{F}{\pi I_r}\right)^{\frac{1}{2}} \qquad \text{(A1-42)}$$

I_r is obtained by integrating the amount of nuclei formed in a segment over dt.

$$I_r = 2r_a B_n a_n \int_{t=\frac{-\theta}{mv}}^{0} e^{b_n m v t} dt = \frac{2r_a B_n a_n}{b_n m v}\left(1 - e^{-b_n\theta}\right) \qquad \text{(A1-43)}$$

Substituting into equation A1-42 and solving for r_a yields

$$r_a = \left[\frac{F}{\frac{2\pi B_n a_n}{b_n m v}(1-e^{-b_n\theta})} \right]^{\frac{1}{3}} = \left[\frac{FE_n mv}{2\pi k T_g^2 B_n e^{\frac{-E_n}{kT_r}} \left(1-e^{\frac{-E_n\theta}{kT_g^2}} \right)} \right]^{\frac{1}{3}} \qquad \text{(A1-44)}$$

Substituting into equation A1-41 and solving for F yields

$$F = \frac{2\pi B_n B_r^3 E_n^{\frac{1}{2}} T_g^8 k^4 e^{\left[\frac{-(E_n+3E_r)}{kT_g}\right]}}{E_r^3 (mv)^4 \left[1-e^{\left(\frac{-E_n\theta}{kT_g^2}\right)} \right]^{\frac{1}{2}}} \left\langle \frac{1}{E_n} \left[e^{\frac{-2E_r\theta}{kT_g^2}} - e^{\frac{-(E_n+2E_r)\theta}{kT_g^2}} \right] - \frac{2}{E_n+E_r} \left[e^{\frac{-E_r\theta}{kT_g^2}} - e^{\frac{-(E_n+2E_r)\theta}{kT_g^2}} \right] \right.$$

$$\left. + \frac{1}{E_n+2E_r} \left[1 - e^{\frac{-(E_n+2E_r)\theta}{kT_g^2}} \right] \right\rangle^{\frac{3}{2}} \qquad \text{(A1-45)}$$

The exponential terms in equation A1-45 are typically much less than one.

Therefore,

$$F = \frac{2\pi B_n B_r^3 E_n^{\frac{1}{2}} T_r^{\frac{13}{2}} R_g^4 \exp\left(\frac{-(E_n+E}{R_g T_r}\right.}{E_r^3 (mv)^4 (E_n+2E_r)^{\frac{3}{2}}} \qquad \text{(A1-46)}$$

If $E_n = E_r$, then

$$F = \frac{1.21 B_n B_r^3 T_g^8 k^4 \exp\left(\frac{-4E_r}{kT_g}\right)}{E_r^4 m^4 v^4} \qquad \text{(A1-47)}$$

Section A1.4 Calculation of Aspect Ratio

Substitution of equation A1-47 into equation A1-12 yields

$$\Phi = \frac{0.573 E_r^4 m^4 v^4 \exp\left(\frac{4E_r}{kT_g}\right)}{B_n B_r^3 T_g^8 k^4} \qquad \text{(A1-48)}$$

In equation A1-48, it appears that the aspect ratio has a fourth power dependence on both the temperature gradient, m, and the velocity, v. However, the velocity must match the growth rate at T_g. If v increases, T_g will also increase. The T_g^8 term overpowers the exponential and v^4 terms. An increase in velocity actually reduces elongation. There is a fourth power dependence on the temperature gradient.

Section A1.5 Relationship of Model to Main Body of Thesis

At the time that this experimental plan was developed, Otto's model was the best model available for predicting the effect of solid state thermal gradient processing. According to Otto's approximation, the aspect ratio resulting from solid state thermal gradient processing may be predicted using

$$\Phi = \frac{0.573E_r^4 m^4 v^4 \exp\left(\frac{4E_r}{kT_g}\right)}{B_n B_r^3 T_g^8 k^4}$$

where m is the temperature gradient, v is the traveling velocity, E_r and $E_n = E_r$ are the activation energies of growth and nucleation, respectively, T_g is the temperature where the growth rate equals the traveling velocity, k is Boltzmann's constant, and B_n and B_r are constants in the exponential approximations for nucleation and growth, respectively.

There is an apparent fourth power dependence of the aspect ratio on the temperature gradient and the velocity. The fourth power dependence on the temperature gradient is correct. However, when v increases, T_g will also

increase which results in the aspect ratio decreasing. This makes sense when one considers the extreme cases of very fast or very slow velocities. A very fast velocity is equivalent to loading a sample into a preheated isothermal furnace. No elongation would be expected in this case. A very slow velocity will result in T_g being less than T_n and nucleation will be prevented. In this case, the grains will extend the length of the sample. Thus, a fast velocity results in small elongation and a slow velocity results in large elongation.

In the case of solid state thermal gradient processing of metallic precursor ribbons to form superconducting oxides, elongation of the superconductor grains along the length of the ribbon was expected to improve the superconducting properties. The reduction in the number of grain boundaries that a supercurrent would have to cross in order to travel the length of the ribbon would improve the critical current density.

Otto's model, however, does not consider the effect of the presence of a noble metal, a multi-phase material, or anisotropic growth, all of which are present in the transformation to form $Y_1Ba_2Cu_3O_{7-x}$/Ag composite ribbons. It was shown in Section 4.4.3.1 that growth will not occur according to Otto's model when there is a large amount of noble metal present. Otto's model depends on the impingement of the growing grains and the maintenance of a growth front at T_g. Neither of these conditions applies to the experimental case encountered in producing the $Y_1Ba_2Cu_3O_{7-x}$/Ag composite ribbons. It was shown in Section

4.4.3.2 that the anisotropic growth of the superconductor grains will result in the vast majority of grains growing perpendicular to the c-axis direction. This c-axis direction may or may not be perpendicular to the traveling direction.

Thus, Otto's model was not found to be applicable to the experiments where $Y_1Ba_2Cu_3Ag_{15}$ precursor ribbons are oxidized and then transformed in a temperature gradient to form $Y_1Ba_2Cu_3O_{7-x}$/Ag composite ribbons. Otto's model will be applicable for solid state thermal gradient processing in many other material systems when the additional complications of the noble metal, the multi-phase material, and anisotropic growth are not present. There may also be cases in which deformation processing and solid state thermal gradient processing may be combined to result in improved superconducting properties due to elongation and preferential alignment along the length of the ribbon. Possible future applications such as this were discussed in Section 4.4.4.

References

1. J.G. Bednorz and K.A. Muller: "Possible High T_c Superconductivity in the Ba-La-Cu-O System," Z. Phys. B - Cond. Matter 64 (1986) p. 189-193.

2. G.J. Yurek, J.B. Vander Sande, W.-X. Wang, D.A. Rudman, Y. Zhang, and M.M. Mathiesen: "Synthesis of a Superconducting Oxide by Oxidation of a Metallic Precursor," Met. Trans. A 18A (1987) p. 1813-1817.

3. G.J. Yurek, J.B. Vander Sande, W.-X. Wang, and D.A. Rudman: "Direct Synthesis of a Metal/Superconducting Oxide Composite by Oxidation of a Metallic Precursor," J. Electrochem. Soc. (Oct. 1987) p. 2635-2636.

4. G.J. Yurek, J.B. Vander Sande, D.A. Rudman, and Y.-M. Chiang: "Superconducting Microcomposites by Oxidation of Metallic Precursors," JOM (Jan. 1988) p. 16-18.

5. G.J. Yurek, J.B. Vander Sande, and D.A. Rudman: "Synthesis of Superconducting Oxides and Oxide/Metal Composites by Oxidation of Metallic Precursors," Mat. Res. Symp. Proc. Vol. 99 (1988) p. 619-622.

6. H.K. Onnes: Commun. Phys. Lab. U. B. (1911) p. 119.

7. R.M. Hazen: The Breakthrough: The Race for the Superconductor, Summit Books, New York, 1988.

8. M.K. Wu, J.R. Ashburn, C.J. Torng, P.H. Hor, R.L. Meng, L. Gao, Z.J. Huang, Y.Q. Wang, and C.W. Chu: "Superconductivity at 93 K in a New Mixed-Phase Y-Ba-Cu-O Compound System at Ambient Pressure," Phys. Rev. Let. 58 (1987) p. 908.

9. J. Detjen: "New Type of Superconductors Found; Development Hailed by Scientists," Philadelphia Inquirer, Feb. 16, 1988, p. A2.

10. The Associated Press: "New Material Found for Superconductivity Report of Record Temperature Confirmed," San Jose Mercury News, March 2, 1988, p. 8A.

11. J. Narayan: "Microstructure and Properties of High-T_c Superconductors," JOM (Jan. 1989) p. 18-23.

12. P. Chaudhari, R.H. Koch, R.B. Laibowitz, T.R. McGuire, and R.J. Bambino: "Critical Current Measurements in Epitaxial Films of $YBa_2Cu_3O_{7-x}$ Compound," Phys. Rev. Let. 58 (1987) p. 2684.

13. D.M. Kroeger: "Grain Boundaries and J_c in High-T_c Oxide Superconductors," JOM 41 (1989) 1, p. 14-17.

14. J.C. Garland: "Granular Properties of High T_c Superconductors," Physica A 157 (1989) p. 111-119.

15. J.W. Ekin, A.I. Braginski, A.K. Panson, M.A. Janocko, D.W. Capone II, N.J. Zaluzec, B. Flandermeyer, O.F. de Lima, M. Hong, J. Kwo, and S.H. Liou: "Evidence for Weak Link and Anisotropy Limitations on the Transport Critical Current in Bulk Polycrystalline $Y_1Ba_2Cu_3O_x$," J. Appl. Phys. 62 (1987) 12, p. 4821-4828.

16. S.S. Kim, T.T. Srinivasan, and R.E. Newnham: "Weak-Link Nature of AC Susceptibility in the Grain Oriented $YBa_2Cu_3O_{7-\delta}$ Superconducting Ceramics," Phys. Stat. Sol. A 123 (1991) p. 275-283.

17. J.R. Clem: "Granular and Superconducting-Glass Properties of the High-Temperature Superconductors," Physica C 153-155 (1988) p. 50-55.

18. D. Dimos, P. Chaudhari, J. Mannhart, and F.K. LeGoues: "Orientation Dependence of Grain-Boundary Critical Currents in $YBa_2Cu_3O_{7-\delta}$ Bicrystals," Phys. Rev. Let. 61 (1988) 2, p. 219-222.

19. Y. Hidaka, Y. Enomoto, M. Suzuki, M. Oda, and T. Murakami: "Anisotropic Properties of Superconducting Single-Crystal $(La_{1-x}Sr_x)_2CuO_4$," Jpn. J. Appl. Phys. 26 (1987) p. L377-L379.

20. T.R. Dinger, T.K. Worthington, W.J. Gallagher, and R.L. Sandstrom: "Direct Observation of Electronic Anisotropy in Single-Crystal $YBa_2Cu_3O_{7-\delta}$," Phys. Rev. Let. 58 (1987) 25, p. 2687-2690.

21. Y. Hidaka, Y. Enomoto, M. Suzuki, M. Oda, A. Katsui, and T. Murakami: "Anisotropy of the Upper Critical Magnetic Field in Single-Crystal $YBa_2Cu_3O_{7+y}$," Jpn. J. Appl. Phys. 26 (1987) 5, p. L726-L728.

22. K. Hayashi, K. Murata, K. Takahashi, M. Tokumoto, H. Ihara, M. Hirabayashi, N. Terasa, N. Koshizuka, and Y. Kimura: "Preparation and Characterization of Ba-Y-Cu-O Single Crystals," Jpn. J. Appl. Phys. 26 (1987) 7, p. L1240-1243.

23. T.K. Worthington, W.J. Gallagher, T.R. Dinger, and R.L. Sandstrom: "Anisotropy in Single-Crystal $YBa_2Cu_3O_{7-x}$," Novel Superconductivity, 1987, p. 781-785.

24. D.R. Clarke, T.M. Shaw, and D. Dimos: "Issues in the Processing of Cuprate Ceramic Superconductors," J. Am. Ceram. Soc. 72 (1989) 7, p. 1103-1113.

25. S. Jin, R.C. Sherwood, R.B. van Dover, T.H. Tiefel, and D.W. Johnson, Jr.: "High Tc Superconductors - Composite Wire Fabrication," Appl. Phys. Let. 51 (1987) p. 203-204.

26. T. Kogure, Y. Zhang, R. Levonmaa, R. Kontra, W.-X. Wang, D.A. Rudman, G.J. Yurek, and J.B. Vander Sande: "Grain Boundary Structure of $YbBa_2Cu_3O_{7-x}$ Formed by Oxidation of Metallic Precursors," Physica C 156 (1988) p. 707-716.

27. K.H. Sandhage: "The Preparation of Superconducting YBa2Cu3O7-y/Ag Microlaminates by an Oscillating Scheme," J. Electrochem. Soc. 139 (1992) 6, p. 1661-1671.

28. Y. Feng, D.C. Larbalestier, S.E. Babcock, and J.B. Vander Sande, "(001) Faceting and $Bi_2Sr_2CuO_{6+x}$ (T_c=7~22 K) Phase Formation at the Ag/Bi-Sr-Ca-Cu-O Interface in Ag-Clad $Bi_2Sr_2CaCu_2O_{8+x}$ (T_c=75~95 K) Superconducting Tapes," Appl. Phys. Let. 61 (1992) 10, p. 1-3.

29. C. Wagner, "Types of Reactions in the Oxidation of Alloys," Z. Elektrochem 63 (1959) 7, p. 772-790.

30. O. Kubaschewski and B.E. Hopkins: Oxidation of Metals and Alloys, Butterworth & Co. Ltd., London, 1962.

31. K.A. Gschneider, Jr.: "On the Valences of Europium and Ytterbium in Compounds," J. Less Com. Met. 17 (1969) p. 13-24.

32. T. Rosenqvist: Principles of Extractive Metallurgy, McGraw-Hill Book Co., New York, 1974.

33. A. Combe and J. Cabane: "Mechanism of Internal Oxidation in Silver Alloys," Oxid. of Metals 21 (1984) 1/2 p. 21-37.

34. I. Kontoulis and B.C.H. Steele: Solid State Ionics 47 (1991) 3-4, p. 317-24, in Diffusion & Defect Data, Solid State Data - Pt. A: Defect and Diffusion Forum A 86&87 (1992) p. 167.

35. M.G. Hall and C.W. Haworth: "Diffusion of Cu in Ag-Cu Alloys," Trans. Met. Soc. AIME 245 (1969) p. 2476-2478, in Diffusion Data 4 (1970) p. 10.

36. H.H. Podgurski and F.N. Davis: "The Solubility of Oxygen in Silver and the Thermodynamics of the Internal Oxidation of a Silver-Copper Alloy," Trans. AIME 230 (1964) p. 731-735.

37. W. Eichenauer and G. Muller: Z. Metallk. 53 (1962) p. 321.

38. V.M. Gryaznov, S.G. Guliyanova, and S. Kanizius: "Diffusion of Oxygen through a Silver Membrane," Zh. Fiz. Khim 47 (1973) 10, p. 2694-2696, in Diffusion and Defect Data 10 (1974) p. 3.

39. R. Mackert, Jr., R.D. Ringle, and C.W. Fairhurst: "High-Temperature Behavior of a Pd-Ag Alloy for Porcelain," Dental Res. 62 (1983) 12, p. 1229-1235.

40. S. Guruswamy, S.M. Park, J.P. Hirth, and R.A. Rapp: "Internal Oxidation of Ag-In Alloys: Stress Relief and the Influence of Imposed Strain," Oxid. of Metals 26 (1986) 1/2, p. 77-100.

41. B.J. Piearcey and F.L. Versnyder: "A Breakthrough in Making Turbine Components ... Directional Solidification and Single Crystals," Metal Prog. 90 (1966) 5, p. 66-71.

42. J.S. Haggerty, W.P. Menashi, and J.F. Wenckus: "Methods of Forming Refractory Fibers by Laser Energy," U.S. Patent 3,944,640 (Mar. 1976).

43. H.D. Brody, J.S. Haggerty, M.J. Cima, M.C. Flemings, R.L. Barns, M. Gyorgy, D.W. Johnson, W.W. Rhodes, W.A. Sunder, and R.A. Laudise: "Highly Textured and Single Crystal $Bi_2CaSr_2Cu_2O_x$ Prepared by Laser Heated Float Zone Crystallization," J. Crystal Growth (1989) p. 225-233.

44. X.P. Jiang, J.G. Huang, Y. Yu, M. Jiang, G.W. Qiao, Y.L. Ge, Z.Q. Hu, C.X. Shi, Y.H. Zhao, Y.J. Wang, G.Z. Xu, and Y.E. Zhou: "The Crystal Growth of Y-Ba-Cu-O by Laser Floating Zone Melting," Supercond. Sci. Tech. 1 (1988) p. 102-106.

45. T.J. Richardson and L.C. De Jonghe: "Traveling Solvent Zone Texturing of Ceramic Superconductor Thick Films," J. Mat. Sci. Let. 10 (1991) p. 369-370.

46. M.L. Kronberg and F.H. Wilson: "Secondary Recrystallization in Copper," Trans. AIME 185 (1949) p. 501.

47. W.G. Burgers and P.C. Louwerse: "Uber den Zusammenhang zwischen Deformationsvorgang und Rekristallisationstextur bei Aluminium," Zeits. f. Physik 67 (1931) p. 605-678.

48. C.S. Barrett: "Recrystallization Texture in Aluminum After Compression," Trans. AIME 137 (1940) p. 128-145.

49. A.E. van Arkel: "Quelques phenomes de recristallisation," Rev. d. Met. 33 (1936) p. 197.

50. P.A. Beck, P.R. Sperry, and H. Hu: "The Orientation Dependence of the Rate of Grain Boundary Migration," J. Appl. Phys. 21 (1950) p. 420-425.

51. J.M. Nell: "Multiphase Strengthening of Rapidly Solidified Nickel Base Superalloys," PhD Thesis, Massachusetts Institute of Technology (Feb. 1989).

52. R.L. Cairns, L.R. Curwick, and J.S. Benjamin: "Grain Growth in Dispersion Strengthened Superalloys by Moving Zone Heat Treatments," Met. Trans. A 6A (1975) p. 179-188.

53. J.M. Marsh and J.W. Martin: "Micromechanisms of Texture Development During Zone Annealing of MA 6000 Extrusions," Mat. Sci. and Tech. 7 (1991) p. 183-188.

54. Y. Ohba: "Secondary Recrystallization of Pure Molybdenum Wires," Acta Met. 34 (1986) 7, p. 1329-1334.

55. V.S. Postnikov, Y.M. Iyevlev, and A.D. Povalyayev: "Directional Recrystallization of Gold and Silver Films," Fiz. Metal. Metalloved. 42 (1976) 1 p. 208-210.

56. T. Kunugi, S. Oomori, and S. Mikami: "Preparation of Ultra-High Modulus Polyethylene Films by the Zone-Annealing Method," Polymer 29 (1988) p. 814-820.

57. G.K. Williamson and R.E. Smallman: "The Growth of Strain-Anneal Crystals of Predetermined Orientation," Acta Met. 1 (1953) p. 487-491.

58. D. Driver: "Near Net Shape Manufacture of Aero Engine Components," Metals and Materials 4 (1988) p. 493-497.

59. A.N. Christensen, S.E. Rasmussen, and G. Thirup: "Superconductivity of Some Transition Metal Compounds," J. Sol. State Chem. 34 (1980) p. 45-50.

60. A.N. Christensen and P. Roehammer: "The Crystal Growth of δ-VN by Floating Zone and Zone Annealing Techniques," J. Crystal Growth 38 (1977) p. 281-283.

61. R.E. Allen: "Directionally Recrystallized TD NiCr," Proceedings of Seven Springs Conference, MCIC-72-10 (Sept. 1972) Chapter X.

62. C.H. Smith and N.J. Grant: "An Alternative Approach to Processing Dispersion-Stabilized Superalloys," Mat. Sci. and Eng. 89 (1987) p. 129-143.

63. R.K. Hotzler and T.K. Glasgow: "The Influence of γ' on the Recrystallization of an Oxide Dispersion Strengthened Superalloy-MA 6000E," Met. Trans. A 13A (1982) p. 1665-1674.

64. M.M. Baloch and H.K.D.H. Bhadeshia: "Directional Recrystallization in Inconel MA 6000 Nickel Base Oxide Dispersion Strengthened Superalloy," Mat. Sci. and Tech. 6 (1990) p. 1236-1246.

65. P. Shewmon: Diffusion in Solids, 2nd ed., The Minerals, Metals & Materials Society, Warrendale, PA, 1989, p. 224-239.

66. A. Otto and J.B. Vander Sande: "On Microstructures Arising from Solid State Reactions in Temperature Gradients," unpublished manuscript (March 1992).

67. A. Otto: "The Oxidation Formation and Properties of $Yb_nBa_{2n}Cu_{3n+1}O_x$ [n=1,2,∞] Superconducting Oxide - Silver Composites," PhD Thesis, Massachusetts Institute of Technology (Feb. 1991).

68. J. Unnam, C.R. Houska: "Ag-Cu Interdiffusion," J. Appl. Phys. 47 (1976) 10, p. 4336-4342, in Diffusion and Defect Data 14 (1977) p. 4.

69. O.M. Bakunin, V.B. Vykhodets, S.M. Klotsman, A.D. Levin, S.A. Matveev, and K.A. Stepanov: "Diffusion Phenomena in Thin Films of High Temperature Superconductors of the Y-Ba-Cu-O System," Defect and Diffusion Forum 66-69 (1989) p. 1311-1317.

70. I.M. Lifshitz and V.V. Slyozov: "The Kinetics of Precipitation from Supersaturated Solid Solutions," J. Phys. Chem. Solids 19 (1961) p. 35-50.

71. P.W. Voorhees: "The Theory of Ostwald Ripening," J. of Statistical Physics 38 (1985) 1/2, p. 231-252.

72. S.M. Allen: Massachusetts Institute of Technology, private communication, 1993.

73. F.A. Nichols: "On the Spheroidization of Rod-Shaped Particles of Finite Length," J. Mat. Sci. 11 (1976) p. 1077-1082.

74. H.E. Cline: "Shape Instabilities of Eutectic Composites at Elevated Temperatures," Acta Met. 19 (1971) p. 481-490.

75. F. Zhanguo, J.I. Chunlin, and Z. Zhongxian: "Standard Gibbs Free Energy of Formation of Superconducting $YBa_2Cu_3O_x$ and Related Compounds in the Y_2O_3-BaO-CuO System," J. Less Com. Metals 161 (1990) p. 49-59.

76. W. Gao and J.B. Vander Sande: "Increasing the Critical Current Density of BSCCO/Ag Superconducting Microcomposites by Mechanical Deformation," Physica C 181 (1991) p. 105-120.

77. P. Sarkar and P.S. Nicholson: "Magnetically Enhanced Reaction Sintering of Textured $YBa_2Cu_3O_x$," Appl. Phys. Let. 61 (1992) 4, p. 492-494.

78. A. Holloway, R.W. McCallum, and S.R. Arrasmith: "Texture Development Due to Preferential Grain Growth of Ho-Ba-Cu-O in 1.6-T Magnetic Field," J. Mater. Res. 8 (1993) 4, p. 727-733.

79. A. Lusnikov, L.L. Miller, R.W. McCallum, and S. Mitra: "Mechanical and High-Temperature (920 C) Magnetic Field Grain Alignment of Polycrystalline $(Ho,Y)Ba_2Cu_3O_{7-\delta}$," J. Appl. Phys. 65 (1989) 8, p. 3136-3141.

80. M.L. Kaforey and J.B. Vander Sande: unpublished research (1993).

81. A.D. Hilton and R. Frost: "Recent Developments in the Manufacture of Barium Titanate Powders," Key Eng. Materials 66 & 67 (1992) p. 145-184.

82. D. Hennings: "Review of Chemical Preparation routes for Barium Titanate," in Electroceramics, British Ceramic Proceedings 41, Institute of Ceramics, Shelton, U.K. (1988) p. 1-10.

83. P.P. Phule and S.H. Risbud: "Review: Low-temperature Synthesis and Processing of Electronic Materials in the BaO-TiO_2 System," J. Mat. Sci. 25 (1990) p. 1169-1183.

84. I. Guttman, S.S. Wilks, and J.S. Hunter: Introductory Engineering Statistics, 2nd ed., J. Wiley & Sons, Inc., Toronto (1971), p. 69, 93.

Biographical Note

Monica L. Kaforey, born Monica L. Slocum, grew up in Orchard Park, New York (home of the Buffalo Bills) where she attended Orchard Park High School. She did her undergraduate studies at Carnegie-Mellon University in Pittsburgh, Pennsylvania and received a BS in Metallurgical Engineering and Materials Science with University Honors. While at CMU, she participated in a co-op program that enabled her to work five semesters at Carborundum, Co. in Niagara Falls, New York. She began her graduate work at MIT in 1989 and took her general exams in the field of Ceramics. Monica is active in many organizations including AMaSS (Association of Materials Student Societies), MRS (Materials Research Society), ACerS (American Ceramic Society), and Girl Scouts.